ABSTRACT

Miocene Paleoenvironments and Paleosol pH Proxies

William E. Lukens, Ph.D.

Mentor: Steven G. Driese, Ph.D.

Paleoenvironmental analysis is an interdisciplinary endeavor that draws on sedimentology, stratigraphy, geochemistry, and geostatistics. This dissertation includes two paleoenvironmental case studies and the development of a new suite of proxies for soil pH. The first case study was performed at Coffee Ranch, the site of a late Miocene (6.6 Ma) bonebed in the Texas Panhandle. Using sedimentology, stratigraphy, and paleopedology, the depositional environments at Coffee Ranch were reconstructed as a fluvial system with seasonally-variable discharge, alluvial paleosols with seasonal water deficit, and intermittent eolian deposits. Climate state was constrained using a combination of paleosol morphological properties, micromorphological associations, pedotransfer functions for climate variables, and elemental mass-balance trends, all of which were consistent with a mean annual precipitation (MAP) nearly double modern values and a much warmer and less seasonally variable mean annual temperature (MAT) than modern conditions. An early Miocene (ca. 17.5 Ma) fossil site located at Ngira, western Kenya, was also analyzed using fluvial geomorphologic and paleopedologic techniques. The Ngira fossil locality preserves a large number of vertebrate fossils, but

has a conspicuous lack of primate remains, unlike nearby contemporaneous fossil sites that contain some of the world's best preserved early Miocene fossil apes. Using pedotransfer functions for climate variables, as well as elemental mass-balance and paleosol morphological indices, the site was reconstructed as having a strongly seasonal, dry subhumid climate. Stable carbon isotopes from pedogenic carbonates are consistent with a surprisingly large amount of C_4 biomass, which was used in conjunction with the presence of microcharcoal grains and rodent community paleoecology to interpret an open-canopy habitat for the site. Finally, a soil database was analyzed, with the goal of producing predictive models for soil pH using elemental oxides as input variables. It was found that large-scale vegetation and climate patterns correlate with soil pH; however, elemental ratios traditionally used to predict MAP and MAT were shown to more closely predict pH than climate. Three new pH pedotransfer functions were applied on succession of middle and late Triassic paleosols from western Pangea, and the results indicate that a paleosols became progressively more alkaline as the megamonsoon climate system gradually diminished.

Miocene Paleoenvironments and Paleosol pH Proxies

by

William Ellis Lukens, B.S., M.S.

A Dissertation

Approved by the Department of Geosciences

_____

Stacy C. Atchley, Ph.D., Chairperson

Submitted to the Graduate Faculty of
Baylor University in Partial Fulfillment of the
Requirements for the Degree
of

Doctor of Philosophy

Approved by the Dissertation Committee

_____

Steven G. Driese, Ph.D., Chairperson

_____

Lee C. Nordt, Ph.D.

_____

Daniel J. Peppe, Ph.D.

_____

Stephen I. Dworkin, Ph.D.

_____

Joseph D. White, Ph.D.

Accepted by the Graduate School

December 2017

_____

J. Larry Lyon, Ph.D., Dean

Page bearing signatures is kept on file in the Graduate School.

TABLE OF CONTENTS

LIST OF FIGURES

LIST OF TABLES

ACKNOWLEDGMENTS

The work reported herein was performed alongside a number of superb scientists, whose enthusiasm and criticism were consistent and meaningful. I am grateful to the following people who have blurred the lines of mentor, colleague, and friend: Gary Stinchcomb, David Fox, Logan Wiest, John Kingston, Dan Peppe, Jack Tubbs, Tom Lehmann, and Jay Pulliam.

Drs. Lee Nordt and Steve Driese have provided me the means to pursue my research assistantship activities with great freedom and curiosity. I am thankful for the guidance and constructive criticism offered by my dissertation committee throughout all stages of my tenure at Baylor. The Faculty of the Geosciences Department have been welcoming and outgoing in their support of my work, and I appreciate the countless conversations and brainstorming sessions we have shared. Special thanks are owed to Paulette Penney, Janelle Atchley, and Jamie Ruth for keeping me in line and on time.

My graduate student compatriots have made our time at Baylor truly rewarding and have provided an intellectually and socially stimulating environment. Our collaborations have made us all better scientists and better people.

Finally, my family and friends have offered me unending support throughout this journey. Most of all, my wife—S. Star George—has given me the inspiration that moves me brightly.

CHAPTER ONE

Introduction

This dissertation has three main components, organized as the ensuing three chapters. For each chapter, I collected all previously unpublished field data and samples, performed laboratory and data analyses, generated figures and tables, and wrote the text of the published or submitted manuscripts, unless otherwise noted below or in the chapters.

In Chapter Two, "Sedimentology, Stratigraphy, and Paleoclimate at the Late Miocene Coffee Ranch Fossil Site in the Texas Panhandle," paleomagnetism analyses were performed by M. Loudermilk. Figures and text associated with paleomagnetism methods and results were generated by M. Loudermilk and D. Peppe. S. Driese provided input on project results and edited drafts of the manuscript.

In Chapter Three, "The Early Miocene Critical Zone at Karungu, Western Kenya: An Equatorial, Open Habitat with Few Primate Remains," a large team of researchers and field assistants were involved in the excavation, collection, and identification of vertebrate fossil remains. These individuals are acknowledged at the end of the chatper. T. Lehmann oversaw the field collection and identification of all fossils recovered for the study, as well as the identification of catalogued specimens that were included from the National Museums of Kenya collections. T. Lehmann analyzed paleontological data and co-wrote (with myself) the sections pertaining to paleontological results. D. Peppe wrote portions of the text pertaining to stratigraphic correlations to and the paleoenvironmental

context of deposits on Rusinga Island. D. Fox contributed meaningful discussion on the interpretation of stable isotope results, and provided substantial edits of the text. S. Driese provided editorial comments and assisted in the interpretation of micromorphological features. K. McKnulty provided input on the history of East African hominoid fossils and the context of other fossil sites from the early Miocene.

For Chapter Four, “Reconstructing pH of Paleosols Using Geochemical Proxies,” L. Nordt, S. Driese, and G. Stinchcomb aided in the design of the study and the overall focus of the manuscript. B. Barnard performed cross-validation of regression models, and J. Tubbs provided input on all statistical methods and results.

CHAPTER TWO

Sedimentology, Stratigraphy, and Paleoclimate at the Late Miocene Coffee Ranch Fossil Site in the Texas Panhandle

This chapter published as: Lukens, W.E., Driese, S.G., Peppe, D.J., and Loudermilk, M., *in press*, Sedimentology, stratigraphy, and paleoclimate at the late Miocene Coffee Ranch fossil site in the Texas Panhandle, *Palaeogeography, Palaeoclimatology, Palaeoecology*.

Abstract

The late Miocene Coffee Ranch fossil assemblage contains some of the earliest evidence of C_4 herbivory in North America. However, little is known regarding the environmental setting associated with the fauna, and a general lack of detailed paleoclimate data exists for the late Miocene from the North American continental interior. In this study, the sedimentary environments, stratigraphy, geochronology, and paleoclimate are interpreted for a series of outcrops of the late Miocene Ogallala Formation in the Texas Panhandle that includes the Coffee Ranch locality. Updated magnetostratigraphy coupled with previously published geochronology indicates that all exposed strata were deposited over a ~277 kyr interval within chron C3An.2n from ~6.42-6.70 Ma. Depositional environments include fluvial channels, floodplain ponds, floodplain paleosols, eolian paleosols, riverine tufa, and reworked volcanic ash. Trunk and tributary fluvial channels are differentiated using channel dimensions, sedimentary structures, and bounding surface architecture, and indicate seasonally-variable discharge. Paleosols from nine pedofacies are described and preserve a spectrum of weakly developed Entisols and weakly to moderately mature Inceptisols and Vertisols. Constitutive mass-balance calculations reveal that mature paleosols formed along distinct

pedogenic pathways. Calcic Vertisols accumulated pedogenic carbonate and exhibited either net volumetric dilation or collapse as a result of mineral weathering. In contrast, non-calcic Vertisols show patterns of decalcification and variable degrees of volumetric dilation and collapse. The presence of the paleosols described in this study requires paleoprecipitation between of 900-1150 mm/yr—approximately double modern values—and a westward shift of the continental udic-ustic soil moisture boundary by ~400 km during the late Miocene. This finding suggests that climates in the southern midcontinent were not sufficiently arid to select for C_4 photosynthetic pathways over C_3 photosynthesis in the late Miocene.

Introduction

The Neogene Period was a key interval in the geologic history of the North American midcontinent, marking the last phase of C_3-dominated biomes preceding the emergence of the Great Plains C_4 grassland (Cerling et al., 1993; Retallack, 1997; Cerling et al., 1998; Jacobs et al., 1999; Janis et al., 2002; Fox and Koch, 2003; Sage, 2004; Fox et al., 2012). The C_3-C_4 transition has been rigorously studied, and recent investigations point to local climatic and environmental conditions as potentially important controls on the distribution of C_4 grass on past landscapes (Cotton et al., 2012; Fox et al., 2012; Chen et al., 2015), including minimum growing season temperature and summertime precipitation (Ehleringer et al., 1997; Cotton et al., 2016). The paucity of quantitative terrestrial paleoclimate records for the Miocene of the North American midcontinent currently limits our ability to differentiate the role of climate from other confounding factors (e.g., fire, Keeley and Rundel, 2005) throughout the C_3-C_4 transition during the Neogene.

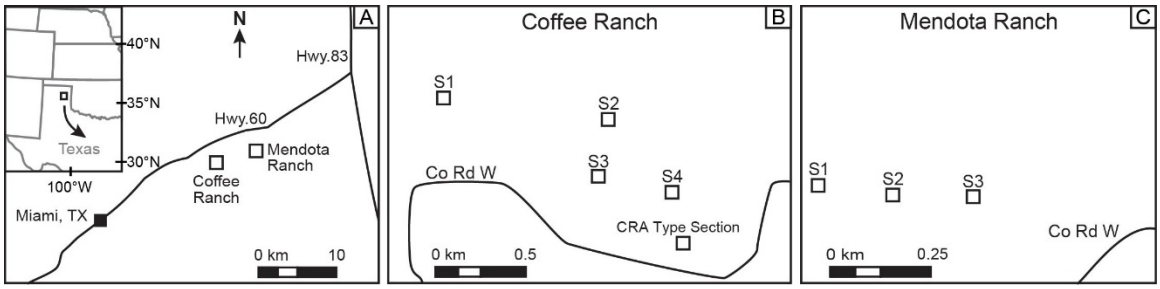

Figure 1.1. Location of Coffee Ranch and Mendota Ranch study sites in the Texas Panhandle.

In this study, we present a sedimentologic, stratigraphic, and geochronologic framework for the Coffee Ranch fossil site (Fig. 1.1), which contains the earliest evidence of C_4 herbivory in the North American geologic record (Wang et al., 1994; Sharp and Cerling, 1998; Passey et al., 2002). Paleosol analysis is used as a tool to reconstruct physical landscape processes, pedochemical weathering pathways, and to estimate mean annual precipitation (MAP) and temperature (MAT) using pedotransfer functions. The results of these analyses provide a baseline assessment of environmental and climatic conditions during this significant time interval in the C_3-C_4 transition.

Paleosols (fossil soils) offer a unique lens into paleoenvironments because they are a commonly-occurring facies element in terrestrial strata and form through the combined action of an array of environmental factors (Jenny, 1994; Kraus, 1999; Retallack, 2001). The factors of pedogenesis were first described in detail by Jenny (1941) in the state-factor model, wherein soils form as a function of climate, organisms/biogenic agents, parent materials, relief/topography, and time of formation. A number of methods now exist for the estimation of paleoclimate based on the elemental composition of paleosol B horizons (Sheldon et al., 2002; Nordt and Driese, 2010b; Stinchcomb et al., 2016) and the oxygen stable isotopic composition of pedogenic carbonates (Nordt et al., 2003; Dworkin et al., 2005). Whereas standing vegetation was

previously studied in detail at Coffee Ranch (Fox and Koch, 2004), we utilize clastic sedimentology, whole-soil geochemistry, oxygen isotopes of carbonates, and comparisons to modern analogue soils to infer climatic conditions, parent material types, geomorphic relationships, and durations of soil formation. By coupling analyses of sedimentary facies and paleopedology, we reconstruct paleoclimate state and landscape-scale physical and geochemical processes operating in the late Miocene in the southern midcontinent.

Geologic Setting

Neogene strata of the Texas Panhandle are underlain by shallow marine Permian strata and overlain locally by Quaternary deposits (Gustavson, 1986; Gustavson and Winkler, 1988). In the area described in this study, the base of the Ogallala Formation is covered and the Quaternary Black Water Draw Formation is preserved as sod tables that onlap outcrops. After deposition of the Ogallala Formation, erosion and sediment bypass in the Canadian River Valley prevented significant burial of late Miocene sediments in the Texas Panhandle (Gustavson, 1986, 1996). Thus, the maximum burial depth of Ogallala Formation strata around Coffee Ranch is likely to be only on the order of tens of meters.

Although nearly a century of predominantly paleontological research has been carried out at Coffee Ranch (e.g., Matthew and Stirton, 1930; Reed and Longnecker, 1932; Webb, 1965; Dalquest, 1969; Dalquest, 1983), the stratigraphy and sedimentology of the Ogallala Formation in the area have yet to be described in detail. Age control at Coffee Ranch is given by the Coffee Ranch ash (CRA), which has yielded fission track (FT) ages of 4.9 ± 0.3 Ma (glass) to 6.8 ± 0.2 Ma (zircon) (Izett, 1975; Naeser et al.,

1980). Boellstorff (1976) also performed FT on CRA glass and reported a date of 5.5 ± 0.4 Ma. Passey et al. (2002) correlated the CRA to the 6.62 Ma Blacktail Creek Ash of the Heiss volcanic field in southern Idaho (Morgan and McIntosh, 2005; Morgan et al., 1999) by comparing the geochemistry of CRA glass shards to a database of volcanic ashes of the western United States (Perkins et al., 1995, 1998). Both the Blacktail Creek Ash and the CRA were deposited within a chron of normal polarity (Lindsay et al., 1975; Pierce and Morgan, 1992), now accepted to be chron C3An.2n (Passey et al., 2002), which occurred from 6.436-6.733 Ma (Ogg, 2012). We follow Passey et al. (2002) and use the date of 6.62 Ma for the CRA. Lindsay et al. (1975) identified a reversal roughly 15 m below the CRA bonebed; however, outcrop exposure no longer extends to that depth at Coffee Ranch, likely as a result of recent slumping of Quaternary sediments.

Previous Paleontologic and Paleoenvironmental Interpretations

The Coffee Ranch fossil locality preserves a diverse assemblage of late Miocene vertebrates that serve as the Hemphillian North American Land Mammal Age (NALMA) type fauna and the Late Hemphillian chronofauna (Wood et al., 1941; Dalquest and Patrick, 1989; Schultz, 1990; Tedford et al., 2004). The fossil assemblage is entirely associated with the CRA type locality stratigraphic section (Fig. 1.2). Most of the vertebrate remains have been recovered from the greenish sand and sandy clay that lies directly below the base of the ash deposit, though a small number of isolated elements have been found in the ash itself (Shultz, 1990). In addition, Dalquest (1983) recovered a limited microfauna by screenwashing the bentonite at the base of the ash.

Figure 1.2. Stratigraphic sections for Coffee Ranch (CR) and Mendota Ranch (MR). See Table 1.1 and Section 3.1 in the text for lithofacies descriptions. Pedofacies descriptions can be found in Section 3.2 in the text and Figs. A2-3. Roman numerals correspond to pedofacies numbers. Massive sandstones colored as dark grey are interpreted to be eolian in origin, and those colored as light blue have redoximorphic Fe features.

Based on the occurrence of alternating green and red bioturbated sandy clay beds with rare lines of carbonate gravel, Dalquest (1969) interpreted the sedimentary environment to be a shallow ephemeral lake, likely similar to the ephemeral playas common on the modern Great Plains (Gustavson et al., 1995; Gurdak and Roe, 2009). The presence of scavenging traces on bones and evidence of trampling of skeletal elements suggests that some of the fauna were subaerially exposed before they were buried in the playa (Dalquest, 1969). In all, over a thousand specimens have been recovered from the clayey sand below the CRA, with remains preserved as both articulated individuals and disarticulated concentrations of bone from a variety of taxa (Dalquest, 1983). These findings are consistent with an attritional accumulation subjected to variable degrees of post-depositional reworking.

A taxonomic list for the Coffee Ranch fauna was first summarized by Dalquest (1969) and updated by Shultz (1990). The fauna includes a large number of mammals, including rodents, carnivores, artiodactyls, perissodactyls, mustelids, sloths, proboscideans, lagomorphs, bats, and Eulipotyphlans (shews and moles). Less abundant taxa include amphibians, fish, birds, and reptiles, which are represented by snakes, crocodilians, tortoises, and aquatic turtles.

Previous paleoenvironmental interpretations of the late Miocene at Coffee Ranch have been made using a variety of archives and proxies, each offering insight into specific components of climate and vegetation. Equids from the Coffee Ranch assemblage contain the earliest definitive evidence in North America of C_4 grass consumption, based on stable isotopic analyses of their tooth enamel (Wang et al., 1994; Sharp and Cerling, 1998; Passey et al., 2002). Using proportions of hypsodonty from the

Coffee Ranch ungulate assemblage, Fraser and Theodor (2013) reconstructed the ecosystem as a bushland with a MAP of 992 mm/y. Further, the decrease in browsers in the Coffee Ranch fauna relative to assemblages of Clarendonian age in the southern midcontinent suggests that a long-term drying trend occurred from the middle to late Miocene (Shultz, 1990). Pedogenic calcium carbonate isotopic values ($\delta^{13}C_{cc}$) from Coffee Ranch suggest an evenly-mixed and dispersed understory of ≤ 25 % C_4 biomass (Fox and Koch, 2003, 2004). Taken together, these studies show that the abundant and diverse fauna preserved at Coffee Ranch is a well-sampled assemblage of the local area, and the local environment had much less C_4 biomass and a larger amount of woody (C_3) vegetation than modern conditions in the southern High Plains.

Methods

Field Methods

The stratigraphy of the Ogallala Formation was documented at Coffee Ranch, including the fossil locality and any accessible outcrops nearby (Fig. 1.1). The strata were laterally traced to a neighboring property hereafter referred to as Mendota Ranch. In total, nearly 7 km of intermittent outcrop exposure with upwards of 25 m of vertical section were described (Figs. 1.1, 1.2). Correlation between measured sections was accomplished using a hand-level or walking out marker horizons within each locality. The CRA was used as a datum to correlate Coffee and Mendota Ranch outcrops. Lithofacies were assigned using a modification of Gustavson's (1996) description of the Ogallala Formation and standard lithofacies codes (Miall, 1978), in a similar fashion to Joeckel et al. (2014). Paleosols were described with respect to horizonation, ped structure, color,

mineralizations, grain size, bounding contacts, root traces, and invertebrate trace fossils (Shoenenberger et al., 2002). Pedofacies were delineated using observed sedimentologic and pedogenic features (*sensu* Bown and Kraus, 1987; Kraus, 1987).

Paleomagnetic block samples were collected from five stratigraphic sections at Coffee and Mendota Ranch outcrops by digging ~0.5 m-deep trenches into fine-grained sedimentary units to remove any weathered material. At each sampling locality, one oriented block sample was collected. A flat face was made using a hand rasp and the strike and dip of that face was measured using a Brunton pocket transit compass. Paleomagnetic sampling was dictated by lithology, and an attempt was made to sample the entire stratigraphic sequence exposed at both sites.

Paleosol Laboratory Methods

Serial samples in paleosol profiles were taken every 10-20 cm. The bulk density of natural aggregates was measured using the paraffin method (Soil Survey Staff, 1996). Powdered samples were analyzed for major and trace elemental composition at ALS Global (alsglobal.com) using a four dissolution and ICP-AES/MS analysis. Aliquots from samples of the uppermost B horizon of four pedofacies were also analyzed using lithium borate fusion/ICP-AES to measure major elements and SiO_2. Thin sections of oriented samples from each horizon were prepared by Spectrum Petrographics (petrography.com) and characterized using methods from Bullock et al. (1985) and Brewer (1964).

Carbonates were analyzed in thin section to differentiate primary micrite from diagenetic sparite and were micro-drilled on paired thin section billets. The resulting powders were analyzed for oxygen isotopic composition at Baylor University using a Thermo-Electron dual-inlet gas-source stable isotope ratio mass spectrometer. The delta

notation is used in reporting stable oxygen isotopic compositions of calcium carbonate ($\delta^{18}O_{cc} = [(R_{sample} / R_{standard}) - 1] \times 1000$), where R is the ratio of heavy to light oxygen ($^{18}O/^{16}O$). All $\delta^{18}O_{cc}$ values are reported relative to the Vienna Pee Dee Belemnite (VPDB) standard with analytical precision of ≤ 0.07 ‰.

Paleomagnetism Analyses

In the laboratory, the oriented block samples were trimmed to ~2 cm^3 using a lapidary saw. The natural remnant magnetization (NRM) for each sample was measured at Baylor University using an automated three-axis DC-SQuID magnetometer housed inside a two-layer magnetostatic shield with background fields typically less than 300 nT. Isothermal magnetic and low-coercivity viscous remnant magnetism were removed using a low alternating field (AF) pre-treatment using a 3-axis automated static alternating field device. Ten to twenty thermal demagnetization steps were then performed from 100 °C to the maximum unblocking temperature, which was typically 400-500 °C, in a controlled nitrogen atmosphere to minimize oxidation reactions. Progressive thermal demagnetization was undertaken until the magnetic intensity of the samples fell below the background noise of the magnetometer, or the measured directions became erratic and unstable.

The characteristic remnant magnetization (ChRM) for each sample was identified via principal component analysis (Kirschvink, 1980). Best-fit lines representing the ChRM direction were defined by three or more consecutive demagnetization intervals trending towards the origin with a maximum angle of deviation (MAD) less than 20° (Fig. A1). If a sample exhibited demagnetization intervals clustered around a solitary point, but did not decay towards the origin, at least four consecutive demagnetization

steps were selected and anchored to the origin to define the ChRM and were accepted if the MAD was less than 20°. Samples with erratic and unstable demagnetization behavior were excluded from analyses. The mean paleomagnetic direction was calculated for each magnetostratigraphic section, for the Coffee Ranch and Mendota Ranch localities, and for all sections using Fisher statistics (Fisher, 1953).

Mass-Balance Geochemistry

Weathering trends in paleosol profiles were studied using constitutive mass-balance functions developed by Brimhall and Dietrich (1987), Chadwick et al. (1990), and Brimhall et al. (1991). Closed-system volumetric changes related to pedogenic processes are calculated as strain (ε), where:

$$\varepsilon_{i,w} = \left(\frac{\rho_p C_{i,p}}{\rho_w C_{i,w}}\right), \quad (1)$$

or the ratio of the products of bulk density (ρ) and immobile index element (i) concentration (C) in the parent material (p) to weathered material (w). Down-profile changes in elemental concentrations were calculated using the open-system transport function (τ), also referred to as translocation, where:

$$\tau_{j,w} = \left(\frac{\rho_w C_{j,w}}{\rho_p C_{j,p}}\right)\left(\varepsilon_{i,w} + 1\right) - 1, \quad (2)$$

using the previously defined terms. Translocations were calculated for each horizon, using average values for multiple samples within horizons. Strain and translocations are presented as percent change.

Paleoclimate Estimations

Paleosol climofunctions were used to predict mean annual precipitation (MAP) and temperature (MAT) (Table 1.1). The chemical index of alteration minus potassium

(CIA-K = 100 x Al_2O_3 / (Al_2O_3 + CaO + Na_2O)), which tracks feldspar hydrolysis and base cation leaching (Sheldon et al., 2002) and CALMAG (100 x Al_2O_3 / (Al_2O_3 + CaO + MgO)), which tracks carbonate precipitation and base cation retention versus leaching in clay-rich Vertisols (Nordt and Driese, 2010b), were used to predict MAP. Mean annual temperature was estimated using a function based on the salinization index (NaK = (Na_2O + K_2O)/ Al_2O_3; Sheldon et al., 2002), which is controlled by the thermodynamic dissolution of feldspars. The CIA-K, CALMAG, and NaK indices each use oxide moles, and where multiple B horizons were present in profiles, samples were averaged before calculation of MAP and MAT.

The paleosol-paleoclimate model ($PPM_{1.0}$, Stinchcomb et al., 2016) was also used to co-predict MAP and MAT. $PPM_{1.0}$ uses eleven elemental oxides (Fe_2O_3, Al_2O_3, SiO_2, TiO_2, ZrO_2, CaO, MgO, K_2O, Na_2O, MnO, and P_2O_5) input as weight percent to estimate MAP and MAT, which are modelled as a joint response using a thin plate spline drawn through the transformed sample scores on axes calculated through a partial least squares regression analysis (Stinchcomb et al., 2016). Only uppermost B horizon samples were input into $PPM_{1.0}$, in accordance with the data used to calibrate the model. The benefits of $PPM_{1.0}$ over other methods include: 1) few *a priori* assumptions are required for paleosol applications due to the diverse training data set used to build $PPM_{1.0}$; 2) the range of MAP and MAT that $PPM_{1.0}$ can predict is more broad than most pedotransfer functions; 3) modelled error for MAT is 3.98 °C, less than other geochemical paleothermometers; and 4) multiple validation steps were taken by Stinchcomb et al. (2016) to model the uncertainty of $PPM_{1.0}$ predictions.

Table 1.1. Paleoclimate Proxies

Index	Index Formula	Model Error[a]	Constraints	Reference
Mean annual precipitation				
CIA-K	14.27x - 37.632	182 mm	Bt, Bw horizons	Sheldon et al. (2002)
CIA-Kv	18.64x - 350.4	146 mm	Vertisols only	Nordt and Driese (2010b)
CALMAG	22.69x - 435.8	180 mm	Vertisols only	Nordt and Driese (2010b)
Mean annual temperature				
NaK	-18.52x + 17.298	4.4°C	Bt, Bw horizons	Sheldon et al. (2002)
$\delta^{18}O_{cc}$[b]	$-0.498T^3 + (x + 152.04)T^2 - 2.78 \times 10^6 = 0$	4.1°C	Primary micrite	Nordt et al. (2003); Dworkin et al. (2005)
$\delta^{18}O_{cc}$[c]	(x + 12.65) / 0.49	4.1°C	Primary micrite	Dworkin et al. (2005), after Cerling and Quade (1993)
Mean annual precipitation and temperature				
PPM	Thin plate spline[d]	512 mm, 3.98°C	Uppermost B horizons; no Gelisols	Stinchcomb et al. (2016)

Note: Formulas for the CIA-K, CALMAG and NaK indices are included in the text.
[a]Values used are standard errors from regression analysis, except for the following: 1) $\delta^{18}O_{cc}$ errors are based on estimates by Hyland and Sheldon (2013) of the theoretical function; we use the error value as an estimate for both isotope paleothermometer functions. 2) PPM errors are root mean square prediction error based on validation modelling.
[b]Referred to as the theoretical function elsewhere in the text.
[c]Referred to as the empirical function elsewhere in the text.
[d]Modelled in SAS statistical software; see Stinchcomb et al. (2016) for code and methods

Paleotemperature was estimated independently using the $\delta^{18}O_{cc}$ of pedogenic calcium carbonate nodules and rhizoliths. Two equations were used that relate $\delta^{18}O_{cc}$ to MAT: 1) a theoretical function resulting from simultaneous solution of the equations that describe the fractionation of oxygen from meteoric water into pedogenic carbonate and the spatial relationship between MAT and $\delta^{18}O$ of meteoric water ($\delta^{18}O_{mw}$) (Nordt et al., 2003; Dworkin et al., 2005), and 2) an empirical function based on the relationship

between $\delta^{18}O_{cc}$ and MAT using data compiled by Cerling and Quade (1993) and reformatted by Dworkin et al. (2005).

The theoretical function uses a laboratory-calibrated equation that relates the temperature-dependent fractionation of oxygen from meteoric water into pedogenic carbonate (Friedman and O'Neil, 1977) and the distribution of meteoric water $\delta^{18}O$ values as they relate to MAT (Fricke and O'Neil, 1999). By simultaneously solving both functions for temperature, a third-order polynomial is generated that uses $\delta^{18}O_{cc}$ as the only input value (Dworkin et al., 2005). Modern, independent data scatter about the theoretical function, suggesting that it is a valid approach to predicting MAT (Dworkin et al., 2005). The empirical function uses observations of modern $\delta^{18}O_{cc}$ and MAT that were not included in the data sets of Dworkin et al. (2005), and therefore have their own distribution and independent regression function. Dworkin et al. (2005) showed that the data of Cerling and Quade (1993) scatter about the theoretical function, which suggests that results of both functions should be similar when applied to independent data.

For these functions to be applicable in deep time, both the spatial distribution of $\delta^{18}O$ compositions of precipitation and regional variations in MAT would have to be similar to modern conditions, or spatial distributions both $\delta^{18}O$ of precipitation and MAT would have to change in concert. We vet the results of the transfer functions that relate $\delta^{18}O_{cc}$ to MAT by comparing independent MAT estimates from paleosol elemental proxies and previously published fossil tooth enamel $\delta^{18}O$ from Coffee Ranch equids (Sharp and Cerling, 1998), which allows for estimation of paleo-meteoric water composition.

Results

Lithofacies Associations

Lithofacies designations, criteria for recognition and environmental interpretations are shown in Table 1.2, and the stratigraphic occurrence of each lithofacies is shown in Figure 1.2.

Channel Sandstones. Fluvial channels occur as tabular (St) and lenticular sandstones (Sl1, Sl2). Individual St channels are >250 m wide by 2-6 m thick (Fig. 1.3A-B; Fig. 1.4) and traceable for kilometers when occurring as caprocks. External bounding surfaces are abrupt and horizontal with smooth lower contacts (Fig. 1.3C). Low-flow conditions are preserved as mud drapes, bioturbation of sedimentary fabrics, and vertebrate trackways (Fig. 1.4A-C). This channel form is interpreted to be a perennial trunk channel with episodically-variable discharge (Bridge, 2003).

Individual lenticular channels are smaller in size than St channels (Fig. 1.4), typically < 2 m thick by 15-20 m wide and only visible in outcrop cross section. Type 1 lenticular sandstone (Sl1) channels have planar to wavy external bounding surfaces. Reworked pedogenic carbonate nodules form lenses of gravel lag between structureless sand (Fig. 1.4D-E) and broken vertebrate fossils. Type II lenticular sandstones (Sl2) have planar upper contacts that interfinger with overlying deposits. Lower external bounding surfaces are wavy and scour into underlying units. Internal surfaces are planar to inclined and bound 10-30 cm thick couplets of sand fining upward to silt (Fig. 1.3C). Channel fill sands contain lateral accretion sets, planar and trough cross- stratification, cobble-sized

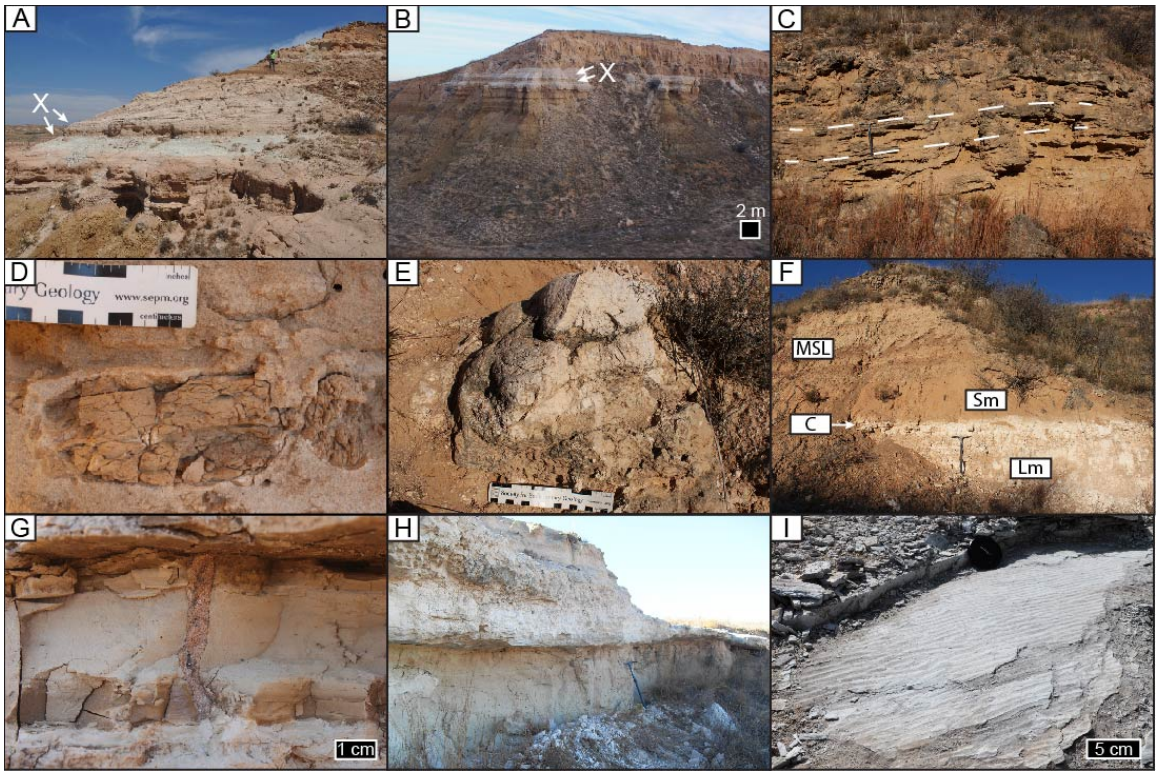

Figure 1.3. Outcrop photographs from Coffee and Mendota Ranch. A) Tabular trunk channel (St) facies overlying Mm facies at MR section 1. X denotes volcanic ash. Geologist in background is 1.82 m tall. B) St facies with volcanic ash (X) overlying stacked floodplain deposits at MR S3. C) Sl2 facies with lateral accretion sets (dashed lines) and wavy internal bounding surfaces at CR section 1. Pick axe between dashed lines is 62.5 cm. D) Reworked bedded sandstone clasts armored with carbonate in a Sl2 channel. E) Stromatolite occurring on an internal bounding surface in a Sl2 channel. F) Massive limestone (Lm), chert (C), unconsolidated massive eolian sand (Sm) and mudstone-sandstone-limestone (MSL) floodplain facies in CR section 1. Note pick axe (62.5 cm) for scale in foreground. G) Root trace filled with red eolian sand in MSL facies. H) Coffee Ranch bonebed site with massive volcanic ash (X) overlying massive, bioturbated fluvial channel sand (Sm). Note pick axe (62.5 cm) for scale. I) Symmetric ripples on a bedding plane at the top of the outcrop pictured in H.

rip-up clasts, brecciated bank collapse blocks, and stromatolites (Fig. 1.3D-E, Fig. 1.4). Vertebrate trackways are visible on bedding planes (Fig. 1.4). Lenticular channel facies are interpreted to be tributaries of tabular sandstone facies based on the smaller cross-sectional area and width-to-depth ratio (Fig. 1.4).

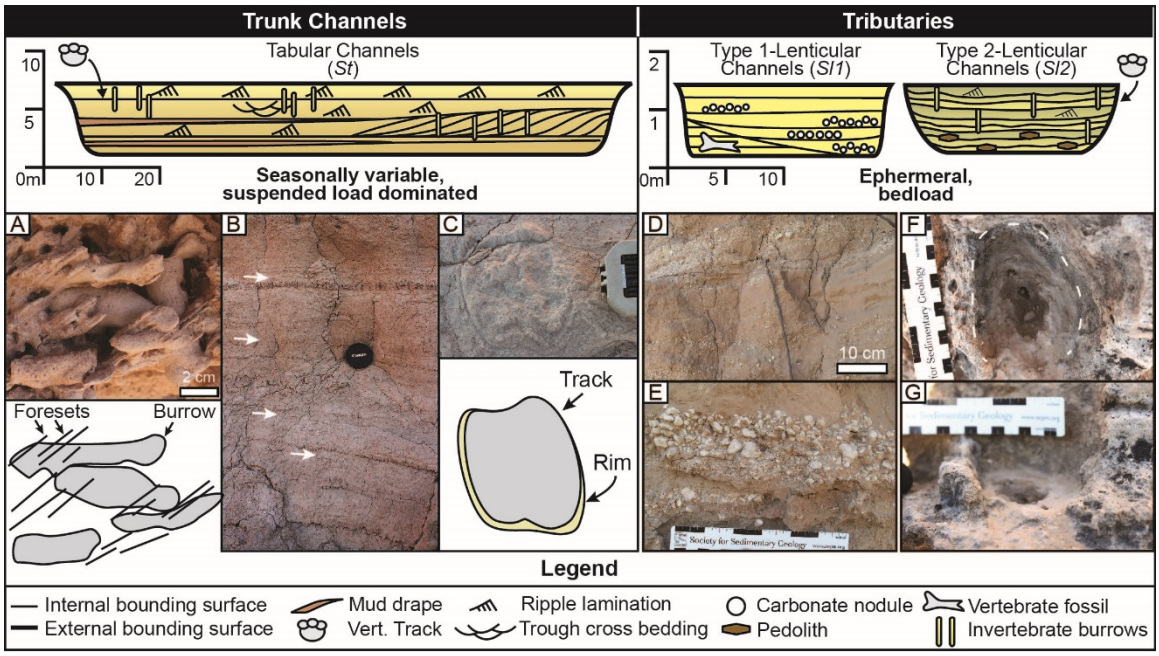

Figure 1.4. Fluvial channel facies and flow-indicating structures. Note change in channel dimension scale bars between channel types. A) Invertebrate burrows disrupting primary 2D dune bedding. B) Mud drapes between planar beds. Lens cap is 5.2 cm wide. C) Vertebrate track of a camel. Brunton compass is 7 cm wide. D-E) Lenses of reworked carbonate nodules occurring as a lag. F-G) Possible track on bedding plane in Sl2 channel, with plan view (F) and cross-section (G).

Thin Sandstones. Two varieties of thin sandstone deposits were observed and are independent of channel bodies. Rippled sandstones (Sr) are < 1 m thick with occasional rip-up clasts, root traces and ripple lamination. This facies is interpreted as a crevasse splay. The second sandstone facies includes redoximorphic sandstones (Sx) that range in thickness from 10-100+ cm. Lower contacts tend to be abrupt and smooth or wavy with ripple lamination or horizontal bedding present near the base of some deposits. Redoximorphic Fe mottles, drab halo root traces, and weak soil structure are present in some units, indicative of subaerial exposure and pedogenic modification. This facies is interpreted to represent proximal floodplain deposits and fluvial levees.

Mud-Sand-Limestones. Successions of interbedded mudstone, siltstone to very fine sandstone, and limestone occur in packages ranging from 10-250 cm thick and are grouped as one facies (MSL). Mudstones are laminated to massive, commonly packed with fecal pellets, and typically contain mudcracks and tubular invertebrate burrows (*Skolithos* isp.) filled with orange fine sand penetrating downward from the upper contact (Fig. 1.3G). Stromatolites and adhesive meniscate burrows (*Naktodemasis* isp.) are also present in mudstones (Fig. 1.5 A-C), representing contrasting intervals of standing water and subaerial exposure (Counts and Hasiotis, 2009), respectively. Siltstones, sandstones, and limestones tend to be ripple-laminated, 1-10 cm thick beds, and are interbedded with mudstones. The MSL lithofacies is interpreted to be small floodplain ponds based on the lack of pedogenic alteration and common stratigraphic juxtaposition with sandy alluvial paleosols, crevasse splays and channel bodies.

Massive Mudstone. Massive mudstone (Mm*)* units of variable thickness (10-200+ cm) occur in nearly all stratigraphic sections. Lower contacts are either eroded into MSL facies, disrupted through bioturbation, or covered. Upper contacts are typically truncated by overlying deposits. Bedding is absent and the presence of root traces, soil structure, slickensides, carbonate nodules, and cryptic invertebrate trace fossils are indicative of pedogenic alteration. This facies is interpreted to represent medial to distal fine-grained flood deposits and floodplain paleosols (see below).

Volcanic Ash. The Coffee Ranch Ash (CRA) is a vitric tuff (facies X) that occurs as white to pink, laminated very fine sand- to silt-sized ash and as white, trough cross-stratified to horizontally bedded sandstone channel fill (Fig. 1.3H). The base of the CRA

Table 1.2. Lithofacies descriptions and characteristics.

Code	Lithofacies	Sedimentary Structures	Interpretation
St	Medium to vc sand, gravel at base	Large-scale inclined tabular and horizontal bedding, 3D dunes, parting lineations, mud drapes, ripple lamination	High-energy seasonal stream
Sl1	Type-1 lenticular sandstone	Reworked carbonate nodule lag, mud drapes, trough cross bedding, vertebrate trackways, broken vertebrate fossils, 3D dunes	Mixed-energy tributary
Sl2	Type-2 lenticular sandstone	Thin, interbedded fining upward vc to f sandstone, bank collapse breccia, vertebrate trackways, inclined tabular cross bedding, trough cross bedding, rare stromatolites	Mixed-energy tributary
Sr	Fine to medium sand	Ripple lamination, few rip up clasts, no roots or ped structure	Crevasse splay/proximal floodplain deposit
Sx	Fine to medium sand	Ripple lamination or horizontal bedding at base of unit, redoximorphic Fe mottles, root traces, weak soil structure	Fluvial levee or proximal flood deposit/redoximorphic paleosol
MSL	Mud-Sand-Limestone	Interbedded mudstone, siltstone to vf sandstone and limestone; very thin bedding; laminated to massive mudstone, ripple laminated sandstones and limestones; mudcracks, tubular burrows/root traces infilled with orange f sand	Floodplain pond
Mm	Massive mudstone	Variable thickness; Bedding absent; soil structure, slickensides, root traces, carboante nodules, occasional tubular burrows and fractures infilled with orange f sand	Medial to distal floodplain paleosol
Sm	Massive sandstone	Massive, semi- to unconsolidated sands; no vertical grain size change; root traces, carbonate nodules, prismatic ped structure, rubified horizons and invertebrate burrows present in some units	Eolian sheet sand/eolian paleosol
Lm	Massive limestone	Up to 2m thick mound with sloped, tapering sides that interbed with fine sand; massive to vertically fractured structure; rare zones of concentric lamination (stromatolites)	Riverine tufa
C	Chert	Massive, conchoidally-fracturing grey-white chert; microcrystalline appearance; siliceous cementation of limestone	Devitrified and recrystallized volcanic ash
X	Vitric Tuff	White to pink vitric tuff with clay to vf sand grain size; occurs as trough cross-stratified to horizontally bedded channel fill, massive, burrowed sand, symmetric ripple laminated vf sand, laminated silt and laminated betonitic clay	Distal volcanic ash reworked into *St* channel; ephemeral playa lake

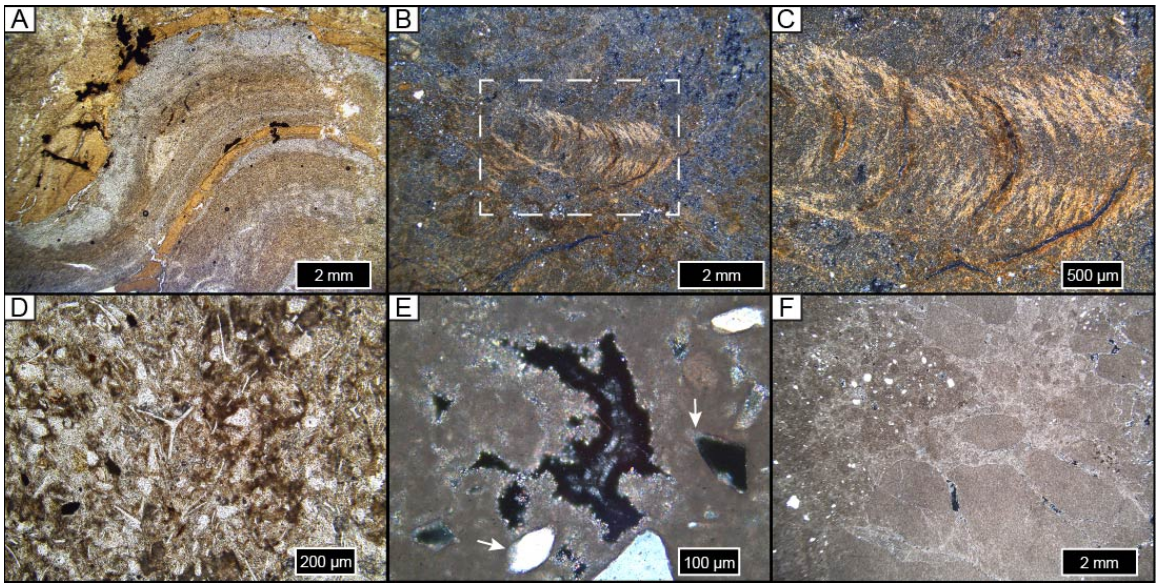

Figure 1.5. Photomicrographs of selected lithofacies features. All photographs are oriented vertically and imaged in cross-polarized light unless otherwise noted. A) Stromatolite in MSL facies, preserved as alternating layers of clay films and carbonate. B-C) Adhesive meniscate burrow (*Naktodemasis* isp.) in MSL facies. D) Pink volcanic ash from the Coffee Ranch Ash Type Section. Note bubble-wall and acicular ash shards as well as black and clear detrital silicate grains; plane-polarized light. E) Chert with recrystallized opaline overgrowths in voids and on grains (white arrows). F) Massive limestone tufa from CR section 1. Note reworked carbonate clasts and detrital quartz grains.

is composed of massive, bioturbated sandy tuff transitioning upward to laminated silty tuff capped by symmetric ripples (Fig. 1.3I) and vertebrate trackways (Lucas and Schultz, 2007). The massive ash interval is a maximum of ~2 m thick and tapers upward to the sides, suggesting that it infilled a low point on the paleolandscape (Dalquest, 1969). Alternating pink and white zones are present in the massive interval and are bounded by irregular contacts blurred by bioturbation. The white and pink deposits at the Coffee Ranch bone bed both contain a mixture of unaltered ash and detrital quartz, with the pink intervals containing common Fe oxides (Fig. 1.5D). A laminated bentonite is present below the massive pink and white ash and contains a finer matrix and relatively fewer ash shards.

The CRA type section laterally grades into the Sl1 channel facies to the northwest. This channel was traced to CR section 2, where the CRA is interbedded between tabular cross strata. The CRA also appears in MR section 1, where the CRA is cross-bedded in the St channel facies.

Chert. A chert bed directly overlies the tufa in CR section 1 (Fig. 1.3F). Bounding surfaces are abrupt and wavy, displacing juxtaposed stratigraphic units. Microcrystalline overgrowths are present in thin section, occurring as void fills and grain overgrowths in a calcareous matrix (Fig. 1.5E). We infer the source of the silica to be diagenetically altered volcanic ash, as no other observed sources of dissolved silica are present in the stratigraphy. Further, the chert occurs stratigraphically within 1 m of reworked volcanic ash in fluvial channels (Fig. 1.2: CR S2, MR S1).

Massive Limestone. Massive limestone (Lm) units are present at both Coffee and Mendota Ranch. Each deposit is roughly 2 m thick and contains pockets of uncemented sedimentary matrix (Fig. 1.3F). Thin, indurated beds of white carbonate extend laterally from a central core and are interbedded with fine sand. Filaments of carbonate are present in the sandstones above and below the limestone at both localities. In CR section 2, stromatolites occur where a Sl2 channel interfinges with massive limestone (Fig. 1.3E). Macroscopically-massive limestones contain reworked micritic grains and detrital quartz grains (Fig. 1.5F). We interpret the massive limestones to be riverine tufas, formed as a result of alkaline groundwater discharge into fluvial channels (e.g., Beverly et al., 2015).

Massive Sand. Massive, semi- to unconsolidated sand (Sm) occurs in two settings. Orange sands are sparse and occur between laminated and pedogenically

modified floodplain mudstones. Lower contacts are either abrupt smooth or bioturbated. Grain size does not change vertically and pedogenic modification is evidenced by root traces, occasional prismatic ped structure, rubified horizons, carbonate nodules and tubular invertebrate burrows (*Skolithos* isp). This facies in interpreted to represent eolian sand sheet deposits.

Drab green to red sands are present directly below the CRA type section and contain weak bedding (Fig. 1.3H). The majority of vertebrate fossils associated with the Coffee Ranch fauna have been recovered from either clusters of interlocking bones at the base of the unit, or as articulated to disarticulated individuals throughout the unit (Dalquest, 1969; Shultz, 1990). This facies is interpreted to be a bioturbated playa lake-bottom.

Pedofacies

A total of 22 paleosols were described in the field and distilled into 9 pedofacies (Figs. A2-3). Paleosol profiles and descriptions are modified from standard NRCS soil descriptions (Schoeneberger, 2002) and presented with supporting micromorphological observations. Pedofacies were delineated through a combination of lithofacies association and observed pedogenic features. The stratigraphic occurrence of each pedofacies is shown in Figure 1.2.

Alluvial Paleosols. Alluvial paleosols (Pedofacies I-VI) range from sandy to clayey textures and exhibit features consistent with weak to moderate pedogenic maturity.

Vertisols were identified by the presence of wedge peds and slickensides (Fig. 1.6). A range of Vertisols are associated with the massive mudstone (Mm) lithofacies.

Incipient Vertisols (Pedofacies I) lack master slickensides but contain common pressure faces and wedge peds. Non-Calcic Thick Vertisols (Pedofacies II) exhibit complex slickenside development and well-formed ped structure. Clay linings were observed on slickensides and root voids (Fig. 1.6C) and carbonates were absent. Calcareous Vertisols range from stage I to stage II carbonate accumulation (Pedofacies III and IV, resp.) (Fig. 1.6E-H). Pedogenic carbonates almost exclusively occur along vertical root features, which range from hairline carbonate filaments (Stage I Calcic Vertisols) to rhizoliths up to 2-7 cm wide and ~2 m long (Stage II Calcic Vertisols). Rare millimeter-scale nodules are present in the matrix of most calcic paleosols.

Two paleosol types are associated with the Sr lithofacies. Mottled Vertisols (Pedofacies V) are weakly developed, evidenced by weak pedality and a lack of clay translocation and carbonate precipitation. Zones of Fe concentration and depletion are rare to common throughout the B and C horizon matrices. Weakly developed, sandy alluvial paleosols (Fluvial Inceptisols, Pedofacies VII) are rare and consist of mottled Bw horizons overlying C horizons with ripple lamination and rip-up clasts.

The Sandy Calcic Vertisol pedofacies (VI) is anomalous, occurring on sandy clay sediment (Sm lithofacies) but containing abundant master slickensides. Large calcareous rhizoliths are off-set along master slickensides (Fig. 1.6G-H) and multigenerational soft and hard carbonate masses are present in all horizons, consistent with stage II carbonate accumulation (Gile et al., 1966). Translocated clay coats ped surfaces and root tubules in the Btkss horizon. The two lowermost horizons (Bk1 and Bk2) lack vertic features and translocated clay.

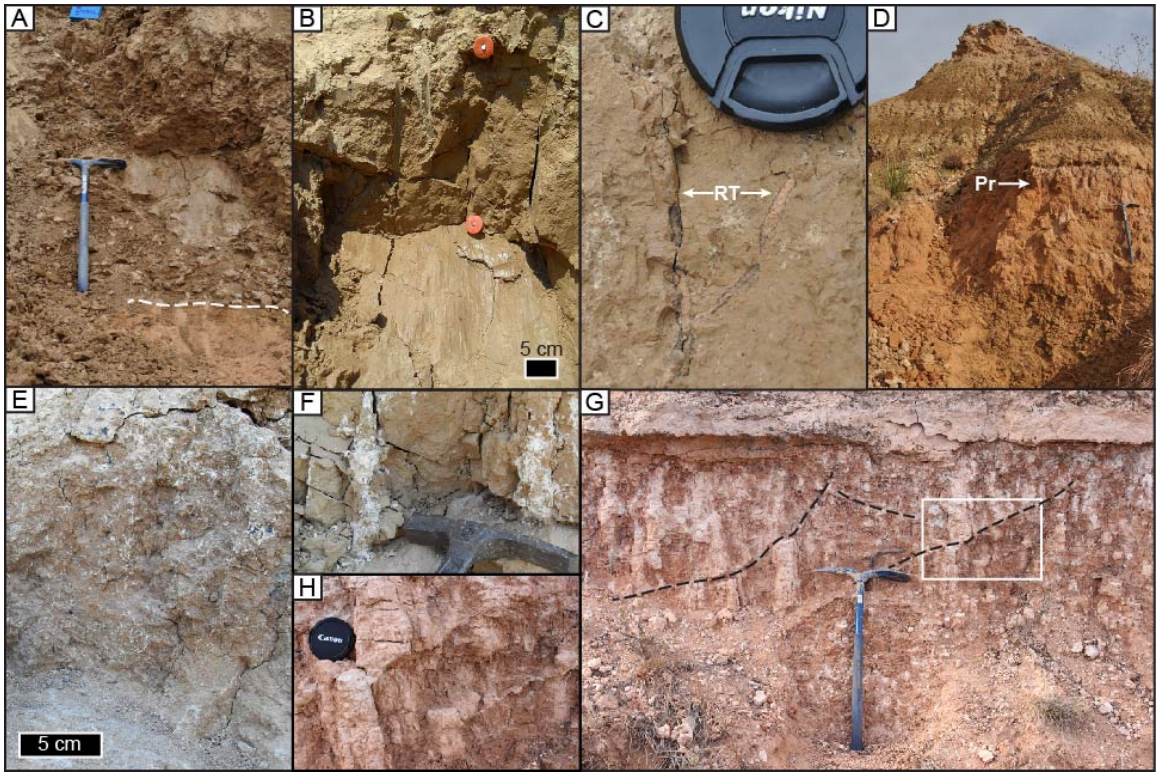

Figure 1.6. Field photographs of paleosol features. A) Brown Non-Calcic Thick Vertisol overlying an orange-tan Eolian Entisol (MR section 3). Note the prominent master slickenside next to the 62.5-cm long paleo-pick. B) Wedge peds (W) with boundaries delineated by dashed lines; close-up of a slickenside of a Non-Calcic Thick Vertisol. C) Root trace (RT) with clay and MnO_2 linings and orange sand infill in a Non-Calcic Thick Vertisol. Lens cap = 5.2 cm. D) Clay-rich, brown alluvial Vertisols interbedded with an orange Eolian Inceptisol exhibiting prismatic peds (Pr); boundaries of some prismatic peds are outlined (MR S2). Paleo-pick for scale. E) Filamentous calcareous rhizoliths in a Stage I Calcic Vertisol with subangular blocky peds (MR S2). F) Stage II Calcic Vertisol with calcareous rhizoliths (CR section 2). Note wedge peds. G) Sandy Calcic Vertisol capped by a fluvial channel (CR section 1). Dashed lines highlight master slickensides, which offset large calcareous rhizoliths. H) Close-up photo of white box in G. Note offset of root trace from pedoturbation.

Eolian Paleosols. Eolian paleosols formed on uniform fine sand (Sm lithofacies) and are identified by the presence of root traces, carbonate nodules and/or color change from parent material. The Eolian Inceptisols pedofacies (VIII) contains a rubified Bw horizon overlain by a thin A horizon that contains fine sediment-filled root traces, likely associated with shallow rooted herbaceous species. The Eolian Entisols pedofacies (IX)

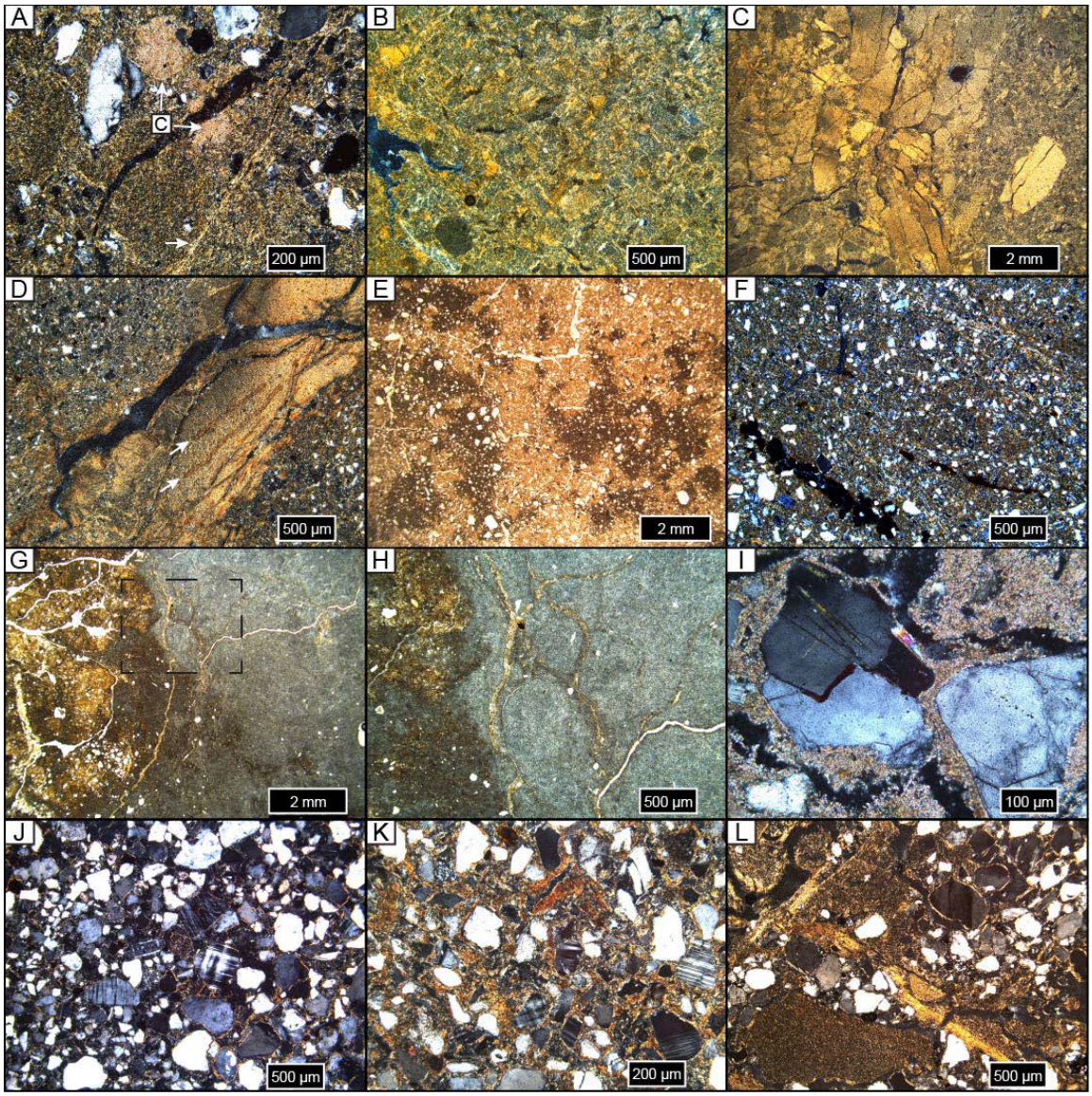

Figure 1.7. Photomicrographs of selected pedogenic features. All images are vertically oriented and in cross-polarized light unless noted. A) Weakly developed cross-striated clay fabric and pedogenic carbonate impregnation (c) in a Thin Vertisol Bss horizon. B) Well-developed cross-striated fabric in the Bss horizon of a Non-Calcic Thick Vertisol. C) Pedogenic breccia resulting from pedoturbation in the Bss horizon of a Non-Calcic Thick Vertisol. D) Multigenerational slickenside with Fe coatings in Stage II Calcic Vertisol Bkss1 horizon. White arrows indicate Fe-coatings interlayered with translocated clay along a slickenside. E) Carbonate impregnating the matrix (dark zones) of the Bkss2 horizon of a Stage II Calcic Vertisol; plane-polarized light (PPL). F) Weakly developed cross-striated clay fabric in the matrix of a Mottled Vertisol Bss horizon. G) Pedogenic clay and carbonate in the matrix of a Sandy Calcic Vertisol. Note impregnation of carbonate septarian shrinkage cracks with clay, highlighted in H. (PPL) I) Weathered rock fragment surrounded by pedogenic carbonate in the Btkss horizon of a Sandy Calcic Vertisol. J) Unweathered quartz, plagioclase and potassium feldspar grains with incipient clay coatings (granostriated fabric) in an Eolian Entisol. K-L) Bw horizon of an Eolian Inceptisol. K) Granostriated fabric on weakly weathered quartz, plagioclase, and potassium feldspar grains (white arrows) and orange porostriated fabric along void in top center. L) Granostriated and cross-striated b-fabric in an Eolian Inceptisol.

occurs as massive sand with randomly dispersed small carbonate masses. Vertically-oriented, non-branching sediment-filled tubules are interpreted as invertebrate burrows (*Skolithos* isp.).

Micromorphology. Thin sections of samples from each lithofacies and selected pedofacies were analyzed to characterize micromorphological features (Fig. 1.7). Birefringent clay fabric (b-fabric) was limited to clay coatings on skeleton grains (granostriated) in the Thin Vertisol, Fluvial Inceptisol, and Eolian Entisol pedofacies. More well-developed clay-rich Vertisols contained complex b-fabric, with granostriated, cross-striated, and pore-coating (porostriated) clays. In Stage II Calcic and Non-Calcic Thick Vertisols, shrink-swell processes led to pedobrecciation, with irregular, rotated blocks of paleosol matrix subsequently coated in translocated clay (Fig. 1.7C-D). Multi-generational desiccation cracks showed evidence of fracture healing via clay coating (Fig. 1.7D). Significant quantities of translocated clay were observed in the Sandy Calcic Vertisol subsurface horizons (Fig. 1.7G-H).

Pedogenic carbonates tend to be associated with macroscopic root traces and were rare in paleosol matrices. The Bkss horizons of the Stage II Calcic Vertisol pedofacies contained diffuse zones of micrite (Fig. 1.7I). The Sandy Calcic Vertisol was the only paleosol with extensive nodular carbonate growths, which had septarian shrinkage cracks plugged with translocated clay (Fig. 1.7G-H) due to alternations between wet and dry intervals.

Eolian paleosols show marked increases in b-fabric from Eolian Entisols, which show only rare granostraited fabric (Fig. 1.7J) to Eolian Inceptisols, which exhibit well-developed granostriated, porostriated, and cross-striated b-fabric (Fig. 1.7K-L).

Constitutive Mass-Balance Results

Bulk geochemical data for paleosols and mudstones are presented in Table A1. The clay-rich Vertisols were weathered to their lower contacts, thereby preventing assessment relative to *in situ* parent material. A proxy parent material was generated by averaging the composition of two laminated floodplain mudstones that had the same color and grain size as most of the Vertisols. The parent material for the Sandy Calcic Vertisol was not present in unweathered outcrop and therefore not sampled, so the lowest sample in the profile was used as the "parent material."

Concentrations of the immobile elements Ti and Zr are uniform in all profiles (Fig. 1.8), with < 0.15 wt. % TiO_2 and < 30 ppm Zr variation in any given paleosol. TiO_2 was selected as the immobile element for mass balance calculations because it is higher in concentration than Zr (*sensu* Driese et al., 2016). Stain (ε) calculations reveal that most profiles show between ~0-25 % volume loss with depth, with the exception that the Stage II Calcic Vertisol shows a dilation of ~13 % volume down-profile (Fig. 1.8C). The translocation function (τ) was used to calculate vertical fluxes of constituents that track climatic and pedogenic processes (Fig. 1.8D-J). Al was conserved in all profiles, with less than 4 % change in all cases. All calcic profiles show net gains in Ca, whereas the Non-Calcic Vertisols show 40-50 % loss of Ca. Most samples showed little change in Mg, the exceptions being large Mg gains in the Sandy Calcic Vertisol—likely due to variations in carbonate content—and moderate (< 10 %) losses in the Stage I Calcic and one of the Non-Calcic Vertisols. Most horizons were depleted in Na. Interestingly, the Stage II Calcic Vertisol gained 48-67 % Na relative to parent materials, with samples containing nearly 1 wt. % Na. Patterns of K were variable and stayed within 20 % of parent material

values for all samples. All profiles showed some gain of Mn with depth, with some horizons increasing by 60-100 %. Fe content was invariant with depth in all profiles.

Paleoclimate Results

Mean annual precipitation (MAP) and temperature (MAT) results are presented in Figure 1.9. The CIA-K, CIA-Kv, and CALMAG functions predict a wet sub-humid to dry humid MAP for the clay-rich Vertisols and a drier, semi-arid to sub-humid MAP for the Sandy Calcic Vertisol. Predicted MAP values are inversely proportional to observed pedogenic carbonate content across the sampled pedofacies. We attribute the disparity in MAP prediction between clay-rich Vertisols and the Sandy Calcic Vertisol pedofacies to be an artifact of grain size-dependent compositional differences rather than actual differences in paleoclimate. The coarse texture of the Sandy Calcic Vertisol would allow for more rapid precipitation of carbonates (Gile et al., 1966), and with less smectite clay and a more abundant coarse detrital fraction, would bias MAP and MAT predictions to lower values independent of climatic conditions.

The $PPM_{1.0}$ MAP predictions are higher than the traditional bulk geochemical transfer function results by as much as ~500 mm for some samples, though all values are within the estimated error for $PPM_{1.0}$. Mean annual temperature estimates using the NaK proxy and $PPM_{1.0}$ are within error for all samples and suggest a mesic to cool thermic climate.

Oxygen Isotopes

The stable isotopic composition of oxygen in calcium carbonate ($\delta^{18}O_{cc}$ VPDB) is presented in Figure 1.10 for pedogenic, tufa, and fracture-fill carbonates. Raw values are

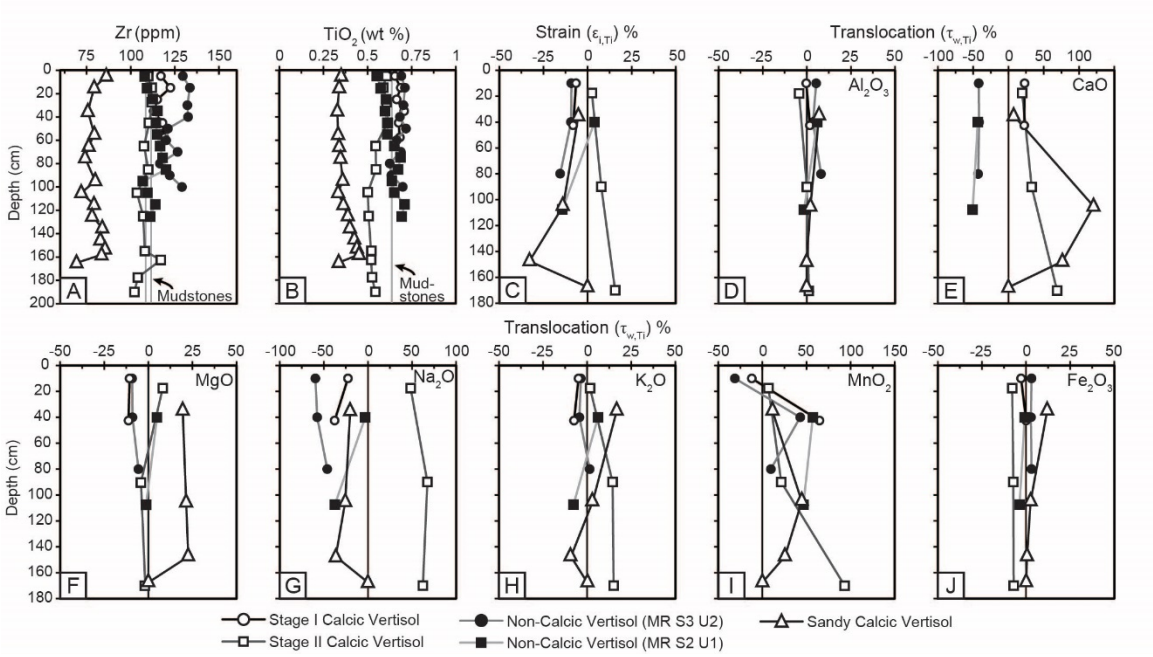

Figure 1.8. Mass-balance geochemical analysis results. Profiles symbols are identified at the base of the figure. The recalcitrant elements Zr and TiO_2 are plotted in A and B, respectively. TiO_2 shows less variation with depth and was used as an immobile reference element. The Zr and TiO_2 concentrations in mudstones used as a proxy parent material is indicated. C) Strain calculations show dilation with depth in the Stage II Calcic Vertisol and mild to moderate collapse with depth for all other paleosol types. D-J) Translocation plots for elemental constituents. The mobile element is indicated in each box and TiO_2 is used as an immobile reference. See text for discussion of translocation plots.

reported in Table A2. Overall, $\delta^{18}O_{cc}$ values are normally distributed (Shapiro-Wilk test, $p = 0.56$) with a range between –5.46 ‰ to –4.46 ‰, a mean value of –4.99 ‰ and standard deviation of 0.23. The texture of the sedimentary matrix hosting carbonate samples was binned into categories modified after NRCS texture classes and include silty clay, sandy clay, clayey silt, sandy silt, and clayey sand (Fig. 1.10A). Tufa and fracture-fill carbonate samples were designated as their own "texture classes." Analysis of variance (ANOVA) showed that mean $\delta^{18}O_{cc}$ values are not identical across matrix texture classes ($p < 0.001$). Carbonate associations were grouped into classes consisting of nodule, rhizolith, tufa, and fracture-fill (Fig. 1.10B). ANOVA again showed that mean

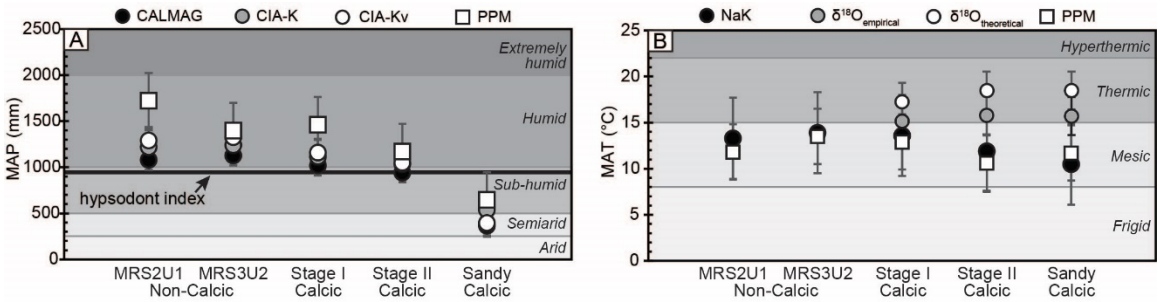

Figure 1.9. Paleoclimate results for selected pedofacies. A) Mean annual precipitation (MAP) values calculated using bulk geochemical pedotransfer functions. The hypsodont index predicts MAP based on the proportion of hypsodont taxa in the Coffee Ranch faunal assemblage within error of some estimates (Fraser and Theodore, 2013). B) Mean annual temperature (MAT) values calculated using transfer functions based on the bulk geochemistry of paleosols and the $\delta^{18}O$ of pedogenic carbonates. See text for details of $\delta^{18}O$ functions. PPM = paleosol-paleoclimate model, which simultaneously predicts MAP and MAT using paleosol geochemistry (Stinchcomb et al., 2016). All pedofacies are Vertisols. Error bars are standard errors given by regression analysis for CALMAG, CIA-K, CIA-K_v and NaK, and modelled error for $\delta^{18}O$ and PPM functions.

$\delta^{18}O_{cc}$ values were not identical across association classes ($p < 0.001$). Tukey's HSD was performed post-hoc and revealed significant differences between the following pairs, with the more ^{18}O-enriched class listed first for each pair: fracture-fill/tufa, fracture-fill/silty clay, clayey sand/tufa, and clayey sand/silty clay.

A weak but significant positive correlation was found between the depth of carbonate samples in paleosol profiles and $\delta^{18}O_{cc}$ ($r^2 = 0.28$, $p < 0.001$; Fig. 1.10C), though we note that all profiles were eroded from above and therefore depth values are necessarily underestimates. The down-profile shift is lower in magnitude and inverse in slope of the expected relationship between $\delta^{18}O_{cc}$ and soil depth for near-surface evaporative enrichment (e.g., Quade et al., 1989).

MAT values were calculated using the mean $\delta^{18}O_{cc}$ value of triplicate analyses of pedogenic carbonate samples. Because little overall variation is observed in $\delta^{18}O_{cc}$ values, MAT estimates are plotted as the average of all samples from each paleosol with

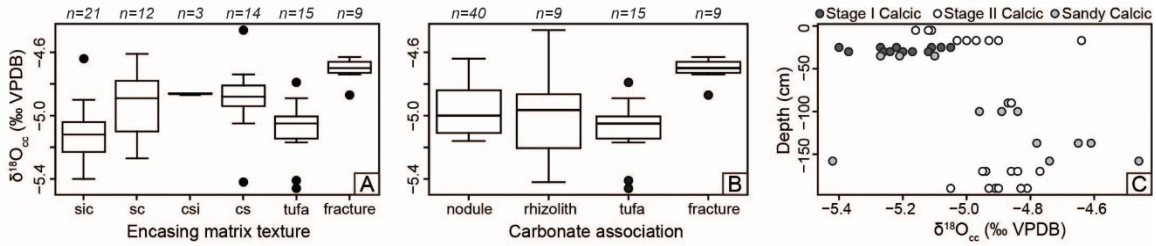

Figure 1.10. Oxygen stable isotopic values ($\delta^{18}O_{cc}$) of pedogenic, tufa and fracture-fill carbonates. A) Box plot of $\delta^{18}O_{cc}$ by sedimentary texture of the encasing matrix. Tufa samples were recovered from a ~2 m thick, massive limestone. Fracture-fill samples cross-cut strata of varying textures. See text for pairwise statistical comparisons. B) Box plot of $\delta^{18}O_{cc}$ by carbonate association. All nodules and rhizoliths were recovered *in situ* from paleosol profiles. See text for pairwise comparisons. C) Cross plot of depth versus $\delta^{18}O_{cc}$. A weak but significant relationship exists for all data and is primarily driven by samples from the Sandy Calcic Vertisol pedofacies.

the estimated standard error from Hyland and Sheldon (2013) (Fig. 1.9). The theoretical MAT function consistently predicts values 1.7-3.0 °C higher than the empirical function. Overall, temperature predictions range from 17-19.2 °C and 15.0-16.3 °C for pedogenic carbonates using the theoretical and empirical functions, respectively. The empirical function results are within error of bulk geochemical estimates of MAT.

Magnetostratigraphy and Age Model

We measured 22 samples extracted from fine grained units of the MSL lithofacies: Vertisols formed on the Mm lithofacies, fine-grained portions of the Sr lithofacies, and the vitric tuff interbedded in fluvial channels at Mendota Ranch outcrops (Fig. 1.2). Data from all calculated lines are plotted in Figure 1.11 (see Tables A3 and A4 for all sample data and all means, respectively). All samples exhibited normal polarity. The mean geographic declination and inclination for all samples from Coffee Ranch and Mendota Ranch are nearly identical and are statistically indistinguishable (Table A4). Based on this, as well as lithologic similarities, we interpret the Coffee Ranch and

Mendota Ranch sections to be age equivalent. The mean geographic declination and inclination for all Coffee Ranch and Mendota Ranch sites is 351.9° and 46.5° (n = 22, a95 = 8.8; Table A4). The virtual geomagnetic pole for all sites is 81.9°N and 129.4°E (n = 22, K = 11.8, A95 = 9.4), which is indistinguishable from the reconstructed global apparent polar wander path for North America between 0 and 10 Ma (Torsvik et al., 2008).

Unlike Lindsay et al. (1975), we did not document any samples of reversed polarity; however, our analyses also indicate that the CRA was deposited within normal polarity. Based on the age estimate of 6.62 Ma for the CRA (Passey et al., 2002), we interpret the Coffee Ranch and Mendota Ranch sections to have been deposited within chron C3An.2n. Lindsay et al. (1975) documented a reversal 15 m below the CRA, which we interpret as the base of chron C3An.2n.

Using the age estimate for the CRA of 6.62 ± 0.08 Ma and the age for the base of C3An.2n (6.733 Ma in Ogg, 2012) and Lindsay et al.'s (1975) documentation of a reversal 15 meters below the CRA, we were able to estimate the sedimentation rate for the Coffee Ranch and Mendota Ranch Sections to be 0.13 meters per thousand years. Based on this sedimentation rate and a total stratigraphic thickness of 36 composite meters for the Coffee Ranch and Mendota Ranch sections, we estimate that the strata were deposited over 277 kyr from ~6.70 to ~6.42 Ma.

Discussion

The lithofacies and styles of pedogenesis interpreted in this study are consistent with a much wetter climate in the southern Great Plains during the late Miocene than today. Fluvial style is typical of moderate-scale meandering river systems in the North

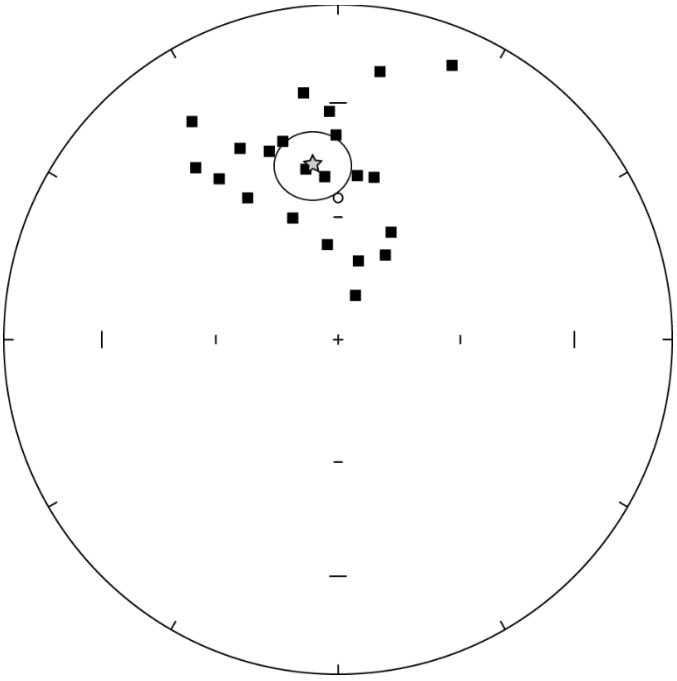

Figure 1.11. Equal-area plot of characteristic magnetization directions calculated from all lines measured in this study. Star indicates the Fisher mean direction. Ellipse around mean direction represents 95 % confidence cone (Fisher, 1953). Open circle indicates present axial dipole.

American continental interior, with tributary and trunk channels containing sedimentary features consistent with episodically variable discharge—likely seasonal—and subaerial exposure. Coarse clasts are limited to reworked carbonate nodules, bank collapse blocks or vertebrate fossils, as the depocenter is far from any upland source areas (Gustavson and Winkler, 1988; Gustavson, 1996). Proximal to distal floodplain facies are represented by a spectrum of paleosols ranging from weakly developed, sandy Inceptisols to increasingly mature Vertisols (Bown and Kraus, 1987), with occasional microenvironments containing ponded water or eolian deposition.

The presence of Vertisols in superposed floodplain suites corroborates sedimentary evidence of episodically-variable discharge in stream channels, as Vertisols require seasonal water deficit to drive shrink-swell pedoturbation (Nordt et al., 2004).

Micromorphologic indicators of alternating wet and dry intervals include pedobrecciation, translocated clay filling septarian cracks in carbonate nodules, and complex b-fabric juxtaposed with carbonate nodules.

Eolian deposits were likely sourced from seasonal exposure of fluvial channel sands (Forman et al., 2001). In the modern Great Plains, prevailing winds have sufficient velocity to entrain sand from surfaces with less than ~30 % vegetation cover (Pye and Tsoar, 1990) . The suite of low-flow indicators observed in the channel facies (Fig. 1.4) demonstrate that episodic exposure of non-vegetated channel bases would provide sufficient sediment supply for eolian mobilization. Red to tan quartz sand was observed in paleosol macrovoids, root traces, and as passive infills of invertebrate burrows in nearly all floodplain facies, often without the presence of discrete eolian deposits in stratigraphic superposition (e.g., Fig. 1.3G, 1.8C). Such cryptic deposits are evidence that channel exposure occurred regularly—likely seasonally—but for short enough durations that eolian sediments were incorporated into paleosols and open root traces without burying the deposits completely.

Most eolian paleosols are weakly formed Entisols developed over relatively short time intervals (10^0-10^2 yr; Birkeland, 1999). The Eolian Inceptisol and Fluvial Inceptisol pedofacies would have formed during depositional hiatuses on the order of 10^2 yr based on the presence of a Bw horizon (Birkeland, 1999). For other pedofacies, trends in geochemical behavior aid in the interpretation of pedogenic maturity and weathering pathways.

The combination of strain and Ca translocation allow for the four different pedofacies to be placed into three pedogenic groupings (Fig. 1.12). In the first, the silty

Stage I Calcic Vertisol and the coarser Sandy Calcic Vertisol accumulated Ca associated with pedogenic carbonate. Moderate to substantial loss of pore space occurred as a result of feldspar weathering, and the lack of a sufficiently cohesive matrix resulted in volume collapse. In the second pedogenic grouping, the more clay-rich Stage II Calcic Vertisol also accumulated Ca with pedogenic carbonate but net matrix dilation occurred as a result of shrink-swell behavior in clays or by generation of porosity as skeletal grains decayed. The third grouping consists of decalcified paleosols that variably experienced dilation or collapse during mineral weathering and shrink-swell processes.

The coexistence of both calcifying and decalcifying paleosols under the same climatic conditions points to landscape-scale processes as drivers of weathering pathways within a climate regime near the continental udic-ustic pedoclimate boundary. In modern North America, soils in the udic soil moisture regime are defined as having less than 90 cumulative days where the soil is dry at 50 cm depth (Soil Survey Staff, 2014). These soils tend to have positive moisture budgets, and are therefore less frequently subjected to moisture stress. The number of dry days varies for ustic soils depending on soil temperature, but the concept behind their classification is that they all experience significant moisture stress for more protracted durations than udic soils, which requires vegetation associated with ustic soils to have adaptations to prevent moisture loss (Soil Survey Staff, 2014).

Calcified Vertisols observed in this study required well-drained conditions to allow vegetative pumping—likely by trees and shrubs—to sufficiently concentrate Ca^{2+} in the rhizosphere (Zamanian et al., 2016). In contrast, the decalcified Vertisols would have formed in slightly less well-drained conditions, retaining water for longer durations

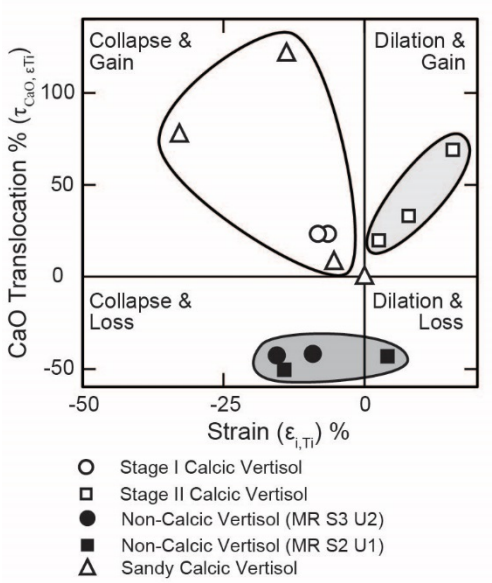

Figure 1.12. Cross-plot of Ca translocation vs. strain. Three pedogenic pathways are interpreted, wherein the Stage I and Sandy Calcic Vertisols experienced volumetric collapse and progressive Ca gain; the Stage II Calcic Vertisol experienced progressive volumetric expansion and Ca gain; and Non-Calcic Vertisols experienced Ca loss and variably manifest volumetric collapse or expansion.

and inhibiting rhizolith mineralization. Seasonal drainage of the low-lying, decalcified paleosols would have occurred for less time, still allowing for the development of slickensides and complex b-fabric (Fig. 1.7). This interpretation is supported by the presence of laminated mudstones containing partially oxidized leaf litter directly above the Non-Calcic Vertisol type profile (MR section 3 unit 2).

While landscape-scale variations in soil hydrology are evident from comparisons of pedofacies, we note that no single, continuous paleocatena was observable in the study area. This is the result of a combination of intermittent outcrop exposure and variable erosional truncation associated with fluvial deposition or landscape deflation in the late Miocene. Lateral variation in Vertisols can be particularly profound compared to other soil orders, resulting in physical and chemical profiles that vary along Gilgai

microtopography (e.g., Nordt et al., 2004). However, field description of every paleosol encountered in the stratigraphy allowed for a total of nine pedofacies to be delineated in just 30 stratigraphic meters. These include six varieties of Vertic paleosols that are interpreted to be the manifestations of lateral landscape positions on a single, hypothetical catenary transect. Thus, we are confident that the environmental and climatic interpretations presented in this study capture the natural variability associated with such heterogeneous soil types.

Mass-balance geochemistry also allows for some comparisons to be made between the late Miocene paleosols and analogous modern soils. Modern Vertisols in Texas tend to be leached of Mn in areas with > 1150 mm MAP, whereas those forming in < 1150 mm accumulate Mn as MnO_2 (Stiles et al., 2003). All paleosols exhibited some gain of Mn with depth (Fig. 1.8), which places an upper limit of 1150 mm MAP for the paleosols in this study. This value agrees with the results of the CALMAG and CIA-K and functions for the clay-rich Vertisols, but is substantially less than the $PPM_{1.0}$ MAP predictions (Fig. 1.9).

Stiles et al. (2003) also found that translocation of Fe progressively increases with time (up to 35 kyr) at a slower rate than mobile bases such as Ca and Mg, which can establish climatically-driven vertical redistributions within as little as 0.4 kyr. Micromorphologic features associated with Fe translocation (Driese, 2004) were absent in all paleosol thin sections, corroborating mass-balance results that showed no trend in Fe minerals in any of the paleosol profiles. The lack of translocated Fe and presence of clear trends in Ca and Mg suggest that the paleosols observed in this study formed over

intervals of 10^3-10^4 yr, which is in line with the time required to form most Bt and Bk horizons (Birkeland, 1999).

Quantitative MAP predictions from the clay-rich Vertisols are slightly higher than an independent estimate of 992 mm, calculated from the proportion of hypsodont taxa in the Coffee Ranch fossil assemblage (Fraser and Theodor, 2013). The hypsodont-MAP index was calibrated on modern African faunal communities, which tend to contain more hypsodont taxa in open environments as a response to the increased presence of grass phytoliths and dust on foliage. Abundant evidence of eolian sediment was observed in the Coffee Ranch and Mendota Ranch stratigraphy. This observation suggests that windblown sand and silt were common on the landscapes and resulted in increased quantities of dust on vegetation, which in turn may have caused increased hypsodonty in the mammalian taxa, even though the inferred vegetation likely consisted of a bushland or woody savannah in which grass was not the primary constituent (Fox and Koch, 2004; Fraser and Theodor, 2013).

Predictions of MAT using bulk geochemical methods converge on values within the mesic temperature regime, with error bars for the clay-rich Vertisols extending into the thermic zone. The similarity between the NaK and $PPM_{1.0}$ MAT estimations is unsurprising given that $PPM_{1.0}$ temperature prediction is most heavily weighted by Na_2O and K_2O concentrations (Stinchcomb et al., 2016). In contrast, independent results from the $\delta^{18}O_{cc}$-MAT transfer functions yield higher values that range from 17-19.2 °C and 15.0-16.3 °C for the theoretical and empirical transfer functions of Dworkin et al. (2005), respectively. Hyland and Sheldon (2013) estimated that the error on the $\delta^{18}O_{cc}$-MAT empirical function to be on the order of 4.1 °C. This value is probably similar for the

theoretical function and would place all isotope-based temperature predictions within the warm mesic to thermic temperature regime. These values are similar to modern MAT near the Canadian River Valley in the Texas Panhandle, which ranges from 13.9-17.8 °C (PRISM Climate Group, 2004).

The presence of crocodilians and large tortoises in the Coffee Ranch bonebed suggest that MAT was either warmer or that seasonal variability in temperature was much lower in the late Miocene than today. Analyses of Neogene *Gomphotherium* tusk growth lines suggest that strong seasonal variation of temperature, precipitation, or both, was established in the Southern High Plains by the late Miocene (Fox and Fisher, 2004). Similarly, Sharp and Cerling (1998) observed intra-annual variations in the $\delta^{18}O$ of tooth enamel in a Coffee Ranch equid. After fitting a sinusoidal smoothing curve to data from 1962-1976, Sharp and Cerling (1998) determined: 1) that late Miocene meteoric water $\delta^{18}O$ ($\delta^{18}O_{mw}$) was roughly 3-4 ‰ more positive than modern values at the Waco, TX, International Atomic Energy Agency (IAEA) monitoring site, and 2) intra-annual variations of late Miocene $\delta^{18}O_{mw}$ in the Panhandle were similar in magnitude and modality to modern $\delta^{18}O_{mw}$ at Waco, TX. These findings suggest that seasonal variations in temperature did exist in the Neogene and that MAT estimations from all of the MAT transfer functions are underestimates.

Modern $\delta^{18}O$ of precipitation at Coffee Ranch and Waco, TX, were calculated using the Online Isotopes in Precipitation Calculator (waterisotopes.org). Values at Coffee Ranch are 1.4 ± 0.2 ‰ more negative than Waco using estimates of both mean annual values (Bowen and Revenaugh, 2003) and monthly values for August (Bowen et al., 2005), which is the most $\delta^{18}O$-enriched time of the year and the most likely time for

pedogenic carbonate formation (Breecker et al., 2009). If late Miocene $\delta^{18}O_{mw}$ values at Coffee Ranch were more positive than modern values at Waco (Sharp and Cerling, 1998), and if the spatial distribution of $\delta^{18}O_{mw}$ values were similar to modern conditions, Coffee Ranch $\delta^{18}O_{mw}$ would be upwards of 4-5.5 ‰ more positive in the late Miocene than today. If these values are accurate, it would suggest that the MAT would have been substantially higher in the late Miocene if the modern spatial correlation between $\delta^{18}O$ and MAT existed at the time.

Recent studies of precipitation changes associated with global warming have found that the amount of rainfall dramatically increases with global temperature (Neelin et al., 2017), and that precipitation events become more intense at mid-latitudes (Karl and Knight, 1998; Groisman et al., 1999). In a warmer world, overall atmospheric water vapor also increases (Easterling et al., 2000). These factors strongly suggest that the spatial relationship between $\delta^{18}O_{mw}$ and MAT has the potential to change with climate due to modifications in the degree of Rayleigh fractionation of water vapor transported over the continents (Gat, 1996). Further, moisture sources in the Gulf of Mexico had more positive $\delta^{18}O$ values in the late Miocene as a result of largely unrestricted flow through the Panama Seaway (Keigwin, 1982; Haug and Tiedemann, 1998) and reduced Northern Hemisphere ice volume (Zachos et al., 2001). From these lines of evidence, we conclude that the $\delta^{18}O$-MAT transfer functions are not applicable in this study, which may be the reason why MAT estimations are below values that temperature sensitive taxa in the Coffee Ranch fauna would require.

Taken together, climatic and pedogenic environments of the late Miocene Texas Panhandle were considerably wetter than today (900-1150 mm/yr in the Miocene vs. 400-

700 mm/yr in modern), and at least moderately warmer than present. Analogous modern soils to the paleosols in this study occur in modern central Texas, near the udic-ustic boundary (Nordt et al., 2004). The current boundary between relatively wet udic soils of the east, and drier ustic and aridic soils of the central and western Great Plains, runs generally south-north from the Texas coastal plain to North Dakota (Salley et al., 2016) and is strongly controlled by MAP. Thus, the presence of the paleosols described in this study with a paleo-MAP of 900-1150 mm indicates a significant westward shift of at least the southern portion of the udic-ustic boundary by ca. 400 km in the late Miocene. The relatively high MAP was perhaps driven by an amplified monsoon from the Gulf of Mexico that drove storm tracks deeper into the continental interior. Such conditions are in line with global reconstructions of vegetation and climate, which suggest a warmer and wetter world existed from the middle to late Miocene (Pound et al., 2012). The MAP values estimated in this study should be incorporated into future efforts to model late Miocene climate, as quantitative estimates of precipitation are sparse for central North America for much of the Miocene (e.g., Bradshaw et al., 2012; Pound et al., 2012; Bradshaw et al., 2015).

Finally, the climate reconstruction in this study helps to explain previous interpretations that relatively little C_4 vegetation was present at Coffee Ranch in the late Miocene (e.g., Fox and Koch, 2004). The selectivity of C_4 photosynthetic pathways over C_3 photosynthesis occurs at low atmospheric *p*CO2 and in arid environments (Ehleringer et al., 1997). Climate conditions were likely too wet and possibly not hot enough to drive a cross-over to C_4-dominated vegetation until later in the Neogene (e.g., Fox and Koch, 2003). The high degree of seasonality suggested by pedogenic features, including

slickensides and interwoven clay and carbonate complexes, indicate that moisture stress in the warm growing season was at least one factor that allowed for the presence of C_4 vegetation. Because only calcic paleosols have been used in previous estimations of C_4 abundance at Coffee Ranch (Fox and Koch, 2003, 2004), it is yet unknown whether the landscape-scale differences in drainage associated with calcic and non-calcic paleosols would have influenced the lateral distribution of C_4 biomass in the late Miocene.

Conclusions

Depositional environments in and around Coffee Ranch in the Texas Panhandle during the late Miocene consisted of lateral floodplain suites and intermittent eolian sand sheet deposition, volcanic ash, riverine tufa, and associated paleosols. The paleosols, which were divided into nine pedofacies, indicate the precipitation was likely seasonal with pronounced intervals with little to no rainfall. Mass-balance geochemistry demonstrates that the paleosols in the succession either gained or lost Ca through carbonate precipitation or leaching, with variable volumetric changes due to mineral weathering. These pedogenic trends are consistent with soil formation near the transitional zone of udic-ustic pedoclimates. This qualitative interpretation of climate agrees with MAP estimates from paleosol transfer functions, which indicate that the late Miocene was roughly twice as wet as modern conditions. Mean annual temperatures were warmer than today, based on the presence of crocodilians and large tortoises in the Coffee Ranch fauna. However, pedotransfer functions based on the element chemistry of paleosol B horizons and $\delta^{18}O$ of pedogenic carbonates underestimated MAT values. Taken together, these results suggest that in the late Miocene, the longitudinal moisture

gradient in the southern midcontinent was shifted to the west by several hundred kilometers.

Acknowledgments

We are grateful to the Wheeler, Coffee, and Abraham families for providing access to field areas. Substantial field assistance was provided by Yohan Letourmy and Martín Schwed. Stable isotopic analyses were performed by Ren Zhang at the Baylor University Stable Isotope Laboratory. We thank Associate Editor Isabel Montañez, Dennis Terry, and an anonymous reviewer for comments that greatly improved the manuscript. Funding support was provided by graduate student research grants from the Geological Society of America and SEPM (to WEL) and the Baylor University Department of Geosciences.

CHAPTER THREE

The Early Miocene Critical Zone at Karungu, Western Kenya: An Equatorial, Open Habitat with Few Primate Remains

This chapter published as: Lukens, W.E., Lehmann, T., Driese, S.G., Peppe, D.J., Fox, D.L., and McNulty, K., *under review*, The Early Miocene Critical Zone at Karungu, Western Kenya: an equatorial, open habitat with few primate remains: *Frontiers in Earth Science*.

Abstract

Early Miocene outcrops near Karungu, Western Kenya, preserve a range of fluvio-lacustrine, lowland landscapes that contain abundant fossils of terrestrial and aquatic vertebrates. Primates are notably rare among these remains, although nearby early Miocene strata on Rusinga Island contain a rich assemblage of fossilized catarrhines and strepsirrhines. To explore possible environmental controls on the occurrence of early Miocene primates, we performed a deep-time Critical Zone (DTCZ) reconstruction focused on floodplain paleosols at the Ngira locality in Karungu. We specifically focused on a single stratigraphic unit (NG15), which preserves moderately developed paleosols that contain a microvertebrate fossil assemblage. Although similarities between deposits at Karungu and Rusinga Island are commonly assumed, physical sedimentary processes, vegetative cover, soil hydrology, and some aspects of climate state are notably different between the two areas. Estimates of paleoclimate parameters using paleosol B horizon elemental chemistry and morphologic properties are consistent with seasonal, dry subhumid conditions, occasional waterlogging, and herbaceous vegetation. The reconstructed small mammal community indicates periodic waterlogging and open-

canopy conditions. Based on the presence of herbaceous root traces, abundant microcharcoal, and pedogenic carbonates with high stable carbon isotope ratios, we interpret NG15 to have formed under a warm, seasonally dry, open riparian woodland to wooded grassland, in which at least a subset of the vegetation was likely C_4 biomass. Our results, coupled with previous paleoenvironmental interpretations for deposits on Rusinga Island, demonstrate that there was considerable environmental heterogeneity ranging from open to closed habitats in the early Miocene. We hypothesize that the relative paucity of primates at Karungu was driven by their environmental preference for locally abundant closed canopy vegetation, which was likely absent at Karungu, at least during the NG15 interval if not also earlier and later intervals that have not yet been studied in as much detail.

Introduction

Early Miocene deposits in the Nyanza rift valley of East Africa preserve a rich assemblage of mammalian remains, with nearly a century of research there focused on the evolutionary context of apes (e.g., Hopwood, 1933; Andrews, 1978; Walker et al., 1993; McNulty et al., 2007, 2015). The early Miocene is recognized as a key interval in the development of anatomical and behavioral adaptations fundamental to interpreting the origin of the human lineage (Gebo et al., 1997; Michel et al., 2014; McNulty et al., 2015; Begun, 2015). These include aspects of the axial skeleton and extremities shared between early hominins and the primitive ape *Ekembo* (Lovejoy, 2009; Lovejoy et al., 2009a, 2009b), frequent use of upright posture in *Morotopithecus* (Sanders and Bodenbender, 1994; Gebo et al., 1997; MacLatchy et al., 2000), advanced subnasal morphology in *Rangwapithecus* (Andrews, 1978; McNulty, 2003), and large body size and prolonged

life history in *Afropithecus*, *Ekembo*, and *Morotopithecus* (Kelley, 1997, 2002). Further, evidence of folivory in *Rangwapithecus* and *Morotopithecus* (Kay and Ungar, 1997; MacLatchy et al., 2010; McNulty et al., 2015) and durophagy in *Afropithecus* (Leakey and Walker, 1997) suggest specialized dietary adaptations existed between clades and locations. Understanding the variety of paleoenvironments and paleoclimate zones in East Africa in the early Miocene is essential to differentiate the roles of environmental pressures (e.g., vegetation and climate) from biotic factors (e.g., niche partitioning, biogeography, and sexual selection) as selection mechanisms for derived traits in hominoids and apes.

Longstanding interpretations suggest that wooded or forested habitats were pervasive across eastern Africa until the late Miocene at ca. 8–10 Ma (Cerling et al., 1998; Jacobs et al., 1999, 2010; Uno et al., 2016), implying that unchanging habitats allowed biotic factors to drive evolution of early hominoid lineages through most of the early and middle Miocene. However, a few studies have indicated the presence of open canopy habitats based on environmental interpretations from paleosols and stable isotopes from early Miocene strata at Karungu and Rusinga Island in western Kenya (Bestland and Krull, 1999; Forbes et al., 2004; Driese et al., 2016). A significant proportion of C_4 vegetation, which is characteristic of open canopy habitats today, has been interpreted for middle to late Miocene strata in the Tugen Hills, central Kenya (Kingston et al., 1994). These studies suggest that open canopy environments may have been important components of landscapes prior to the late Miocene.

Herein, we investigate the evidence for open canopy environments at Karungu by using paleopedology, sedimentology, and microvertebrate paleontology. Although

hundreds of mammalian specimens have been recovered from Karungu (Andrews, 1911; Pickford, 1981), only a small number of the fossils are catarrhine primates, including a tooth of *Dendropithecus* and a few specimens identified as cf. *Ekembo* (Clark and Leakey, 1951; McNulty et al., 2015). Pickford (1981) argued that the mammals represented in the Karungu fauna are generally similar to fauna of the Hiwegi Formation on Rusinga Island (Fig. 2.1), which contains abundant, well-preserved fossil catarrhine primates including *Dendropithecus, Ekembo*, *Nyanzapithecus,* and *Limnopithecus*, (Leakey, 1943; Clark and Leakey, 1951; Kelley, 1986; Pickford, 1986; Walker et al., 1993; Kelley, 1993; Harrison, 2010; Michel et al., 2014; McNulty et al., 2015). Based on assessments of the faunas at Karungu and from the entire the Hiwegi Formation on Rusinga Island, Nesbit Evans et al. (1981) interpreted them to represent similar paleoecological conditions. Driese et al. (2016) argued from analyses of paleosols, sedimentology, stable isotopes, and fauna at the Ngira locality at Karungu, that the paleovegetation and paleoenvironments of Karungu were similar to the Grit and lower Fossil Bed Members of the Hiwegi Formation on Rusinga Island. Based on this similarity, Driese et al. (2016) suggested that faunal differences between Karungu and the lower Hiwegi Formation were unlikely driven by paleoenvironmental differences. Forbes et al. (2004), however, used paleopedology and stable isotope analyses to interpret humid climate conditions for both Karungu and the Wayando Formation, which underlies the Hiwegi Formation on Rusinga Island. In each case, the interpretation of similar paleoenvironments at Karungu, which generally lacks primate fossils, and deposits on Rusinga Island, which preserve abundant primate fossils, suggests differences in the

fossil record are due to biotic pressures or preferences rather than abiotic factors such as paleoenvironmental setting.

We reexamine the hypothesis that differences in the abundance of primates between Karungu and Rusinga Island are driven by biotic or abiotic factors by studying an interval of paleosols at the Ngira locality in Karungu as a spatio-temporal slice through the dynamic deep-time Critical Zone (DTCZ) from western Kenya in the early Miocene (Fig. 2.1). The Critical Zone is the net result of interactions between the lithosphere, atmosphere, hydrosphere, and biosphere, and is preserved as an integrated substrate in the pedosphere (Brantley et al., 2007) . The Critical Zone concept has been translated to the terrestrial stratigraphic record through DTCZ analysis, which utilizes tools developed and applied in sedimentology, paleopedology, and paleoecology (Nordt et al., 2012; Nordt and Driese, 2013). Application of DTCZ concepts to Neogene sites in East Africa will advance the interpretive capacity of environmental and climatic variables from strata that preserve hominoid remains.

Geologic Setting

Early Miocene deposits at Karungu accumulated in a small graben on the southern flank of the Nyanza Rift system (Drake et al., 1988). Sedimentary deposits associated with the Kisingiri volcanic complex include Mfangano and Rusinga Islands, which are on the north side of the Kisingiri caldera roughly 50 km from Karungu. The Kaniamwia fault separates Miocene deposits around Karungu from Kisingiri volcaniclastics to the north (Fig. 2.1) (King et al., 1972; Drake et al., 1988; Bestland et al., 1995). Precambrian igneous and metamorphic basement surrounds the Nyanza Rift in western Kenya (Smith and Mosley, 1993).

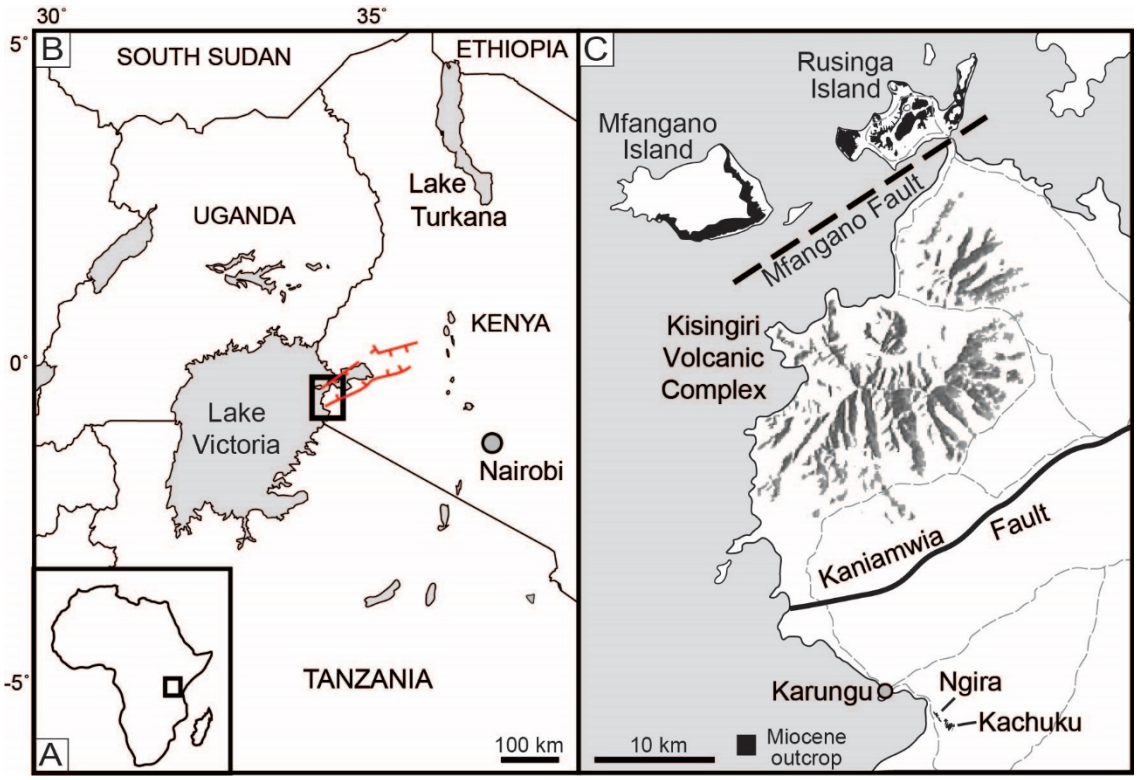

Figure 2.1. Location of study site A) on the African continent, and B) within western Kenya. Red lines indicate the boundary faults of the Nyanza rift. C) Ngira and Kachucku together comprise the Karungu outcrop areas, located roughly 50 km south of Rusinga and Mfangano Islands. Light grey dashed lines are roads. Modified after Bestland et al. (1995), Geraads et al. (2016), and Driese et al. (2016).

Fossiliferous deposits at Karungu consist of two distinct outcrop areas: Ngira and Kachuku. In this study, we focus on the Ngira locality. The stratigraphy and sedimentary environments at Ngira were first documented by Oswald (1914) and were subsequently reexamined by Forbes et al. (2004) and Driese et al. (2016). We follow the stratigraphic descriptions of Driese et al. (2016), which are generally similar to the previous studies (Fig. 2.2). The 50 m of strata at Ngira are divided into units based on major depositional packages. The base of the section is a highly weathered Vertisol with oxisolic properties and is unconformably capped by lacustrine shoreline sandstones (Driese et al., 2016). Fluvial and lacustrine facies are interstratified throughout the section and include fluvial

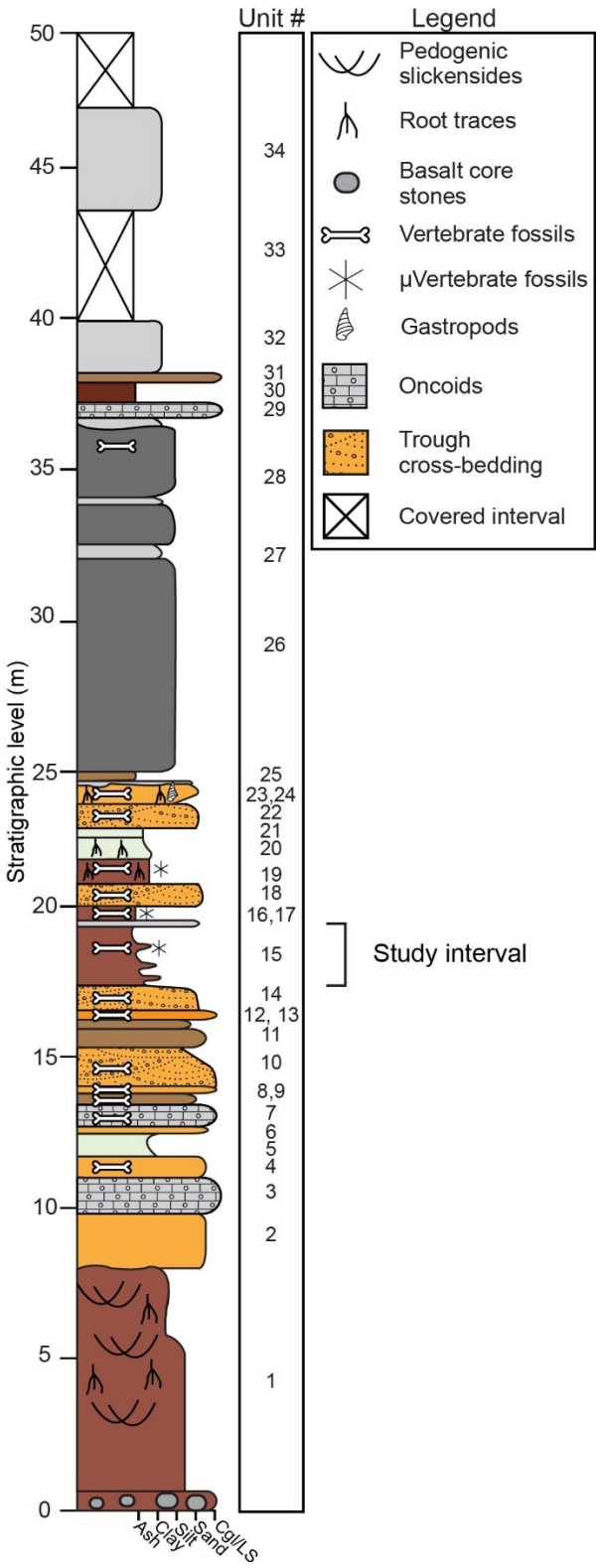

Figure 2.2. Stratigraphic section at Ngira (after Driese et al., 2016). The current study focuses on paleosols within unit 15. Driese et al. (2016) previously examined paleosols in units 1, 19, and 20.

channel sandstones, pedogenically-modified mudstones parented from alluvium and exposed lacustrine mud, and a succession of deep-water lacustrine turbidites that cap the section (Driese et al., 2016). For this study, we focus on unit 15 because it contains pedogenic features, a microfossil assemblage, and carbonate nodules, thus allowing for reconstruction of climatic and ecologic properties through multiple, independent methodologies.

Geochronologic control for Ngira is based on two K-Ar dates on a biotite tuff (unit 25), which yielded ages of 17.7 ± 0.06 and 17.5 ± 0.2 Ma (Drake et al., 1988). However, recent geochronologic analyses of ashes erupted from the Kisingiri complex and deposited on Rusinga Island suggest that the K-Ar total fusion method used by Drake et al. (1988) may not be accurate as a result of post-depositional alteration (McCollum et al., 2013; Peppe et al., 2017). Regardless, numerous analyses of the Karungu fauna are consistent with an early Miocene age (Pickford, 1981, 1986). Re-dating of the deposits at Karungu is underway as part of the Research on East African Catarrhine and Hominoid Evolution (REACHE) project.

Methods

Field Methods

Stratigraphy. Each stratigraphic unit at Ngira was identified in the field at the location described by Driese et al. (2016) using field photos, field notes, and GPS coordinates. For this study, unit 15, hereafter referred to as NG15, was identified and traced laterally using sandstone units that demarcate the top and bottom of the unit. In the location described by Driese et al. (2016), NG15 lacked pedogenic features and consisted of interbedded fluvial sand and silt. Roughly 100 m lateral to that position, however, the

interval was found to contain abundant microvertebrate fossils in a mudstone with pedogenic features.

Paleontology. Following the systematic surface collection procedure developed in the framework of the REACHE project, the area of interest was surveyed using flagging nails to visualize bone concentration. A 12 m² grid was established over the area including the microfossil assemblage, centered around 36M 632912, 9904780 (UTM, WGS84). Within this grid, an exhaustive collection of paleontological remains was performed. Sediment on the surface of the squares was swept and sieved, while the immediate area around the grid was surveyed for identifiable specimens (i.e., surface collection). All items were bagged according to their grid cell. The grid was the basis for the ensuing subsurface excavations, and 11 squares (1x1 m) of the grid were actually excavated. Squares were excavated in arbitrary 10 cm intervals measured from the overlying sandstone unit (NG16) to a depth of 80 cm. Bulk sediment from each depth interval in each grid cell was then sieved on site (5 mm and 2 mm opening) and every biological element recovered was bagged and labeled according to its depth interval and grid cell.

Fossils systematically excavated from NG15 were compared to surface collections made at Ngira over multiple field seasons (2010, 2012, 2013, 2015) in the framework of the REACHE project (Lehmann et al., 2014), and also to the historical collections housed at the National Museums of Kenya in Nairobi (NMK). These surface collections are assumed to record a time-averaged faunal signal, as they were sampled over 25 stratigraphic meters of fluvial sands, gravels, and fluvio-lacustrine mudstones at Ngira (Driese et al., 2016). Nevertheless, the sample size is large enough to capture the

conditions during most of the time of accumulation (Olszewski, 1999) and can be used in broad comparisons between early Miocene localities. All fossils were identified to the lowest taxonomic level possible with regard to anatomical element and taxon. In order to measure the taxonomic structure and composition of the collected fauna, the number of individual specimens (NISP) was calculated (Lyman, 2008). For the purpose of the present paper, our comparisons focused on small mammals, whose body size is inferred to be equal to or less than that of *Megapedetes pentadactylus* (a fossil rodent related to the springhare), which was the largest mammal found during excavations of NG15.

Paleopedology. Two paleosol profiles were trenched into fresh rock through NG15. A trench was excavated through the microfossil collection grid (profile NG15-A) after fossil surveys were completed. A second profile was described ca. 3 m lateral to the fossil excavation (profile NG15-B) after initial observations indicated that paleosol horizons appeared to vary laterally. By describing a pair of trenches, we sought to generate a better understanding of the local sedimentologic and pedogenic conditions that lead to the preservation of the microfossil assemblage. Sedimentologic and pedogenic features were described in both profiles using a modification of USDA-NRCS terminology (Schoeneberger, 2002), and include grain size, horizonation, bounding contacts, ped structure, color, mineralizations, and root traces. Serial bulk and oriented samples were recovered through each horizon of NG15-B, and selected horizons were sampled from NG15-A for comparison.

Laboratory Methods

Elemental geochemistry of bulk paleosol samples was characterized using two methods: 1) untreated, whole-sample assays using fused-bead ICP-AES and ICP-MS analysis for major and trace elements, respectively, at ALS Global (alsglobal.com); and 2) whole-sample assays of decarbonated aliquots of the same samples using X-ray fluorescence (XRF) for major element analysis at Baylor University. Samples sent to ALS Global were also analyzed for loss on ignition (LOI) at 1000°C. Samples analyzed in-house at Baylor University were powdered and homogenized, decarbonated using 10% HCl, and neutralized using repeated rinsing with de-ionized water. The decarbonated samples were then re-ground, homogenized, fused into glass beads, and analyzed for major element concentrations using a Rigaku ZSK Primus II X-ray fluorescence analyzer. Total and organic carbon content were measured on aliquots from each horizon using an element analyzer (EA) before and after *in situ* decarbonation, respectively. Inorganic carbon content was calculated as the difference between the two measurements.

Thin sections of oriented samples from each horizon were prepared by Spectrum Petrographics (http://www.petrography.com) and characterized using a combination of methods from Brewer (1964) and Bullock et al. (1985). Carbonates were analyzed in thin section to identify mineral phases. Nodules and rhizoliths were micro-drilled on paired billets and hand samples after cross-comparison with thin sections. Carbonate powders were analyzed for inorganic carbon ($\delta^{13}C$) and oxygen ($\delta^{18}O$) stable isotope composition at Baylor University using a Thermo-Electron dual-inlet gas-source stable isotope ratio mass spectrometer. The delta notation is used in reporting stable isotope compositions (e.g., $\delta^{18}O = [(R_{sample} / R_{standard}) - 1] \times 1000$), where R is the ratio of the heavy to light

isotope (e.g., $^{18}O/^{16}O$). All isotope values are reported relative to the Vienna Pee Dee Belemnite (VPDB) standard with analytical precision within 0.03‰ and 0.1‰ for $\delta^{13}C$ and $\delta^{18}O$, respectively.

Clay mineralogy of parent material and weathered soil horizons was analyzed using oriented clay slides on a Siemens D5000 X-ray diffractometer that uses Cu Kα radiation and operates at 40 Kv and 30 mA. The clay-sized fraction (< 2 μm equivalent diameter) was separated via centrifugation following the methods of Poppe et al. (2001) and oriented clay slides were prepared following the methods of Moore and Reynolds (1997). To differentiate possible commonly-occurring clay minerals, four treatments were performed on clay slides (Moore and Reynolds, 1997): 1) samples were Mg^{2+}-saturated using a Mg salt solution, 2) Mg^{2+}-saturated samples were glycolated overnight in an airtight chamber, 3) duplicate samples were K^{+}-saturated using KCl, and 4) a subset of K^{+}-saturated samples were heated for at least 2 hours at 550°C. All clay samples were analyzed from 2–30° 2Θ with a step size of 0.02° 2Θ and dwell time of 1 second. Clay minerals were identified following the methods of Moore and Reynolds (1997).

Constitutive Mass-Balance

Bulk geochemistry of paleosol horizons was compared using mass-balance calculations (Brimhall and Dietrich, 1987; Chadwick et al., 1990; Brimhall et al., 1991), without including bulk density due to the effects of compaction on paleosol samples (Driese et al., 2000; Driese, 2004; Driese et al., 2016). Translocation (τ, or "tau") of elements was calculated relative to parent material, where: $\tau = \{[(C_{j,w}/C_{j,p})]/[(C_{i,w}/C_{i,p})] - 1\} \times 100$, in which the concentrations (C) of elements (j) in weathered horizons (w) are assessed relative to immobile elements (i) in the parent material (p). Profiles of tau values

therefore can be used to show gains (positive values) or losses (negative values) as a result of pedogenic processes or sedimentary additions, assessed as a function of starting parent material composition. The composition of C and BC horizons was averaged to account for minor biases due to grain size-dependent compositional changes and/or incipient weathering of individual C or BC horizons.

Climate and Vegetation Reconstruction

The elemental composition of paleosol B horizon samples was used to estimate mean annual precipitation (MAP) and temperature (MAT) using a suite of pedotransfer functions (Sheldon et al., 2002; Gallagher and Sheldon, 2013) (Table 2.1). The chemical index of alteration minus potassium (CIA-K), which tracks feldspar hydrolysis and base cation leaching (Sheldon et al., 2002) was used to estimate MAP. The salinization index (NaK; Sheldon et al., 2002) and the paleosol weathering index (PWI; Gallagher and Sheldon, 2013), which track thermodynamic controls on silicate dissolution, were used to estimate MAT. The paleosol-paleoclimate model ($PPM_{1.0}$) (Stinchcomb et al., 2016) was also used to co-predict MAP and MAT. $PPM_{1.0}$ uses eleven elemental oxides as input variables (Fe_2O_3, Al_2O_3, SiO_2, TiO_2, ZrO_2, CaO, MgO, K_2O, Na_2O, MnO, and P_2O_5) to simultaneously model both MAP and MAT using a thin-plate spline drawn through sample scores generated by a partial least squares regression analysis of modern soil B horizon samples. $PPM_{1.0}$ calculations were run in SAS statistical software (SAS Institute, Inc., v. 9.2.). Climate results are discussed in terms of climate zones after (Bull, 1991), which include MAP zones of arid (< 250 mm), semiarid (250–500 mm), subhumid (500–1000 mm), and humid (1000–2000 mm), and MAT zones of frigid (0–8°C), mesic (8–15°C), thermic (15–22.5°C), and hyperthermic (> 22°C).

Table 2.1. Paleoclimate proxies

Model	Index	Index Formula	Model Error[a]	Constraints	Reference
Mean annual precipitation					
CIA-K	100 x [Al_2O_3 / (Al_2O_3 + CaO + Na_2O)]	$221.1e^{0.02(x)}$	182 mm	Bt, Bw horizons	Sheldon et al. (2002)
PPM	NA	Thin plate spline[b]	512 mm	Uppermost B horizons	Stinchcomb et al. (2016)
Mean annual temperature					
NaK	(Na_2O+K_2O) / Al_2O_3	-18.52(x) + 17.298	4.4°C	Bt, Bw horizons	Sheldon et al. (2002)
PWI	100 x (4.20Na_2O + 1.66MgO + 5.54K_2O + 2.05CaO)	-2.74 x ln(x) + 21.39	2.1°C	Forested Inceptisols, Alfisols, and Ultisols	Gallagher and Sheldon (2013)
PPM	NA	Thin plate spline[b]	3.98°C	Uppermost B horizons	Stinchcomb et al. (2016)

Note: Elemental inputs for CIA-K, NaK, and PWI are in units of oxide moles; PPM uses wt. % oxide.
[a]Values used are root mean square errors from regression analysis, except for PPM, where errors are root mean square prediction error based on validation modelling.
[b]Modelled in SAS statistical software; see Stinchcomb et al. (2016) for code and methods

We frame our vegetation reconstruction in terms of photosynthetic pathway, which is possible as a result of two broad photosynthetic mechanisms that differentially fractionate atmospheric CO_2, resulting in plant-respired soil CO_2 with differing carbon isotope signatures ($\delta^{13}C$). Modern plants that use the Calvin cycle (C_3 pathway) include most trees, shrubs, and cool-season grasses, and have $\delta^{13}C$ signatures between –20 to –33‰, with a mean of –26.7‰ (O'Leary, 1988; Cerling et al., 1997). Water stress is the primary factor that drives the enrichment of C_3 plant $\delta^{13}C$ signatures above ca. –24 to –25‰ (Ehleringer and Cooper, 1988). The Hatch-Slack (C_4) pathway, which is utilized mostly by modern tropical and warm-season grasses and sedges, is a series of anatomical and biochemical adaptations that allows for closure of stomata without photorespiration (Sage, 2004). Modern C_4 plants have $\delta^{13}C$ values between –9 to –11‰, with a mean value of –12.5‰ (O'Leary, 1988; Cerling et al., 1997). Carbon isotope values of

vegetation are recorded in the isotopic composition of pedogenic carbonates that form in equilibrium with plant-respired soil CO_2 at depth in soils of moderate to high productivity (Cerling et al., 1989).

Endmember $\delta^{13}C$ compositions for C_3, water-stressed C_3 (wsC_3), and C_4 vegetation were modeled using nominal fractionation factors for each photosynthetic pathway/plant type and corrected for an average atmospheric CO_2 composition of –5.8‰ from benthic foraminifera for the interval 17.07–17.5 Ma (Tipple et al., 2010). Fractionation factors between plants and CO_2 ($\varepsilon_{plant\text{-}CO2}$) reported by Passey et al. (2002) were used, where $\varepsilon_{C3\text{-}CO2} = –19.6‰$, $\varepsilon_{wsC3\text{-}CO2} = –16.7‰$, and $\varepsilon_{C4\text{-}CO2} = –4.7‰$. A net fractionation of +15‰ between plant-respired soil CO_2 and pedogenic carbonate (Fox et al., 2012, after Cerling and Quade, 1993) yielded endmember compositions of –10.4‰, –7.5‰, and +4.5‰ for carbonates forming under C_3, wsC_3, and C_4 vegetation cover, respectively.

Results

Stratigraphy and Sedimentology

NG15 is bounded by trough cross-stratified fluvial channel sandstones (NG14 and NG16). Across ca. 150 m of lateral outcrop, NG15 varies from thinly-bedded, tan fluvial sandstones to red, calcareous sandy siltstones. The NG15-A and B profiles were described where NG15 occurs as sandy siltstone. A total of five superposed paleosols were identified, most of which were underlain by an alluvial parent material (C or BC) horizon (Fig. 2.3). The parent material horizons were more coarse-grained than overlying subsurface horizons, and in some cases retained primary horizontal stratification.

Bedding contacts at the base of parent material horizons are inclined from NG15-A to NG15-B with upwards of 10 cm relief.

Paleosol Descriptions

Detailed descriptions of paleosol macro- and micromorphology are reported in Table A5, with key observations presented in Fig. 2.3. Horizonation is largely similar between profiles NG15-A and B. The uppermost paleosol is truncated from above and grades laterally from a C1-C2 to a Bw-BC horizon sequence between the profiles, respectively. The second paleosol consists of a Btk-BC horizon sequence with lenses of sand and reworked, hard, grey carbonate nodules variably coated in MnO_2 or Fe_2O_3. The Btk horizon has well-developed prismatic ped structure, clay-filled root traces, clay coatings on peds, and vertically-oriented hairline root traces (Fig. 2.4). With the exception of a thin, truncated Bk horizon that underlies the second paleosol in NG15-A, the rest of the succession consists of alternating couplets of Bw-C horizons, each of which are bounded by erosional contacts. The Bw horizons in the lower portion of the profile have root traces that tend to be < 2 mm wide and occur as drab haloes, calcareous rhizoliths, or clay-filled pores.

Pedality—a measure of ped structure development—and reaction to HCl were characterized for profile NG15-B using USDA-NRCS methods (Fig. 2.3) (Schoeneberger, 2002). The B horizons tend to have more well-developed pedality than parent material horizons. Effervescence was very strong in both B horizons and parent material horizons.

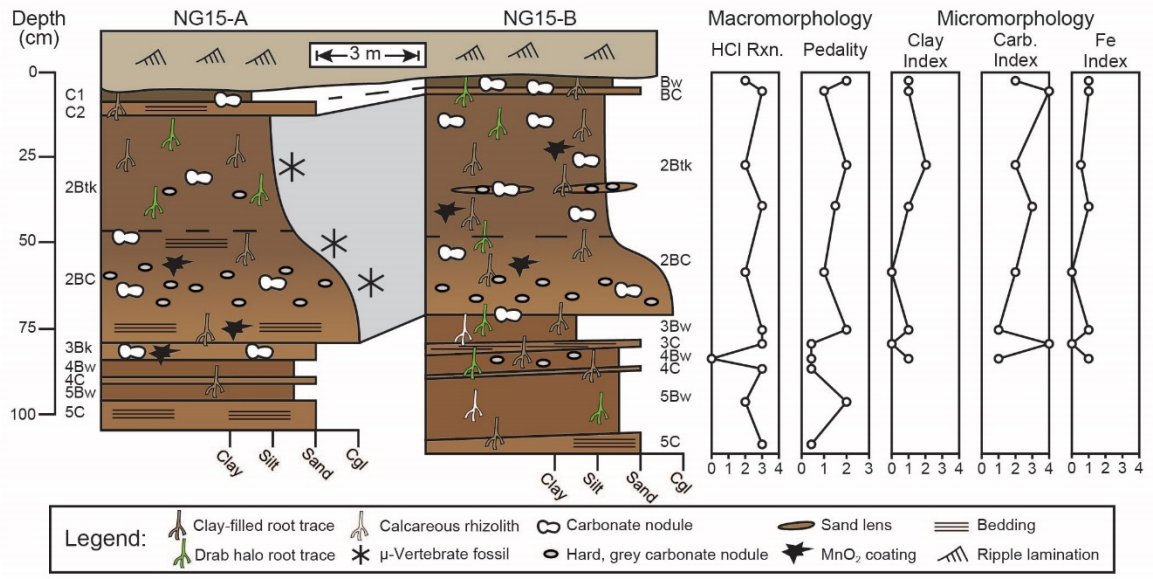

Figure 2.3. Profiles through Ngira unit 15 (NG15). Macro- and micromorphologic descriptions are for profile NG15-B. Numbers before paleosol horizonation indicate separate, superposed paleosols. Effervescence reaction classes (HCl Rxn.) are reported from field tests, with values corresponding to 0) no reaction, 1) very slight, 2) slight, 3) strong, and 4) violent effervescence (after Schoeneberger, 2002). Pedality classes correspond to 0) massive, 1) weakly formed, 2) moderately formed, and 3) strongly formed peds (after Schoeneberger, 2002). Clay, carbonate, and Fe indices are based on qualitative assessment of thin sections with numbers corresponding to features being 0) absent, 1) few, 2) common, 3) abundant, or 4) omnipresent.

Micromorphology

Thin sections from all horizons of the uppermost 4 paleosols in NG15-B were studied for a variety of pedogenic and sedimentary properties (Fig. 2.5). Surveys of clay, carbonate, and Fe features were converted to qualitative indices with values corresponding to features being 0) absent, 1) few, 2) common, 3) abundant, or 4) omnipresent (Fig. 2.3). Pedogenic clay fabric includes grain coatings (granostriated), pore linings (porostriated), and matrix impregnations (argillans). The clay index closely tracks pedality and is highest in B horizons, particularly the 2Btk horizon.

Carbonates exhibit a range of morphologies in profile NG15-B. Pedogenic micrite is the dominant phase in the 2Btk horizon, though minor amounts of sparite coat

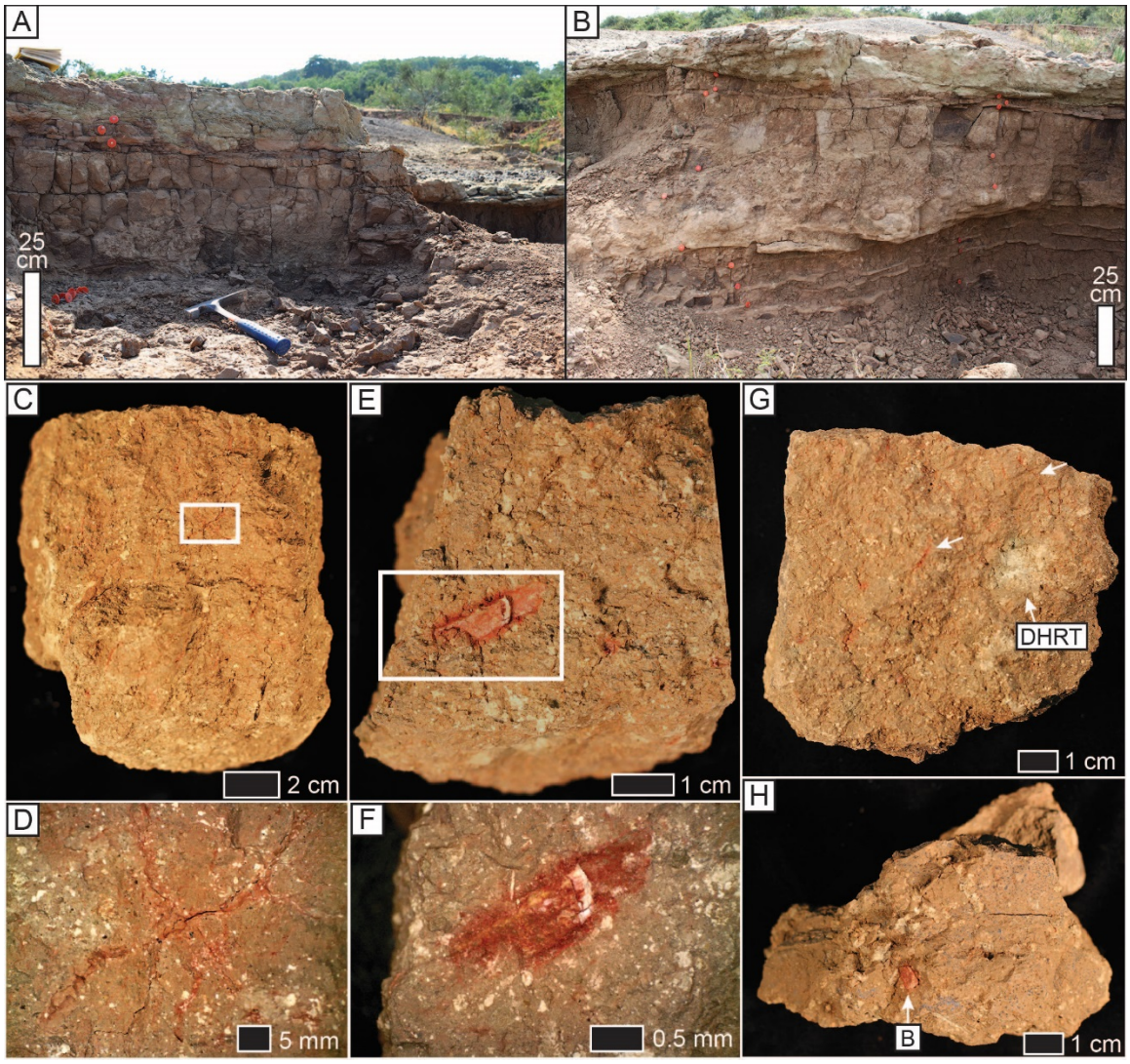

Figure 2.4. Field photographs of profiles of A) NG15-A and B) NG15-B. Note prismatic ped structure in 2Btk horizon. C) Prismatic ped from 2Btk horizon (vertically oriented). Thin, red lines are root traces lined with Fe and clay; white speckles are pedogenic carbonates. D) Close-up of thin root traces from white box in (C). Photo taken with reflected light and a polarizing filter. E) Angular blocky compound ped removed from a prismatic ped in the 2Btk horizon. Photo is the base of the ped, with Fe-coated microvertebrate fossil. F) Close-up of microvertebrate bone from E. Note Fe coating and white pedogenic carbonate. Faint, thin root traces are also present. Photo taken with reflected light and a polarizing filter. G) Angular blocky ped from 2Btk horizon. White arrows indicate fine root traces; DHRT = drab halo root trace. Ped is vertically oriented. H) Base of an irregular angular blocky ped (3Bw horizon), with Fe-stained bone fragment indicated. Note white calcareous rhizoliths, seen in cross section from this view. Photo in box A is used with permission from T. Wenzel.

septarian shrinkage cracks in some cases. Hard, grey carbonate nodules tend to be micritic with minor quantities of sparite in septarian cracks. Diagenetic calcite spar is pervasive in parent material horizons and cross-cuts pedogenic features, such as fecal pellets and clay fabric. Sparite crystals are nucleated on detrital silicate grains and pedogenic features, with growth axes radiating displacively into the paleosol matrix. The carbonate index includes both pedogenic and diagenetic phases, and therefore tracks increases in pedogenic carbonate content in the Btk horizon, as well as diagenetic sparite that occurs in C horizons.

Fe features primarily occur as concretions in B horizons. Fe concretions are nucleated on weathered detrital grains and microvertebrate bone chips, which typically also have clay coatings (Fig. 2.5L-M). The Fe index is highest in B horizons and closely tracks the clay index and pedality.

Microcharcoal (10–500 μm wide) was observed in most thin sections (Fig. 2.5B-C, Fig. 2.5H-I). Grains of microcharcoal were differentiated from detrital silicates and heavy minerals by their opacity under plane- and cross-polarized light, tattered and irregular edges, and lack of cleavage planes. The concentration of microcharcoal grains was not estimated because, in many instances, grains occurred in a large range of sizes, likely as a result of fragmentation.

Elemental Geochemistry

Elemental geochemistry, loss-on-ignition (LOI), and measured organic and inorganic carbon content for the NG15-B profile are reported in Tables A.6-A.9. Untreated samples were compared with samples that were decarbonated before elemental analysis (Fig. 2.6).

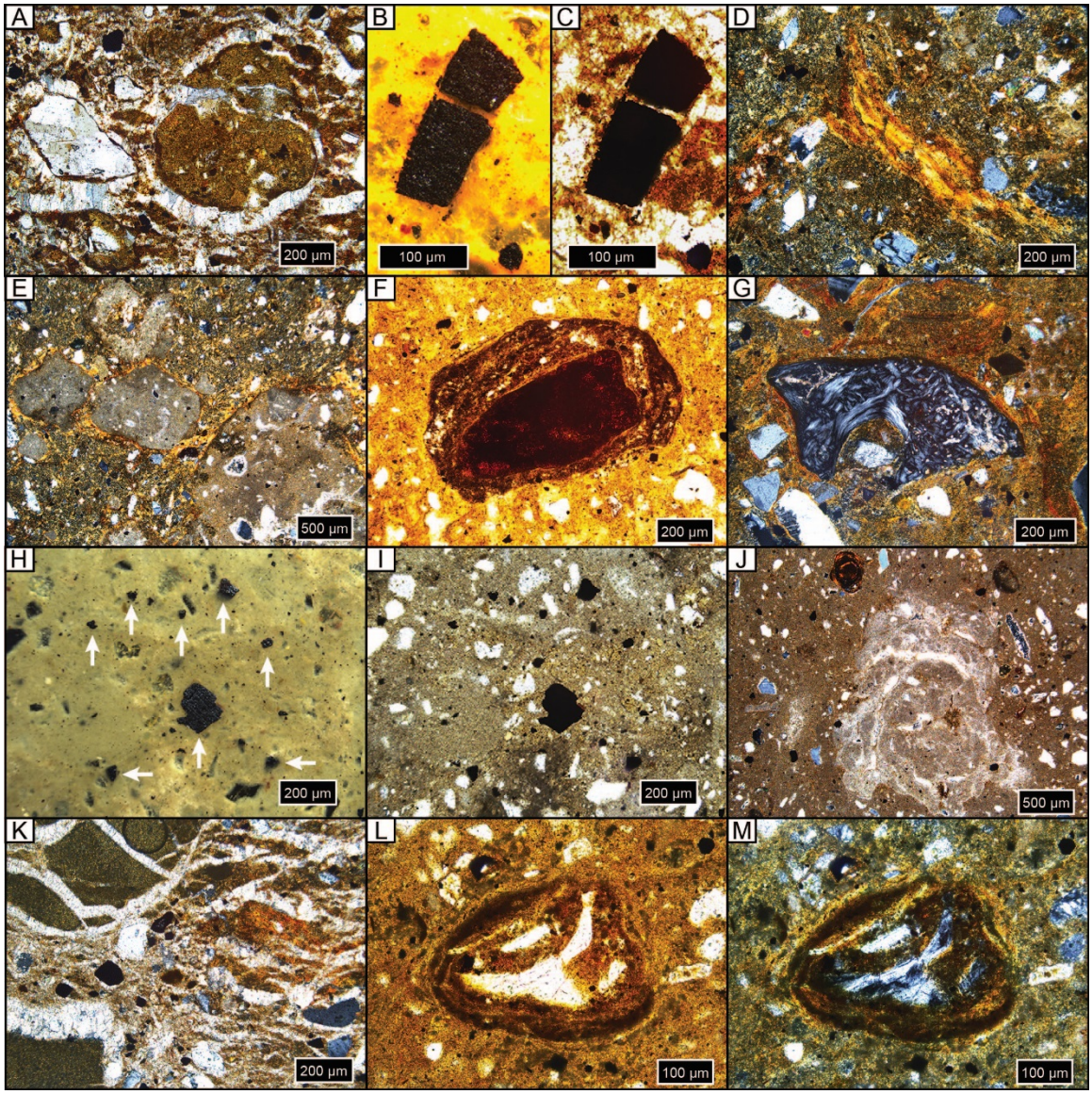

Figure 2.5. Photomicrographs of representative features. All samples are upright and in cross-polarized light unless noted. A) Diagenetic sparite overgrowths on detrital quartz grain, on and in a micritic carbonate nodule, and throughout matrix; NG15-B, BC. B-C) Microcharcoal grain in reflected light (B) and plane-polarized light (ppl) (C); NG15-B, BC. D) Argillan and granostriated clay fabric on quartz and weathered orthoclase detrital grains; NG15-B, 2Btk. E) Micritic carbonate nodules with sparite filling septarian cracks with pedogenic clay bridges (granostriated fabric); NG15-B, 2Btk. F) Fe concretion nucleated on weathered detrital grain; note clay coatings within and on concretion, and clay-rich matrix; ppl, NG15-A, 2Btk. G) Granostriated clay fabric on bone chip and detrital grains; NG15-A, 2Btk. H-I) Microcharcoal grains in reflected light (H, white arrows) and ppl (I); NG15-B, 2BC. J) Microspar carbonate concretion with sparite filling septarian cracks. Thin clay coats line septarian walls. Note Fe concretion and sparite overgrowths on detrital grains; NG15-A, 3Bw. K) Displacive sparite around and within clay clasts (left) and orange pedogenic clay (right), on detrital grains, and through matrix; NG15-B, 3C. K-L) Bone chip encased in Fe/clay concretion, ppl (L) and xpl (M); NG15-B, 4Bw.

Effects of HCl Treatments. The concentrations of CaO and inorganic carbon from NG15-B are well correlated with loss on ignition (Fig. 2.6). Organic carbon is uncorrelated with loss on ignition. Because clay mineralogy is dominated by illite, which holds little structural water (Moore and Reynolds, 1997), and organic carbon concentrations are low (ca. 0.03 wt.%), the majority of LOI is attributed to calcite.

All major elemental oxides (Na_2O, MgO, K_2O, Fe_2O_3, SiO_2, P_2O_5, MnO, Al_2O_3, and Ti_2O) show significant ($p < 0.05$) correlations with CaO in untreated samples (Table A.10). Because many of the oxides are not associated with carbonate minerals, the correlations are interpreted to be a result of CaO diluting the contributions of other elementals to total measured concentrations. In contrast, only SiO_2, P_2O_5, MnO, and Al_2O_3 are correlated with CaO in decarbonated samples, and none of the weatherable bases (MgO, Na_2O, K_2O) are correlated with CaO. Most elements, including CaO, show little down-profile variation in decarbonated samples.

The effect of weight percent change induced by removal of carbonate-bound calcium scales linearly with the elemental concentration of each oxide, such that elements with higher concentrations in decarbonated samples receive a proportionately larger share of the relative measured weight occupied by CaO in untreated samples (Fig. 2.6). Regression diagnostics were analyzed using the “plot” function in R (R Core Team, 2016). Two samples with high initial CaO (28.0 and 30.5 wt. % before HCl treatment) were found to be high-leverage points in the linear regression, both of which had a Cook’s distance of ca. 1 or more (Cook and Weisberg, 1982). For these two samples, decarbonation resulted in disproportionately large increases in SiO_2 (samples with mass

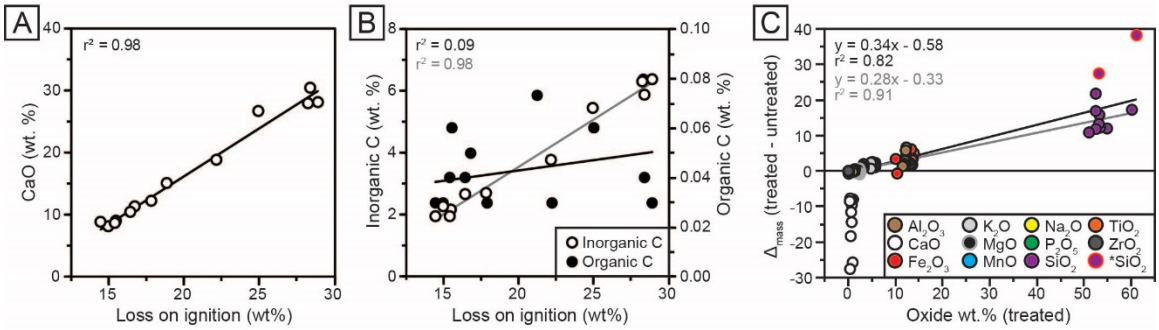

Figure 2.6. A) CaO in untreated samples is strongly correlated with loss on ignition (LOI). B) Inorganic C is strongly correlated with LOI (grey regression line); organic C is very low in abundance and not correlated with LOI (black regression line). C) Effect of treatment on oxide abundances. The y-axis is the mass change, calculated as decarbonated sample mass minus untreated mass, plotted against mass of treated (decarbonated) samples. Note that mass change scales with oxide abundance for all constituents except CaO. *SiO2: Two outlier values with high initial CaO and high SiO2 mass change, which improve regression statistics when omitted. Black regression was calculated for all samples. Grey regression was calculated omitting two SiO2 outliers.

change > 25 in Fig. 2.6C). When these two samples were omitted from simple linear regression in Fig. 2.6C, the correlation coefficient between treatment effect (oxide mass gain after decarbonation) and decarbonated oxide mass increased from 0.82 to 0.91. No other samples were found to be high-leverage points in regression analyses. The removal of CaO via decarbonation caused substantial increases in CIA-K and PWI index values (Fig. 2.7A-B). Because Na_2O and K_2O are minimally affected by the treatment, NaK index values do not change significantly after decarbonation (Fig. 2.7C).

Mass-Balance Geochemistry. The three oxides commonly used as immobile index constituents in mass-balance calculations are Al_2O_3, TiO_2, and ZrO_2. The concentrations of these three oxides in untreated samples vary greatly down-profile, but showed little variation in decarbonated samples. Al_2O_3 was selected as the immobile element for mass-balance calculations because it has the highest concentration of the three candidate oxides.

Results of tau calculations are presented in Figure 2.7, wherein untreated and decarbonated samples are overlain on mass-balance plots for comparison. TiO_2 and SiO_2 concentrations do not vary relative to Al_2O_3 in both untreated and decarbonated samples. Fe_2O_3, however, shows increases in decarbonated samples from B horizons, a trend that was not observable in untreated samples and mirrors the micromorphologic Fe index (Fig. 2.3). CaO shows large losses in B horizons relative to parent material in untreated samples (Fig. 2.7E). With the exception of gains in the uppermost horizon, CaO concentrations in decarbonated samples vary within ca. 50% of parent material composition. MgO concentrations vary within ca. 25% of parent material for both untreated and decarbonated samples (Fig. 2.7E). K_2O and Na_2O show inverse trends that are unaffected by the acid treatment (Fig. 2.7F).

Clay Mineralogy

Samples from the five uppermost horizons of NG15-B profile yielded similar X-ray diffraction results (Fig. 2.8). Primary peaks on each diffractogram of K^+-saturated samples occur at 10.15 Å, 5.02 Å, and 3.34 Å, which are associated with illite/mica 001, 002, and 003 peaks, respectively. Quartz can also contribute to the peak at 3.34 Å, but because a secondary peak at 4.26 Å is absent, quartz is either absent in the clay-sized fraction or contributing very little to the illite 003 peak. Peaks associated with smectite (17.5 Å) and kaolinite (7.18 Å and 5.38 Å) were not observed. The lack of change with Mg^{2+} saturation, glycolation, or heat treatments further supports an interpretation of exclusively illitic clay mineralogy. The calcite peak corresponding to a d-spacing of 3.03 Å is present in all samples, and is sharpest in the Btk horizon. Peaks occurring at 4.51 Å and 3.52 Å may indicate minor quantities of detrital palygorskite and kaolinite,

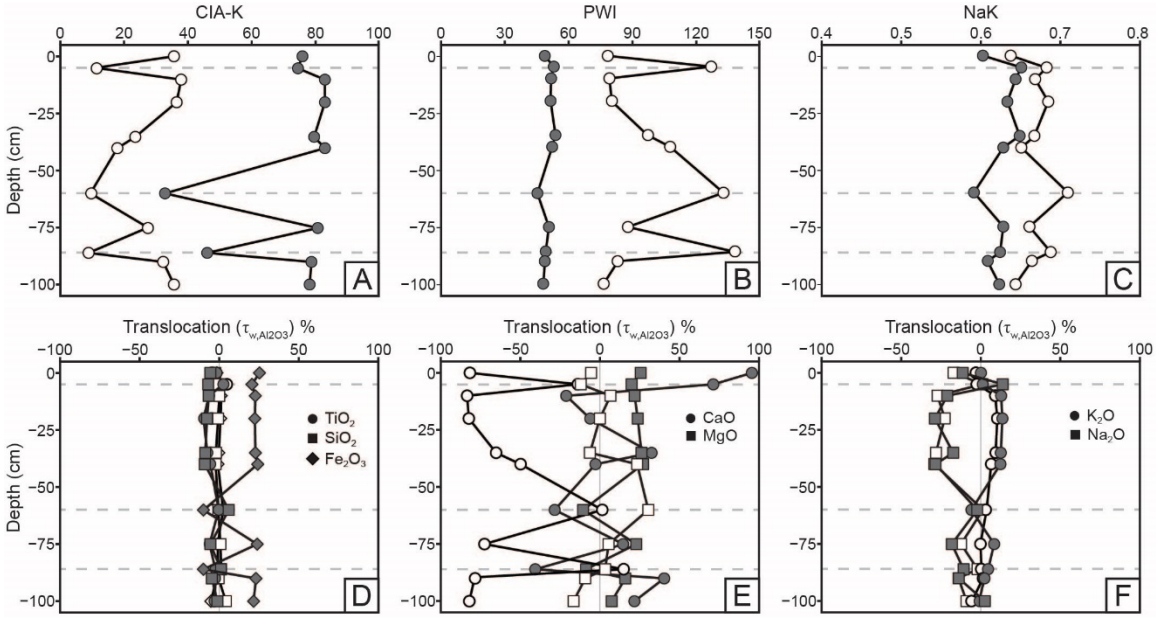

Figure 2.7. Profiles of weathering indices and constitutive mass-balance results. See Table 2.1 for weathering index formulae. A) Chemical index of alteration minus potassium (CIA-K) values increase with decarbonation as a result of CaO removal and Al2O3 relative mass increase. B) Paleosol weathering index (PWI) values decrease with decarbonation; note that lower PWI values correspond to more highly weathered, base-poor samples. C) Salinization index (NaK) values are generally inversely correlated before and after treatment due to the relative increase in Al2O3 with removal of CaO.

respectively (e.g., Myers et al., 2011), though no secondary peaks associated with either mineral is present.

Paleoclimate

Two approaches were used to estimate MAP and MAT values: pedotransfer functions using weathering index proxies for MAP or MAT, and a multivariate spline model that uses 11 elemental oxides as input values to co-predict MAP and MAT (Fig. 2.9). The CIA-K proxy for MAP yields arid to semiarid values (< 500 mm) for untreated samples and mostly subhumid values (500–1000 mm) for decarbonated samples. MAP values calculated using $PPM_{1.0}$ range from arid to humid for untreated samples, and, interestingly, range from arid to subhumid for treated samples—substantially lower than

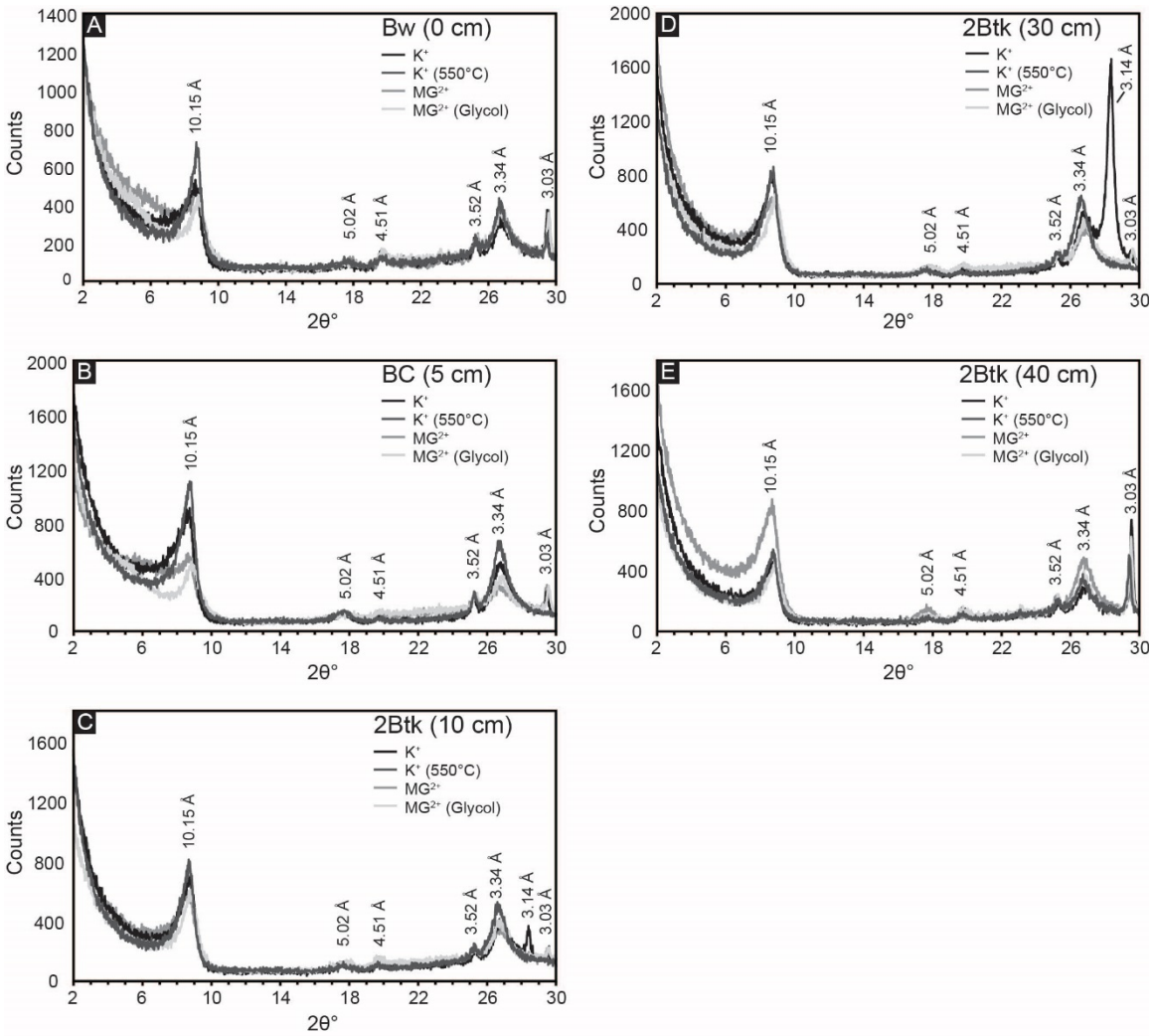

Figure 2.8. X-ray diffractograms of the < 2μm fraction from the first five horizons in NG15-B: A) Bw, B) BC, and C-E) three samples from the 2Btk horizon. Four treatments were applied to all samples: K-saturation, heating to 550°C of K-saturated samples, Mg-saturation, and ethylene glycolation of Mg-saturated samples. Illite is identified by the presence of peaks at 10.15 Å, 5.02 Å, and 3.34 Å. Peaks associated with smectite (17.5 Å) and kaolinite (7.18 Å and 5.38 Å) were not observed, and the lack of change with glycolation or heat treatments further supports an interpretation of exclusively illitic clay mineralogy.

CIA-K predicted MAP. Decarbonation resulted in no detectable change in MAT values predicted by NaK and PWI, which were within the frigid (< 8°C) and mesic zones (8–15°C), respectively. The $PPM_{1.0}$ model yielded mesic to thermic MAT values (ca. 8–18°C) for untreated samples and frigid to mesic values (ca. 5–14°C) for treated samples.

Stable Isotopes and Pedogenic Carbonates

Pedogenic carbonate $\delta^{13}C$ and $\delta^{18}O$ results are presented in Fig. 2.10; raw values are reported in Table A.11. Values for $\delta^{13}C$ span approximately 9‰, ranging from -7.3 ± 0.1 to -1.9 ± 0.2‰ VPDB, and the majority of samples are more positive than the calculated endmember of water-stressed C_3 vegetation. Previously analyzed carbonate nodules from units 19 and 20 by Driese et al. (2016) fall within the range of samples presented in this study, with the exception of a single nodule close to the C_3 endmember composition. Samples of lacustrine oncoid carbonate reported by Driese et al. (2016) fall in the middle of the isotope space and mirror the overall negative correlation between $\delta^{13}C$ and $\delta^{18}O$. This suggests that lacustrine carbonates carried an isotope signal that sampled a mixture of local vegetation, similar to Pleistocene riverine tufa from Karungu and Rusinga Island (Beverly et al., 2015). Mean $\delta^{18}O$ values reported in this study range from –4.6‰ to –8.0‰, which are similar to pedogenic carbonate values ranging between ca. –5‰ to –8‰ reported from middle Miocene sites at Fort Ternan and West Turkana in Kenya (Cerling, 1992), and thus likely did not form from highly evaporitic waters.

Measured $\delta^{13}C$ values show limited correlation with carbonate morphology. Micritic, hairline rhizoliths from Bw horizons in the NG15-B profile have the highest $\delta^{13}C$ values (up to –1.9‰). Mixed samples containing both rhizoliths and nodules are variable across the sample space. The composition of hard, grey nodules interpreted to be detrital is not unique; those occurring the 4Bw horizon have relatively high $\delta^{13}C$ and low $\delta^{18}O$ values, whereas those found in the 2Btk horizon have lower $\delta^{13}C$ and higher $\delta^{18}O$ values.

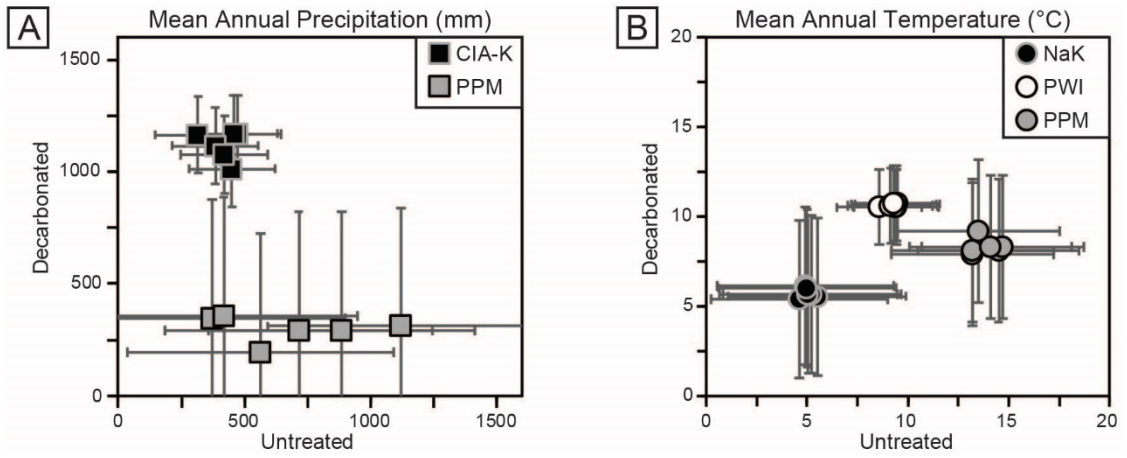

Figure 2.9. Cross-plots of climate estimations for decarbonated and untreated samples. See Table 2.1 for details of each proxy. A) Mean annual precipitation (MAP) estimates using CIA-K and PPM1.0 show disparate results. MAP estimates using CIA-K are likely underestimated in untreated samples and overestimated in decarbonated samples, suggesting a dry subhumid climate (800–1000 mm), within error of PPM1.0 estimates. B) Mean annual temperature (MAT) estimates using NaK, PWI, and PPM1.0. Decarbonation had little effect on NaK and PWI estimates, but reduced PPM1.0 output values. All estimates are interpreted to be too low for the geologic setting and sampled flora and fauna.

Using the calculated C_3 and C_4 endmembers of carbonate compositions, 21–57% of the standing biomass associated with NG15 was C_4 vegetation. If a water-stressed C_3 endmember is used, 2–47% C_4 biomass is required to account for the observed $\delta^{13}C$ values, which on the upper end at least is a considerable and possibly surprising amount of C_4 biomass for an interval of this age.

Microfossil Assemblage Results

Faunal composition of the excavated NG15 site is given in Table 2.2. NISP for the excavation grid at NG15 was 415, including surface collections within the grid boundaries. Mammals are the dominant taxon in the excavated grid, with 81.1% of the total abundance (83.6% when including the indeterminate Mammalia). Aquatic taxa are present, but not very common and include crocodiles (1.7%), turtles (1.2%), and fish

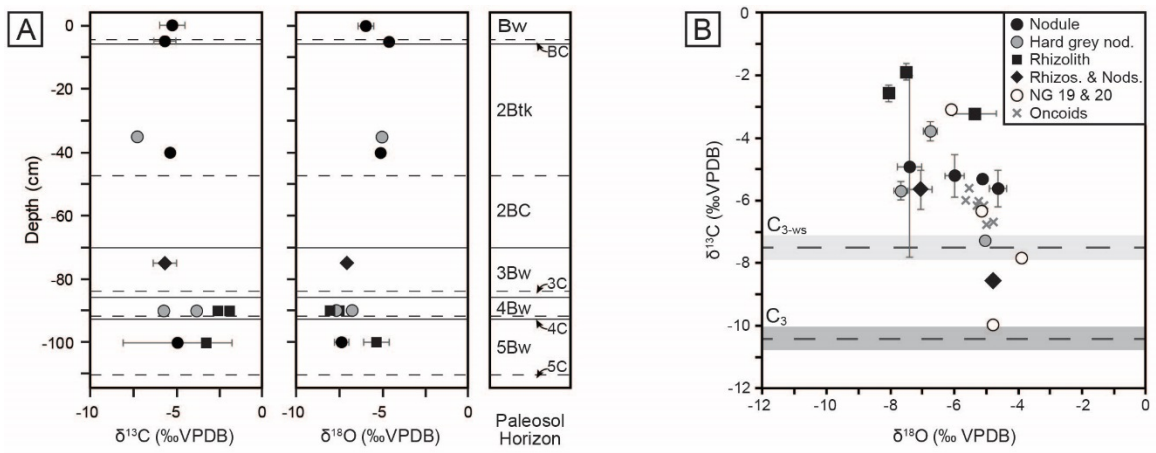

Figure 2.10. Stable isotopic compositions of pedogenic carbonates from Ngira. A) Profiles in NG15-B of pedogenic carbonates, coded by morphology and phase (see B for key). Each sample is the mean of triplicate analysis; 1 σ error bars about the mean are shown when error is greater than symbol size. B) Cross-plot of δ13C vs. δ18O values, with calculated endmember compositions for C3 and water-stressed C3 (C3-ws) vegetation. The C4 endmember is +4.5‰. Data for units NG19 and NG20, as well as lacustrine oncoid carbonates, are also plotted (from Driese et al., 2016).

(1.2%). In contrast, crocodiles and turtles collectively represent almost a third of the total NISP recovered through surface collections at Ngira as a whole.

Only 152 of the 347 mammal specimens are sufficiently well-preserved to be identified at the genus level (Table 2.3). By comparison, the surface collections made at Ngira include over 3,000 fossils, but only 482 belong to small mammals (i.e., body size of the rodent *Megapedetes pentadactylus* or less) identifiable to the genus level. The taxonomic composition of the NG15 excavation includes 10 genera, and surface collections from throughout Ngira yielded 18 genera of comparable size ranges. Both samples show seven genera in common, whereas three genera are unique to the NG15 excavation sample and 11 to the surface collections (Table 2.3). Accordingly, the Jaccard similarity coefficient and the Sørensen–Dice index are very low (33.3% and 50%

Table 2.2. Faunal composition of the excavated NG15 site.

Taxon	NG15 Excavation	
	NISP	%
Artiodactyla	13	3.8%
Carnivora	1	0.3%
Hyracoidea	1	0.3%
Lagomorpha	23	**6.6%**
Lipotyphla	3	0.9%
Macroscelidea	21	**6.1%**
Rodentia	219	**63.1%**
Crocodilia	6	1.7%
Gastropoda	15	4.3%
Osteichthyes	4	1.2%
Potamoidea	14	4.0%
Squamata	23	**6.6%**
Testudines	4	1.2%
Identified NISP	347	83.6%
Total Mammalia	281	81.1%
Indet. Mammalia	66	15.9%
Indet. Vertebrata	2	0.5%
Total NISP	415	

Note: Only specimens recovered during the excavations and the surface sweep of the grid are shown. The most abundant taxa are highlighted. NISP = Number of Individual Specimen; % = relative abundance.

respectively) (see Lyman, 2008), which indicate that the overall surface collection is quite different from the NG15 excavation in their taxonomic composition.

The small mammal community at Ngira is dominated by artiodactyls (especially the genus *Dorcatherium*) in the overall surface collection sample. In contrast, the NG15 excavation fauna is dominated by rodents, especially the genus *Paraphiomys*. Lagomorphs are equally well represented in both samples, whereas macroscelids (especially the genus *Myohyrax*) are more abundant in the surface collection sample. The NISP of each genus in common between surface collected and excavated samples at NG15 differ significantly in terms of taxonomic abundance (chi-square = 220.27; $p < 0.001$) and are not correlated (Spearman's rho = 0.36; $p > 0.10$), which suggests that the

Table 2.3. Composition of the small mammal fauna from Ngira.

Taxon	NG15 Excavation		Ngira Surface Collections	
	NISP	%	NISP	%
RODENTIA	95	54.9%	61	12.7%
Bathyergoides	0	0.0%	1	0.2%
Diamantomys	0	0.0%	2	0.4%
Epiphiomys	0	0.0%	2	0.4%
Kenyamys	2	1.2%	0	0.0%
Paraphiomys *	89	**51.4%**	53	**11.0%**
Pedetidae *	4	2.3%	3	0.7%
LAGOMORPHA	23	13.3%	33	7.2%
Kenyalagomys *	23	**13.3%**	33	7.2%
MACROSCELIDEA	20	11.5%	128	27.8%
Miorhynchocyon	3	1.7%	0	0.0%
Myohyrax *	17	**9.8%**	128	**27.8%**
LIPOTYPHLA	2	1.2%	4	0.9%
Amphechinus	0	0.0%	3	0.7%
Galerix	1	0.6%	0	0.0%
Gymnurechinus *	1	0.6%	1	0.2%
ARTIODACTYLA	12	7.0%	244	52.9%
Diamantohyus *	1	0.6%	30	6.5%
Dorcatherium *	11	6.4%	209	**45.3%**
Walangania	0	0.0%	5	1.1%
TUBULIDENTATA	0	0.0%	5	1.1%
Myorycteropus	0	0.0%	5	1.1%
CARNIVORA & HYAENODONTA	0	0.0%	2	0.4%
Anasinopa	0	0.0%	1	0.2%
Stenoplesictis	0	0.0%	1	0.2%
PRIMATE	0	0.0%	5	1.1%
Dendropithecus	0	0.0%	3	0.7%
Ekembo	0	0.0%	1	0.2%
Nyanzapithecus	0	0.0%	1	0.2%
Total NISP	152		482	

Note: Table includes specimens recovered from the NG15 excavations and from surface collections (including REACHE surveys in 2010, 2012, 2013, 2015 and historical collections housed at the NMK). Included are all specimens identified to the genus level from taxa smaller or equal in size with Megapedetes pentadactylus. Pedetidae regroups the genera Megapedetes and Rusingapedetes. For each collection, the three most abundant taxa are highlighted. NISP = Number of Individual Specimen; % = relative abundance; * = genera in common in both samples.

fauna recovered by the NG15 excavation may represent a separate ecosystem, or at least—taking into account time averaging for the surface collections—a specific ecosystem within an environmental mosaic that varied spatially and temporally at Ngira. Notably absent from NG15 are carnivorous mammals and primates, which are also rare in the surface and historical collections from Ngira.

Notable taxonomic differences were also observed within the NG15 profile (Table 2.4). The depth interval from 5–50 cm, which includes the C1, C2 and 2Btk horizons, is dominated by *Paraphiomys* and lacks remains of *Dorcatherium* and Pedetidae. The depth interval from 50–80 cm, yields a moderate abundance of *Dorcatherium* and Pedetidae, but lacks the rodent *Kenyamys*. Although the taxonomic abundance of each depth interval is not significantly different (chi-square = 9.43; $p > 0.32$), the taxonomic composition does differ between the upper and lower portions of the profile (Jaccard similarity coefficient of 33.3%; Sørensen–Dice index of 50%).

Discussion

Two profiles through stacked paleosols in unit 15 at Ngira preserve a unique assemblage of physical, biotic, and climatic elements of the Critical Zone in western Kenya during the early Miocene. The following discussion frames field and laboratory observations into interpretations of Critical Zone components, and subsequently ties inter-related processes together.

Lithosphere

The stratigraphic interval of NG15 transitions laterally from small fluvial channels (Driese et al., 2016) to pedogenically modified floodplain siltstones.

Table 2.4. Faunal composition of the excavated NG15 site by depth interval, omitting surface collections.

Taxon	NG15 Excavation			
	5 to 50 cm (2Btk)		50 to 80 cm (2BC)	
	NISP	%	NISP	%
Kenyamys	1	3.2%	0	0.0%
Paraphiomys	22	**71.0%**	54	**58.1%**
Pedetidae	0	0.0%	4	4.3%
Kenyalagomys	5	**16.1%**	15	**16.1%**
Myohyrax	3	**9.7%**	7	7.5%
Miorhynchocyon	0	0.0%	1	1.1%
Galerix	0	0.0%	1	1.1%
Diamantohyus	0	0.0%	1	1.1%
Dorcatherium	0	0.0%	10	**10.8%**
Total NISP	31		93	

Note: Included are all specimens identified to the genus level. For each interval, the three most abundant taxa are highlighted. NISP = Number of Individual Specimen; % = relative abundance.

Microtopography observed across the ca. 3 m described in the current study includes dipping sedimentary and paleosol horizon contacts that are overlain by coarser sediment, reworked carbonate nodules, and microvertebrate skeletal elements. We interpret these features to be the result of cut-and-fill episodes that were subsequently overprinted by pedogenic alteration.

The mineral assemblage reflects granitic basement sources in the surrounding uplands (Smith and Mosley, 1993), and lacks evidence of drainage connection to the Kisingiri volcanic complex to the northwest. The detrital grains observed in thin section consist of dominantly poly- and monocrystalline quartz, with accessory orthoclase, microcline, and plagioclase feldspars. This mineral assemblage is likely derived from a granitic source rather than the mafic-alkaline volcanic source at Kisingiri, due primarily to the lack of tuffaceous material, volcanic rock fragments, and paucity of mafic minerals observed in thin section. Amphiboles and pyroxenes are rare in NG15 thin sections and

are highly weathered. The Fe released by decomposition of these mafic minerals was conserved as concretions in B horizons.

The clay mineral assemblage in NG15 is composed of illite, and volcanic grains are notably absent. Illite is most likely a detrital rather than diagenetic mineral for two reasons. First, unaltered smectite was observed in the lowest unit at Ngira (NG01) and contains no illite (Driese et al., 2016). If the illite observed in NG15 were an alteration product of smectite, one would expect that NG01 would also have been illitized. The unconformity above NG01 coincides with a change in sediment composition and geomorphology, which accounts for the lack of detrital illite in NG01. Second, mass-balance calculations after removal of calcite from NG15 revealed that relatively little elemental variation was present between paleosol horizons. Significant production of pedogenic clay in B horizons would have been evident as increases in Al_2O_3 relative to SiO_2 (Retallack, 2008), which was not observed. Therefore, we interpret micromorphologic clay fabric and macroscopic clay coatings to be reworking of detrital clay.

Forbes et al. (2004) previously described the stratigraphy and selected paleosols at Ngira. Their KU-3 paleosol is almost certainly the same interval as NG15, as their description includes clay-lined columnar peds in a Bt horizon underlain by thin couplets of siltstone and sandstone (see Fig. 2.3 in Forbes et al., 2004). The ped structure in the Btk horizon is actually prismatic, forming as a result of clay translocation and stabilization by herbaceous roots, rather than columnar peds, which form as a result of clay flocculation in sodic soils (Brady and Weil, 2008). Forbes et al. (2004) calculated constitutive mass-balance for samples equivalent to the Btk horizon of NG15 relative to a

granitic parent material and found losses of 80–90% for SiO_2, Na_2O, and K_2O. This result led to the interpretation that the paleosols formed under subhumid to humid conditions. However, the parent material for the NG15 paleosol was fine-grained alluvium—originally sourced from granitic basement—and had significant additions of CaO associated with diagenetic calcite (Fig. 2.6). Pre-weathering and reworking of alluvium before deposition at NG15 led to the overestimation of mass loss calculated by Forbes et al. (2004). After removing carbonate-associated CaO, we found that only moderate *in situ* weathering occurred and the climate was more likely dry subhumid.

Hydrosphere

The NG15 paleosols show evidence of variable drainage conditions. The 2Btk horizon contains prismatic ped structure, macro- and microscopic illuvial clay coatings, pedogenic carbonate, and oxidized color, all of which form during well-drained conditions (Birkeland, 1999). In contrast, isolated zones of Fe depletion are also present in both hand sample and thin section and are the result of saturated conditions. Hematite concretions are present in all B horizons and require intervals of water saturation to reduce and mobilize Fe from the surrounding soil matrix, and subsequent intervals of well-drained conditions to oxidize and stabilize Fe^{2+} to Fe^{3+} (Vepraskas, 2001). Taken together, these features indicate that the paleosols in NG15 were episodically waterlogged, but the predominance of oxidized features is consistent with well-drained conditions for relatively longer durations.

Atmosphere: Climate State

Mean annual precipitation estimations using CIA-K are bounded by underestimates associated with untreated samples containing artificially high CaO, and overestimates from decarbonated samples containing artificially low CaO due to the removal of small quantities of pedogenic carbonate. The best estimate for paleo-MAP is likely subhumid (500–1000 mm), which falls between the values calculated for untreated (< 500 mm) and decarbonated samples (800–1200 mm). Previous MAP estimates from paleosol B horizons in NG19 and NG20, which occur ~5 m stratigraphically above NG15 and showed no evidence of diagenetic calcite, also yielded subhumid MAP estimates (Driese et al., 2016). Results from the $PPM_{1.0}$ model are variable with high error that encompasses all values calculated using CIA-K, and therefore offer less practical utility than the CIA-K estimates. The presence of illuvial clay and pedogenic carbonate is an indication of seasonally-variable precipitation.

Estimations of MAT using NaK, PWI, and $PPM_{1.0}$ are all clearly too low given the equatorial setting of the locality and presence of taxa that currently inhabit thermic to hyperthermic climate zones (e.g., crocodilians and turtles). Instead we suggest that MAT was probably considerably warmer and similar to fossil leaf estimates from Rusinga Island of 23–35°C (Michel et al., 2014). Paleosol studies frequently find the results from elemental proxies for MAT are below reasonable values, primarily because MAT is much less important in controlling soil weathering compared to other variables, such as MAP (e.g., Stinchcomb et al., 2016).

Biosphere

Flora. Multiple lines of evidence suggest that paleosols in NG15 formed under open canopy conditions with predominantly herbaceous vegetation. Root traces are abundant and occur in multiple morphologies, including calcareous rhizoliths, clay- and Fe-lined root pores, and as drab haloes. Drab halo root traces do not preserve original root dimensions (Retallack, 2008); however, calcareous rhizoliths and clay- and Fe-lined pores likely record primary root diameters. All observed root traces are less than ca. 5 mm, consistent with herbaceous roots.

Further, $\delta^{13}C$ values of pedogenic carbonates are surprisingly high, and cannot be explained by water-stressed C_3 vegetation under the boundary conditions of modern terrestrial vegetation $\delta^{13}C$ values (Kohn, 2010). The weak, negative relationship between $\delta^{13}C$ and $\delta^{18}O$ values ($r = -0.58$) negates the possibility that high $\delta^{13}C$ values (i.e., water stressed vegetation) are associated with evaporative enrichment of soil water in ^{18}O, a circumstance observed in some lacustrine settings (Ufnar et al., 2008). The most parsimonious explanation of highly enriched $\delta^{13}C$ signatures of pedogenic carbonates is the presence of C_4-photosynthesizing biomass. Most of the measured $\delta^{13}C$ values fall within the range of modern wooded grassland (roughly –2.4‰ to –6.9‰), with only three samples within the range of woodland/bushland/shrubland biomes (roughly –6.9‰ to –12‰) (Cerling et al., 2011).

Forbes et al. (2004) reported organic carbon stable isotope analyses for the NG15 paleosol interval (interpreted to be their unit KU-3), with all values between ca. –22‰ to –25‰. Total organic matter measured in the paleosol was between 0.08 to 0.02 wt.%, which is far less than typical soil organic matter contents (e.g., Wynn, 2007). These

organic carbon isotope signatures are within the range for early Miocene C_3 vegetation. However, given the very low organic contents of the paleosols, we contend that the stable isotope signatures of pedogenic carbonates are better indicators of aboveground biomass in this setting.

Modern hydromorphic Vertisols have been shown to precipitate carbonate during a range of hydrologic conditions, from fully saturated to well-drained (Mintz et al., 2011). In such soils, $\delta^{13}C$ values of authigenic carbonate phases tend to be more positive when calcite precipitates during well-drained conditions as a result of actively growing C_4 biomass and higher rates of atmospheric CO_2 diffusion into soil pore space (Cerling et al., 1991). Though NG15 does not contain Vertisols, occasional waterlogging may simulate the poorly drained phase common in Vertisols. The Mintz et al. (2011) model of carbonate precipitation is in line with our interpretation of a C_4 biomass isotopic signature on the $\delta^{13}C$ values measured for NG15: specifically, that the carbonates in NG15 formed during well-drained conditions in equilibrium with fully terrestrial aboveground biomass. If, however, bicarbonate-fixing semi-aquatic vegetation were present at the time of carbonate precipitation, C_4 vegetation would not be necessary to account for the very positive values observed (e.g., Rascio, 2002). To our knowledge, there is no diagnostic method for independently identifying such vegetation from the set of observations available in this study (e.g., root morphology). Thus, we acknowledge the possibility that the observed $\delta^{13}C$ values for pedogenic carbonates in NG15 could be the result of bicarbonate fixation by C_3 vegetation during water-saturated conditions. Given that the NG15 paleosols appear to be predominantly well-drained, with only occasional waterlogging, it is most plausible that the pedogenic carbonates measured in this study

formed during well-drained conditions in equilibrium with a mixture of C_3 and C_4 biomass.

The $\delta^{13}C$ values measured for NG15 are similar to those previously reported by Driese et al. (2016) for paleosols in NG19 and NG20 (Fig. 2.10B). Because NG19 and NG20 were interpreted to be redoximorphic Vertisols, soil forming conditions were generally similar to that of NG15—a fine grained substrate subjected to occasional waterlogging on a low-lying fluvial landscape. These similarities suggest that the open canopy biome interpreted for NG15 was recurrent throughout the stratigraphic section at Ngira, and that C_4 vegetation inhabited a marginal habitat within a narrow range of landscape positions in the early Miocene.

The microcharcoal reported in this study suggests that wildfires occurred in seasonally dry landscapes at or nearby Karungu in the early Miocene, though we note that cellular structure and stomata were not observed in our samples. Seasonal aridity is independently recorded as micromorphologic interlayering of translocated clay and carbonate in pedogenic concretions (Fig. 2.5), with intervals of carbonate precipitation representing seasonal water deficiency. The microcharcoal grains are small enough to have been deposited from eolian or fluvial deposition. However, because most environmental reconstructions for early Miocene sites are for forested or woodland environments (Jacobs et al., 1999), it is more likely that the charcoal originated locally in association with the open canopy land cover at NG15. Fire is one of the key ecological variables that can facilitate the maintenance of open-canopy landscapes, (Bond and Keeley, 2005; Keeley and Rundel, 2005), and may have been an important property of the paleolandscapes preserved in NG15.

Fauna. The dominance of terrestrial fauna, paucity of aquatic taxa, and down-profile variations in faunal composition within NG15-A are consistent with sedimentologic and paleopedologic interpretations. The depth interval of 50-80 cm (2BC horizon) contains a larger NISP and taxonomic diversity than the overlying 45 cm (Table 2.4), suggesting that fluvial reworking mixed microvertebrates from the local area and deposited them with detrital parent material. The depth interval from 5-50 cm is predominantly the 2Btk horizon and either contains a more local faunal signal unique to the position of NG15 on a floodplain, or a depositional fining-upward pattern caused taphonomic filtering toward smaller specimens higher in the profile.

The NG15 fauna differs both in taxonomic composition and abundance compared to the Ngira locality overall, with a predominance of *Paraphiomys* and a relative scarcity of artiodactyls (*Dorcatherium*), primates, and carnivores. Lagomorphs (*Kenyalagomys*) and elephant-shrews form an important proportion of the small mammal fauna at the NG15 site, but the highly specialized *Myohyrax* (Macroscelidea) is less abundant than in the overall Ngira assemblage. The small proportion of microfossils in surface collections can be attributed to multiple factors, including their relatively higher erodibility from outcrop and the inherent bias toward sampling larger fossils in surface collection (Rogers et al., 2017). Microfossil assemblages are therefore particularly important to assess relative taxonomic abundance and species richness as they help to recover otherwise underrepresented small-bodied taxa (Lyman, 2008). As a result of the NG15 excavations, the faunal list for Ngira has been expanded to now include the rodent *Kenyamys*, the Macroscelid *Miorhynchocyon*, and the Galericine *Galerix*, all of which are also known from Rusinga Island.

The paleoecology of the fossil genera observed in this study is not well understood and still relies mostly on comparison with modern analogues. The rodent genus *Paraphiomys* for instance, belongs to the family Thryonomyidae, whose extant representatives (endemic to Africa) live in long grass savanna, swamps and reed beds, do not dig burrows nor climb trees, and feed on coarse grass (Happold, 2013a). Interestingly, these rodents tend to live in small groups, which may explain the concentration of 89 NISP at the NG15 excavation site, though more than half of these occur in the 2BC horizon that is interpreted to contain reworked specimens.

The two extinct genera of the rodent family Pedetidae, *Megapedetes* and *Rusingapedetes*, are morphologically similar to the extant springhares (*Pedetes*) (Butynski, 2013a; Pickford and Mein, 2011). Extant springhares are notorious saltatorial rodents, but are also good diggers. They feed primarily on grasses, live in arid and semiarid, relatively flat and open areas with short grass, with little or no woody vegetation (Butynski, 2013b). The highest density of extant springhares is found near floodplains, lakes, and swamps (Butynski, 2013b), which are within the plausible environments for NG15 based on sedimentary and paleosol evidence.

A recent study of the dental microwear of *Dorcatherium* species from Rusinga Island and Songhor (Ungar et al., 2012) showed that, contrary to extant chevrotains, the fossil tragulids were ecologically diverse in their diet, ranging from variable grazers (*D. chappuisi*) and mixed feeders (*D. parvum*) to browsers/generalists (*D. pigotti*). These authors also suggested that the presence of grazing animals implied that there was at least some grass locally available. At Ngira, both in the NG15 excavations and in the surface collections, all three of these *Dorcatherium* species have been found.

Kenyalagomys belongs to the family Ochotonidae, known from Africa from the early to the middle Miocene, and now only living in Eurasia and North America (Happold, 2013b). The Leporidae migrated to Africa not before the late Miocene (Happold, 2013b). Extant members of the Ochotonidae (i.e. pikas) are smaller than extant Leporidae of Africa, are terrestrial herbivorous animals, and are usually associated with rocks and talus slopes (Happold, 2013b). Interestingly, a recent study showed that pikas have a strong preference for C_3 plants, whereas leporids are more attracted by C_4 plants (especially Poaceae) (Ge et al., 2013). The authors suggested also that the expansion of C_4 plants induced the extinction of ochotonids in Africa to the profit of leporids. We note, however, that the decrease in ochotonid genera began before the C_4 origination date (Ge et al., 2013: Fig. 2.1).

Finally, the genus *Myohyrax* is more enigmatic, as they exhibit highly specialized, ungulate-like hypsodont teeth that are unique among macroscelids (Andrews et al., 1979). Cranial, dental and postcranial features led several authors to suggest a tough diet (e.g. seeds), possibly a saltatorial locomotion, and a predilection for savannah (or "veldt") habitat (Patterson, 1965; Whitworth, 1954).

None of these taxa represents a strict indicator for a forested environment. On the contrary, the reconstructed NG15 small mammal community supports an open floodplain environment with little wood cover. The observations of herbaceous roots and isotopic evidence for at least some C_4 grass imply the availability of fodder for animals adapted to grazing (e.g. hypsodont teeth) and open spaces suitable for fast moving animals (e.g., saltatorial locomotion). The spatially restricted and stratigraphically limited NG15 assemblage does not represent the entirety of the faunal community from Karungu.

Hence, further studies are necessary to understand the faunal and environmental variations within the stratigraphic record preserved at Karungu.

Comparison to Paleoenvironments of the Hiwegi Formation on Rusinga Island

Previous investigations have often treated early Miocene deposits at Karungu and Rusinga Island, specifically the fauna of the Hiwegi Formation, as comparable (Nesbit Evans et al., 1981; Pickford, 1981). However, the results of this study and the work of Driese et al. (2016) call this assumption into question for a number of reasons. First, lithostratigraphic and paleopedologic analyses of the entire sequence indicate a variety of depositional environments (Driese et al., 2016). Additionally, our results, which document differences in the faunal assemblages between surface collections at Ngira and the excavation at NG15, also support the interpretation of multiple paleoenvironments within Ngira. Second, paleoenvironmental interpretations for the Hiwegi Formation on Rusinga Island indicate multiple environments ranging from more open shrubland to riparian woodland to closed-canopy tropical seasonal forest (Collinson et al., 2009; Conrad et al, 2013; Maxbauer et al. 2013; Michel et al., 2014). Third, the paleoenvironmental reconstructions for nearly every Critical Zone component reconstructed for NG15 are different from most recent environmental and climatic reconstructions of the Hiwegi Formation. While the stratigraphy at Ngira consists of interbedded fluvial and lacustrine strata (Driese et al., 2016), sedimentation in the Hiwegi Formation is a mixture of fluvial, palustrine, and primary and reworked volcaniclastic material (e.g, ash fallout and lahars) (Bestland and Krull, 1999; Maxbauer et al., 2013; Michel et al., 2014). This indicates that there were substantial differences in physical sedimentary environments between Karungu and the Hiwegi Formation. We reconstruct

the NG15 interval as an open canopy environment, ranging from an open riparian woodland to a wooded grassland biome. This is similar to, though perhaps more open than, environmental reconstructions for the Grit Member and lower Fossil Bed Member of the Hiwegi Formation, which are reconstructed as a patchwork of woodland and forested biomes within a riparian habitat in a warm and highly seasonal climate in which evaporitic conditions were recurrent (Collinson et al., 2009; Conrad et al., 2013; Maxbauer et al., 2013). Likewise, the interpretations for the NG15 interval are considerably different from the paleoenvironmental reconstruction for the Kibanga Member of the Hiwegi Formation, which is reconstructed to be a closed-canopy, tropical seasonal forest (Michel et al., 2014). Fourth, there are notable differences in the fauna recovered from Karungu and that of the Hiwegi Formation, particularly in the composition and abundance of small mammals and especially primates.

These differences between Karungu and Rusinga Island draw into question the reliability of wholesale comparisons of faunal composition and abundances between early Miocene sites before detailed geologic analyses are performed. For example, Pickford (1981) suggested that the Karungu fauna was most similar to that of the Hiwegi Formation from Rusinga Island (i.e., his faunal Set II). Perhaps the most conspicuous difference between Karungu and the Hiwegi Formation is the rarity of primate taxa at Karungu, in comparison to the relatively common primates found in the Hiwegi Formation. Coupled with evidence for variability in paleoenvironment and paleovegetation through the deposits at Karungu and through the Hiwegi Formation (e.g., this study; Collinson et al., 2009; Maxbauer et al., 2013; Michel et al., 2014; Driese et al., 2016), the differences in the faunal abundance and occurrences between Karungu and

Rusinga Island are likely related to true faunal differences, possibly as a result of paleoenvironment differences.

Compared to the 34 genera (smaller or equal in size with *Megapedetes pentadactylus*) recorded from the Hiwegi formation at Rusinga Island (e.g. Pickford, 1986), the small mammal collections of both the NG15 excavation (10 genera) and the Ngira surface collections (18 genera) are less taxonomically diverse. This could be an artifact of sampling error, but we have exhaustively collected the Ngira deposits at Karungu over the last several years and small mammals are uncommon and carnivore and primate taxa are very rare. Thus we hypothesize that the difference in small mammal diversity and abundance between Karungu and the Hiwegi Formation on Rusinga Island reflect true differences in the fauna. When our results are coupled with recent paleoenvironmental reconstructions from Karungu and the Hiwegi Formation (e.g., Collinson et al., 2009; Conrad et al., 2013; Maxbauer et al., 2013; Michel et al., 2014; Driese et al., 2016), we conclude that a substantial heterogeneity of environments and climates existed in western Kenya in the early Miocene, and the paucity of primates at Karungu is not likely the result of biotic factors alone.

Paleoenvironmental Context in East Africa

In general, early Miocene environments across East Africa are interpreted to have been dominated by tropical forest or woodland vegetation (Andrews and Van Couvering, 1975; Edwards et al., 2010). Stable isotope analyses of compound-specific biomarkers (Uno et al., 2016), pedogenic carbonate (Cerling, 1992), and fossil tooth enamel (Cerling et al., 1998) suggests that C_4 vegetation was not common across East Africa until ca.10 Ma, with a gradual rise of C_4-dominated grasslands starting in the late Miocene at ca. 8

Ma. Nevertheless, several lines of evidence suggest that a patchwork of environments existed in the early Miocene, at least in some parts of the region.

Sediment cores from the Niger River delta show evidence of grass pollen and charred grass cuticle appearing in low abundance at ca. 16 Ma, which is interpreted to signify the initiation of seasonally dry savannahs (Morley and Richards, 1993). A review of Cenozoic vegetation across East Africa by Bonnefille (2010) provides strong evidence for a patchwork of dry, seasonal woodlands to humid forest habitats across the tropical belts of the African continent as early as the late Eocene. Pedogenic carbonates from the Tugen Hills succession near Lake Baringo in Kenya have $\delta^{13}C$ values consistent with mixed C_3 and C_4 vegetation from 15 Ma to Recent (Kingston et al., 1994). Contemporaneous mammals from the same strata in the Tugen Hills also have tooth enamel $\delta^{13}C$ values that are higher than expected for a pure C_3 endmember, and in the absence of vegetation with extreme water stress, those mammals with high $\delta^{13}C$ values likely consumed some portion of C_4 vegetation in their diets (Morgan et al., 1994). Based on the tendency of C_4 vegetation to exist in open canopy conditions in modern ecosystems, it is likely that the Tugen Hills succession contained at least a patchwork of woodland/shrubland to woody grassland environments.

Our observations supporting the presence of open canopy, dry woodland to woody grassland at Karungu are consistent with previous faunal analyses by Andrews and Evans (1979), who compared the composition of modern faunas with that of early Miocene sites. These included a total of 15 species (including microvertebrates) (Andrews, 1974) from Karungu recovered from excavations and sieving from Oswald's (1914) Bed 16. According to our fieldwork, this stratigraphic interval corresponds to

units 20-22 of Driese et al. (2016), 3 to 5 m above NG15. In Andrew and Evans' (1979) analysis, the fauna from Karungu stood out because: 1) its ecological diversity patterns as well as its locomotor adaptations resemble those of non-forest faunas; 2) its taxonomic composition closely resembles that of woodland-bushland faunas (except for the lack of carnivorous species); 3) the smallest size categories predominate the assemblage; and 4) interpreted feeding patterns of the community overall were unlike those in any modern community. Interestingly, unlike the NG15 excavation, this faunal assemblage was dominated by *Kenyalagomys* and *Myohyrax* (74% of the total NISP; Andrews, 1974). But because both taxa have no living relatives in Africa today, Andrews and Evans (1979) considered that this faunal assemblage may either represent a habitat type that is no longer represented in Africa, or was a limited sample from a larger community. Based on similarities in pedogenic carbonate $\delta^{13}C$ values and paleoclimate estimates between NG15 and NG19-NG20, we hypothesize that the fauna recovered from NG20-NG22 also represent open canopy conditions. These environments may not be comparable to any known modern landscape due to the possibly ephemeral and unique nature of early C_4 savannahs or grasslands.

Finally, we posit a possible explanation for the lack of records of C_4 vegetation in recently studied marine cores. Uno et al. (2016) present a compound-specific isotope record from cores taken from the Somali Basin, Gulf of Aden, and Red Sea. Their data offer a large-scale picture of vegetation types in East Africa, but necessarily sample externally-drained continental basins. However, the Ngira locality was potentially an endorheic basin, given the rapid lake level fluctuations documented in the stratigraphy (Driese et al., 2016), and therefore is very unlikely to have contributed to the record of

Uno et al. (2016). This finding underscores the fact that, while a major turnover from C_3 to C_4 vegetation occurred in the late Miocene, much work remains for documenting landscape heterogeneity earlier in the geologic history of East Africa.

Taken together, the observations of pedogenic carbonate $\delta^{13}C$ signatures, paleosol morphology, microcharcoal, and microvertebrate fauna presented in this and previous studies support an interpretation of open canopy conditions within an overall diverse environmental mosaic in the early Miocene of western Kenya.

Conclusions

Early Miocene deposits at Ngira show substantial environmental differences compared to the reconstructions for other contemporaneous primate-bearing deposits in Western Kenya. Climate and vegetation reconstructed for the NG15 stratigraphic interval is consistent with a dry, seasonal subhumid setting with open habitats likely ranging from open riparian woodland to wooded grassland, in which C_4 vegetation may have been an important ecosystem component. These findings differ from previous reconstructions for deposits at Karungu and suggest that either depositional processes or habitat preference are the root causes of differences between the faunal communities at Karungu and Rusinga Island.

The findings presented in this study allow us to present a number of testable hypotheses to explain the scarcity of primate remains at Karungu:

H1) Early Miocene primates did not inhabit the open-canopy environments at Ngira;

H2) Fluvial deposition on relatively low-relief floodplains was less likely to preserve primate remains than volcanic and volcaniclastic sedimentation on higher-relief slopes at Rusinga and Mfangano Islands;

H3) The age for deposits at Karungu is incorrect, and strata are not directly comparable to formations on Rusinga Island.

To test H1, additional early Miocene sites that lack primate remains should be investigated. Because the focus on sedimentary environments of sites in Western Kenya has largely been in conjunction with faunal sites, there is clearly much to learn regarding non-fossiliferous strata. To test H2, taphonomic studies of primate fossils on Rusinga Island and mammalian fossils at Karungu should be compared. Further geochronologic control is needed to test H3, although overall similarities in non-primate fauna suggested that deposits at Karungu are similar in age to the Hiwegi Formation on Rusinga Island (Pickford, 1981, 1986). Pending further investigations, we tentatively favor H1—that early Miocene primates did not favor the environments at Karungu—due to the lack of canopy cover in a more open woodland to woody grassland biome in early Miocene times. While some hominoid primates were clearly adapted to open-canopy conditions by the Pliocene (Cerling et al., 2011), it is yet unknown whether primates exploited non-forested ecosystems where they occurred in the early Miocene. Future investigations of early Miocene paleoclimate and paleoenvironments should include localities that lack primate fossils in order to test the relative importance of biotic versus environmental controls on the occurrence of primates in the fossil record.

Acknowledgments

Funding for this research was provided by the National Science Foundation (BCS #124812 to SGD and DJP, and BCS #1241807 to KPM and DLF), by the Karl und Marie Schack-Stiftung to TL, by the Vereinigung von Freunden und Förderern der Goethe-Universität Frankfurt to TL, and the Baylor University Geology Department. We are grateful to the Kenyan government and National Museums of Kenya and Dr. F. Kyalo Manti for facilitating our work. Invaluable field assistance was provided by K. Jenkins, D. Aketch, T. Cicak, M. Fuchs, C. Hemm, R. Henning, U. Menz, S.N. Muteti, S.O. Oloo, D. Obura, C. Ochieng, J. Ouma, T. Rumpf, J. Tausch, T. Wenzel, W. Odhiambo, S. Odhiambo, B.A. Obonyo, J.L. Otieno, F. Odeny, J.O. Orembe., K. Ogondo, and J. Shaduma. Logistical support was provided by J. Siembo. We thank associated editor G.E. Stinchcomb and two reviewers for careful and constructive reviews. This manuscript is publication #6 supporting Research on East African Catarrhine and Hominoid Evolution (REACHE).

CHAPTER FOUR

Reconstructing pH of Paleosols Using Geochemical Proxies

This chapter published as: Lukens, W.E., Nordt, L.E., Stinchcomb, G.E., Driese, S.G., Tubbs. J.D., and Barnard, B., *under review,* Reconstructing pH of paleosols using geochemical proxies: *The Journal of Geology*.

Abstract

Soil pH is essential to understanding weathering, nutrient availability, and biological-edaphic relationships. However, standard pH measurement on soils requires friable material, thereby excluding most paleosols. In this manuscript, bulk geochemical proxies for pH are developed for soil B horizons using indices that track pH-dependent mineralogical transformations. Geochemical relationships within a continental-scale data set of modern soils (n=619) were explored using principal components analysis, which revealed a close association between pH and log-transformed CaO, and little influence of refractory oxides on pH. These results guided the formulation of three geochemical indices that consist of ratios of Fe_2O_3, TiO_2, and Al_2O_3 to CaO, herein referred to as FeCa, TiCa and AlCa. Each index has similar predictive capacity for pH (r^2 = 0.67-68, RMSE = 0.82-0.84). The models were tested using an internal cross-validation, which returned model fitness and prediction errors similar to regression results (r^2 = 0.66-68, RMSPE = 0.82-0.86). While soil pH shows a significant correlation with mean annual precipitation, partial correlation analysis of FeCa, TiCa, AlCa, and a number of widely-used paleosol weathering indices revealed that the relationship between B horizon composition and pH is significant even when climate is held constant. This finding

implies that bulk geochemical indices used in pedotransfer functions for climate primarily track pH, which, in turn, responds to climate state. A case study is examined, where the pH transfer functions were applied on a succession of Triassic alluvial paleosols that experienced a large range of soil-forming conditions. Reconstructed pH values closely track interpreted vegetation, climate, and pedogenesis. These pedotransfer functions offer a new pathway to estimate an ecologically-significant parameter in deep-time Critical Zones.

Introduction

Paleopedology is a fundamental tool in the study of deep-time Critical Zones ((Nordt and Driese, 2013). Reconstruction of climate parameters from paleosols have been a priority of the paleosol community, primarily due to correlations between soil B horizon chemistry and climate (Sheldon et al., 2002; Nordt and Driese, 2010b; Gallagher and Sheldon, 2013). However, modern Critical Zone science (www.criticalzone.org/national/) is concerned with a broad array of biogeochemical processes, including regolith production (Ma et al., 2010; Dere et al., 2013; Riebe et al., 2017), soil O_2 and CO_2 fluxes (Hasenmueller et al., 2015), and colloidal microenvironments (Chorover et al., 2007). For paleopedology to become a contributing component of deep-time Critical Zone science, geochemical proxies for paleosols must expand beyond the focus on climatic factors alone (Nordt et al., 2012; Nordt and Driese, 2013).

With the advent of soil characterization proxies for Vertisols, such as pH, base saturation, cation exchange capacity, and organic C, (Nordt and Driese, 2010a; Nordt et al., 2013), the linkages between deep-time Critical Zone components can now be

assessed in some geologic settings (Nordt et al., 2012; Nordt and Driese, 2013; Beverly et al., 2015; Driese et al., 2016). Such studies underscore the need for further edaphic proxy development. A broadly applicable method of quantifying pH in paleosols is an essential first approach, as it offers context for understanding mineral authigenesis (e.g., clays, Wilson, 1999), bioavailability of nutrients (e.g., phosphorus, Devau et al., 2009), climatic influence on pedogenesis (Kämpf and Schwertmann, 1983), microbial productivity and diversity (Aciego Pietri and Brookes, 2008; Lauber et al., 2009), and, ultimately, the former geochemical state of a paleosol.

Soil pH is a measure of the H^+ activity in dynamic equilibrium between pore water and exchange sites in the diffuse double layer of colloids (Miller and Kissel, 2010; Nordt et al., 2013), typically analyzed with an electronic probe submersed in a 1:1 soil-water mixture (Soil Survey Laboratory Staff, 1992). Other methods include the use of colored dyes or soil-salt mixtures (Soil Survey Laboratory Staff, 1992). The pH of consolidated paleosols is typically assessed using the qualitative HCl field test, a visual estimate of the degree of effervescence (Schoeneberger et al., 2012).

In the soil system, acidity and alkalinity are mediated by mineral solubility, such that: A) carbonates act as an alkaline buffer at pH ca. 8.3, B) hydrolysis of framework aluminosilicates consumes H^+ and releases base cations at circumneutral pH (6-7.5), C) advanced acid attack on aluminosilicates with progressive base cation loss continues at acid pH (4-6), and D) after silicate minerals are exhausted, 1:1 clays and Al oxyhydroxides stabilize pH between 3-4 (Thomas, 1996; Chadwick and Chorover, 2001). Nutrient availability is optimized in the circumneutral to mildly acidic range (Brady and Weil, 2008; Nordt et al., 2013). Most plant growth is significantly inhibited by sodium

toxicity and nutrient limitation at high pH (Qadir and Schubert, 2002) or aluminum toxicity and free acids at low pH (Delhaize and Ryan, 1995; Beyrouty et al., 2000).

Notably, pH reflects geochemical composition at the time of measurement, regardless of whether soil mineralogy is dominated by pedogenic (secondary) minerals or inherited parent materials. For example, a mature soil with well-formed calcic horizons that developed on noncalcareous parent material and an incipient soil developed on limestone would both be alkaline. Thus, the influence of parent materials on soil composition poses a potential disjuncture between bulk geochemistry and climate, and likely contributes to the error of soil-based proxies for specific climate variables (Jenny, 1941, 1994; Stinchcomb et al., 2016). In the case of paleosols, pH values would represent the last snapshot of soil chemistry before burial.

A limited number of approaches have been used to quantify paleosol pH. To our knowledge, Nordt et al. (2012) and Nordt et al. (2013) are the only two studies that have attempted direct measurements of pH on lithified paleosols. Nordt et al. (2012) used the 1:1 soil-water method (Soil Survey Laboratory Staff, 1992) to measure pH values of 7.6-8.2 on an unusually well-preserved early Paleocene Vertisol. These values were consistent with the presence of pedogenic calcite and smectite-dominated clay fraction. In contrast, Nordt et al. (2013) used powdered dyes to measure a pH of 8-8.5 from a more deeply buried late Triassic Vertisol, which is more alkaline than expected given the lack of pedogenic calcite and the mixed clay mineral assemblage. Such measurements suggest that diagenesis can either alter the exchange complex, or compaction prevents accurate measurements of H^+ activity.

Because pH controls mineral dissolution and authigenesis in soils, the bulk geochemistry of a soil or paleosol should serve as a proxy for pH (Nordt and Driese, 2010a; Sharma et al., 2014). We hypothesize that the concentration of bulk CaO is inversely correlated with pH, as calcite is the most common soil carbonate in alkaline settings, and Ca^{2+} is typically the most abundant exchangeable base in soils with circumneutral pH (Brady and Weil, 2008). Transitions to acidic pH remove Ca^{2+} due to the stronger affinity of Al^{3+} for colloidal exchange sites, resulting in a net decrease in total Ca as pH lowers (Chadwick and Chorover, 2001). Therefore, we expect ratios of Ca to Al to improve predictive models for pH due to the dichotomous relationship of the alkaline carbonate and acidic Al oxyhydroxide buffers (Thomas and Hargrove, 1984; Chadwick and Chorover, 2001).

Bulk-measured CaO from B horizons is already used in a number of widely utilized paleosol proxies for climate, including the chemical index of alteration minus potassium (CIA-K, (Sheldon et al., 2002), CALMAG (Nordt and Driese, 2010b), the paleosol weathering index (PWI, Gallagher and Sheldon, 2013), and the paleosol-paleoclimate model ($PPM_{1.0}$, Stinchcomb et al., 2016). These proxies are now routinely applied throughout the geologic record (Nesbitt and Young, 1982; Maynard, 1992; Kahmann and Driese, 2008; Beverly et al., 2015; Nordt et al., 2015; Driese and Ashley, 2016; Sheldon et al., 2016), and the extension of bulk geochemical indices to the reconstruction of edaphic variables is necessary in order to advance the growing discipline of deep-time Critical Zone science.

In this paper, we first explore relationships between observed geochemistry and pH of a suite of modern soils using principal components analysis (PCA). The results of

PCA are vetted using first-principles of soil processes and tested for possible covariation with climate parameters. The empirically-derived relationships between geochemical constituents and pH are then modelled using regression analysis and vetted using internal cross-validation. Finally, the predictive relationships are applied on a succession of deep-time paleosols that span a wide range of soil-forming conditions in order to demonstrate the utility of pH reconstruction in paleosol studies.

Methods

Data Set

A data set of 685 modern soil B horizons (Stinchcomb et al., 2016) was modified to derive relationships between bulk geochemistry and pH. Details of the original data compilation are reported in (Stinchcomb et al., 2016). In all, the uppermost B horizons from 619 pedons with reported geochemistry, pH measurements, and no known anthropogenic alteration were selected for this study. Profile descriptions, characterization data, and elemental compositions are reported in the online Geosciences Dataverse data repository hosted by the Texas Data Repository (doi: 10.18738/T8/CAFPD7). The uppermost B horizon was chosen to minimize parent material influences on geochemistry from underlying horizons, and because A horizons are comparatively rare in the geologic record (Sheldon and Tabor, 2009).

The geochemical data for ten major elements compiled by Stinchcomb et al. (2016) were from samples prepared following the methods of Soil Survey Investigations Report 42 (Soil Survey Staff, 1996). Samples were analyzed on the air-dried, < 2 mm fraction using microwave digestion combined with HF-HNO_3-HCl digestion, followed by neutralization in boric acid and inductively coupled plasma atomic emission spectrometry

(ICP-AES, Burt et al., 2003). One additional element (Mn) was measured using microwave digestion with HNO_3-HCl (aqua regia) followed by ICP-AES (Burt et al., 2003). The pH measurements used in this study are from the 1:1 soil-water mixture method (Stinchcomb et al., 2016).

The soils in the data set formed under a broad range of environmental and climatic settings to maintain the widest possible applicability of the proxies derived herein (Figs. 2.1, 2.2). Ten soil orders are represented and exclude only Histosols and Gelisols. Most horizons are some variety of Bt or Bw horizon (which include Btk, Btkg, etc.), and, in theory, the functions reported in this study could be applied to any B horizon type in the data set. Of the five soil-forming factors (Jenny, 1994), duration of pedogenesis is the only unconstrained variable, though the presence of soils from Entisols with weakly formed B horizons to Oxisols suggests that the data set includes soils formed for 10^0 to $>10^6$ years (Birkeland, 1999). The ranges of mean annual precipitation (MAP) and temperature (MAT) span 130-6866 mm and 0-27°C, respectively. Vegetation cover includes desert scrub to tropical forest. Relief ranges from 0-85°, though the majority of soils formed on slopes of < 5°. Parent materials include alluvium, colluvium, loess, eolian sand, marine sediments, glacial sediments, glacial till, lacustrine mud, volcanic ash, and felsic to mafic residuum. The data set includes soils with pH values between 3.5 and 10.5.

Principal Components Analysis

Principal components analysis (PCA) is a multivariate exploratory technique commonly used in the geosciences to elucidate relationships within complex, large data

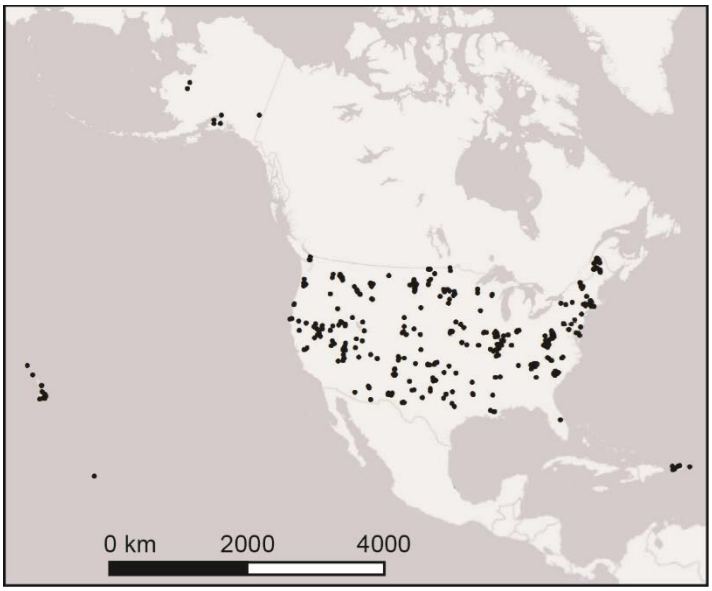

Figure 3.1. Map of sample locations (n = 619). Sample localities include areas on Hawaii, Guam, Puerto Rico, U.S. Virgin Islands, Alaska, and the continental United States.

sets (Helena et al., 2000; Farnham et al., 2003; Farnham et al., 2003; Borůvka et al., 2005; Borůvka et al., 2007; Li et al., 2007; Mandal et al., 2008). In this study, PCA was performed on correlations using JMP software v.13.0.0 (*JMP*, 2016). Each principal component (PC) is a linear combination of an eigenvector of the correlation matrix, with eigenvalues representing the variance of each PC (Davis, 1986). Because the correlation matrix is square with dimensions equal to the number of input variables, the number of PCs always equals the number of input variables, and all PCs will necessarily be orthogonal. Observations are projected onto the PCs and referred to as PC scores. The coefficients of the equation defined by each eigenvector is the vector loading, which is computed for each variable along each PC and signifies the importance of the variable in generating the PC. Taken together, the PC scores and loadings can be used to infer underlying processes or latent structures acting to organize the set of observations, typically by using only the first few PCs that explain most of the data variance. The

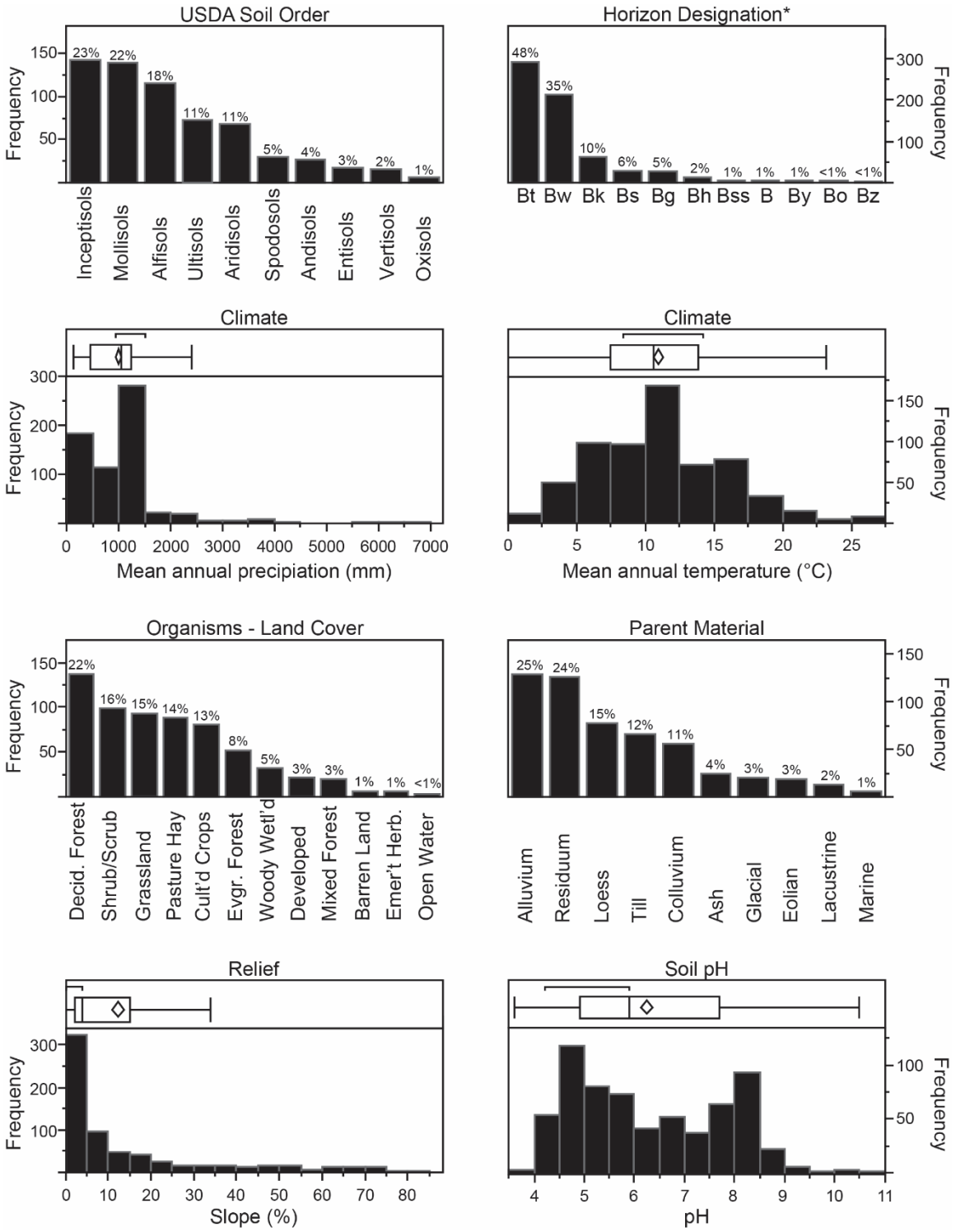

Figure 3.2. Histograms of selected characteristics for the 619 uppermost B horizons used to develop the pH proxies (after Stinchcomb et al., 2016). Distributions are presented as frequencies, and percentages are shown for categorical variables. Box and whisker plots are shown for numerical variables. On box and whisker plots, diamonds indicate the 95% confidence interval about the mean, and brackets above the boxes identify the shortest half of the data, a measure of distribution density. *Frequencies are shown for all horizons containing the subordinate indicator (t, s, k, etc.). For example, a Btk horizon is counted in both the Bt and the Bk columns. See Soil Survey Staff (1993) horizon designation definitions.

practical utility of PCA in soil geochemistry lies in the fact that commonly-occurring elemental oxides with similar geochemical affinity will be collinear (e.g., the base oxides). The PCs projected through such observations will capture the variance of multiple inputs along a lower number of axes, thereby reducing dimensionality and maximizing variance in a new coordinate system (Krzanowski, 1988).

Prior to running PCA, CaO, MgO, and Na_2O were natural log-transformed—hereafter referred to as *l*CaO, *l*MgO, and *l*Na_2O—to improve normality of distributions and prevent outlier values from influencing results. To further correct for differences in variance and magnitude between variables, PCA was run on correlations (not covariances), which first centers and scales the input data. Geochemical predictors of pH were assessed by analyzing the distribution of PC scores within categories of soil forming factors, and by graphical interpretation of loading vectors on PC biplots.

Regression Analysis

The results of PCA informed the construction of geochemical indices used in regression analysis. Elemental oxides determined to be associated with pH were used as predictor (mobile) oxides, whereas those least correlated with pH were used as recalcitrant (immobile) oxides. Predictor and recalcitrant oxides were transformed into geochemical indices according to the formula:

$$\frac{R}{R+X_1+X_2 \ldots X_n} \times 100, \quad (1)$$

where R represents a recalcitrant oxide and X_1, X_2, … X_n represent predictor oxides. These ratios are structured after the chemical index of alteration (CIA), where $R = Al_2O_3$, $X_1 = CaO$, $X_2 = Na_2O$, and $X_3 = K_2O$ (Nesbitt and Young, 1982). Two variations of Eq. 1 have been widely used for predicting MAP in paleosols: CIA-K (Maynard, 1992;

Sheldon et al., 2002), where R = Al_2O_3, X_1 = CaO, and X_2 = Na_2O, and CALMAG (Nordt and Driese, 2010b), where MgO is substituted for Na_2O in X_2, and neither index incorporates K_2O. The structure of Eq. 1 is such that index values approach 0 or 100 when mobile constituents are progressively added to or leached from a soil, respectively. The transformation should thereby correct for extreme values of input data by driving the index in either direction. A range of pH values from 3.5 to 10.5 were used in this study.

The geochemical indices constructed in light of PCA results were regressed against pH, with combinations of candidate predictor and recalcitrant oxides iteratively included. Indices that conformed to first principles theory and contained the most robust regression statistics were selected as pH proxies and cross-validated.

Principal Components Analysis Results

PCA and Pedogenic Processes

The twelve input variables (11 oxides and pH) resulted in twelve principal components. The first three PCs explain 31.8%, 24.4%, and 11.2% of the total variance, with each additional axis explaining ca. 7% or less of the total variance (Fig. 3.3). We therefore omit PCs 4-12 from further discussion. In general, the amount of variance explained by PCs 1-3 is similar to other studies of geologic data (Helena et al., 2000; Borůvka et al., 2005; Borůvka et al., 2007), and, in this case, reflects the natural variability in factors of soil formation that drive geochemistry and pH across such a large variety of settings.

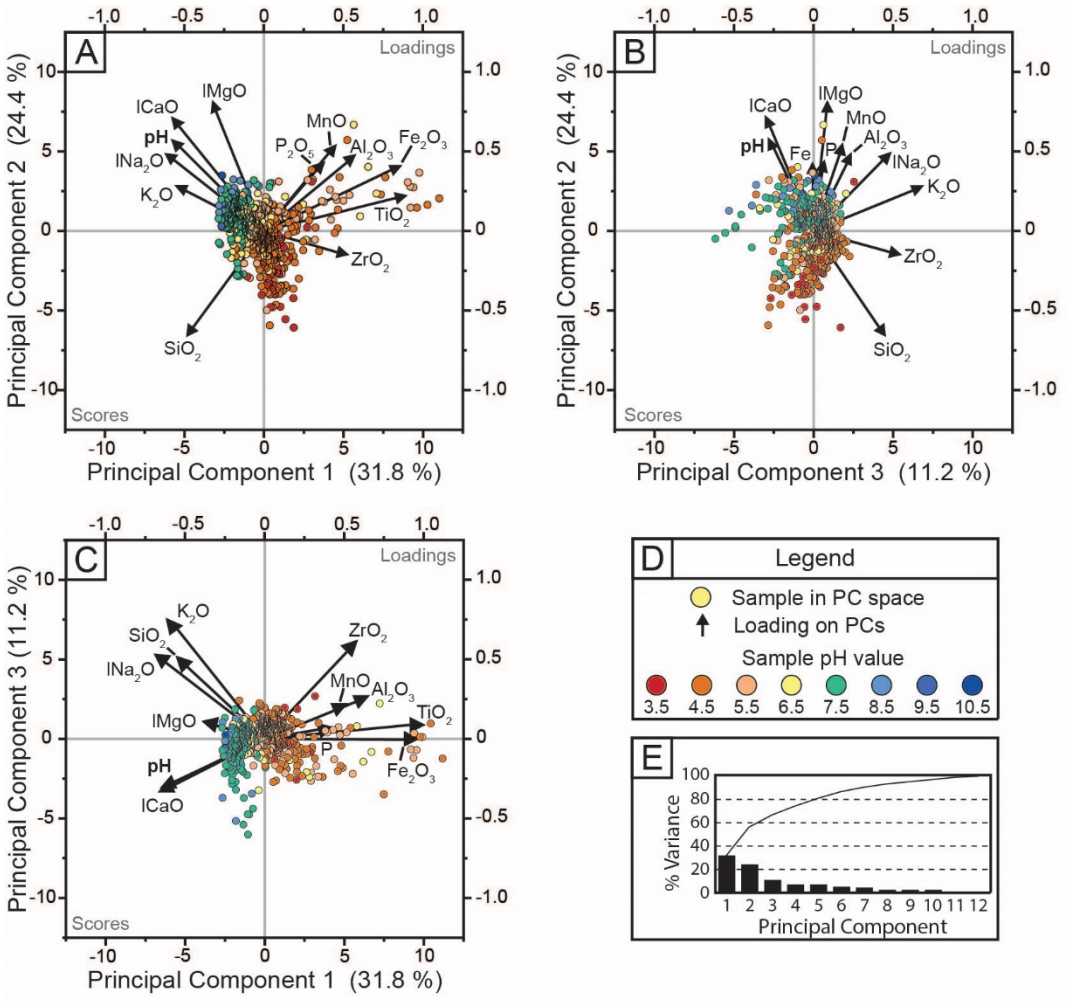

Figure 3.3. Principal components analysis (PCA) biplots, with sample scores overlain on oxide loading vectors. On each biplot, the left and bottom axes are sample scores scales; the right and top axes are loading vector scales. All oxides were input as weight percent. Parentheses: total variance in the training data set explained by each principal component (PC). A) On PCs 1 and 2, increases in pH are tracked by base oxides, notably lCaO. B) pH is correlated with lCaO on PCs 2 and 3. C) pH is correlated with lCaO on PCs 1 and 3. D) Legend of pH values for individual samples. E) Percent of the total variance explained by each PC, with a line denoting cumulative variance explained. PCs 4-12 each explain < 7% of the total variance in the data set and are omitted from discussion.

Cross-plots of sample scores overlain on input variable loading vectors are shown in Fig. 3.3 for the first three PCs. In Fig. 3.3A, the pH loading vector extends into the second quadrant, oriented roughly 45° from PCs 1 and 2. Because both PCs 1 and 2

describe aspects of pH variance, geochemical trends and factors of soil formation within the sample data are discussed in terms of both PCs 1 and 2. The combination of PCs 1 and 2 reveal four general patterns in the data (Fig. 3.3A): 1) pH and the base oxides cluster at negative values on PC 1 and positive values on PC 2 (second quadrant); 2) P_2O_5, MnO, and the refractory metals Al_2O_3, Fe_2O_3, and TiO_2 cluster at positive values on PCs 1 and 2 (first quadrant) and were generally orthogonal to the pH loading vector; 3) SiO_2 is loaded orthogonally to the base oxides and pH (third quadrant), and is negatively correlated with the refractory metals; and 4) ZrO_2 is loaded positively on PC 1, similar to the refractory metals, but is loaded negatively on PC 2 (fourth quadrant).

Although PC 3 explains little of the overall variance in the data set, the correlation between *l*CaO and pH is evident by their similar loading vectors. The inverse correlation between *l*Na_2O, K_2O, and SiO_2 with pH and *l*CaO on PC 3 is evidence that an ancillary process is influencing soil geochemical variance independent of the factors that ordered samples on PCs 1 and 2.

The following examination of sample scores on each PC is organized after Jenny's (1941) factors of soil formation, namely climate, organisms, parent material, topographic relief, and time, with additional focus paid to NRCS soil taxonomy and selected measures of soil mineralogy.

Climate. Pairwise correlations with each PC are presented in Table 3.1 for input oxides, pH, MAP, and MAT. This tabulation is an alternative representation of the coordinates of loading vectors on each PC, and aids in understanding the role of climate in shaping the elemental-pH space. Along PC 1, the climate parameters MAP and MAT are positively correlated with the refractory metals and negatively correlated with the

Table 3.1. Correlations with principal components.

Variable	PC 1	PC 2	PC 3
Fe_2O_3	0.90	0.15	-0.01
MnO	0.58	0.30	0.29
P_2O_5	0.46	0.28	0.20
SiO_2	-0.59	-0.64	0.30
TiO_2	0.89	0.06[a]	-0.05[a]
ZrO_2	0.46	-0.44	0.12
Al_2O_3	0.67	0.13	0.37
lCaO	-0.33	0.78	0.03[a]
lMgO	-0.05[a]	0.68	0.26
lNa_2O	-0.38	0.35	0.63
K_2O	-0.38	0.13	0.73
pH	-0.38	0.70	0.10[b]
MAP	0.63	-0.23	-0.13
MAT	0.34	0.02[a]	-0.26

Note. Correlation coefficients are reported as Pearson's r. All correlations are significant with $p < 0.001$, unless noted otherwise. [a] Correlation is not significant ($p > 0.05$). [b] Correlation is significant at $p < 0.05$.

base oxides and SiO_2. PC 2 shows a strong positive correlation with pH and the bases, and MAP is negatively correlated with PC 2. MAT is not correlated with PC 2. *l*Na_2O and K_2O show a strong positive correlation with PC 3, which is negatively correlated with MAT.

Vegetation. Land cover classes associated with each soil in the data set were extracted from the United States Geological Survey (USGS) National Land Cover Dataset (NLCD) of 2001 (Homer et al., 2007). The distribution of each land cover class was studied with respect to sample scores on PCs 1-3 (Fig. 3.4A-C). The land cover categories that tend to score negatively on PC 1 and positively on PC 2—similar to the trend of increasing pH values (Fig. 3.3A)—include barren lands, emergent herbaceous, grasslands, and shrub/scrublands. A number of samples within the deciduous forest,

evergreen forest, mixed forest, and woody wetlands land cover classes have positive scores on both PCs 1 and 2, consistent with samples that plot with the loading vectors of the refractory metals, P_2O_5, and MnO in the first quadrant on Fig. 3.3A. Most of the other land cover categories are distributed about zero on each PC. On PC 3, all samples are distributed about zero, though barren lands, evergreen forests, and shrub/scrublands show notably high variance.

To study possible functional relationships between biomes, soil pH, and soil geochemistry, land cover categories were stratified into bins that broadly capture differences in biome types. The grass/herbaceous bin includes the grasslands and emergent herbaceous classes, the shrub/scrubland bin includes only the shrub/scrubland class, and the tree bin includes deciduous forests, evergreen forests, mixed forests, and woody wetlands (Fig. 3.4D-L). The Kruskall-Wallis test was run on PC scores, stratified by simplified land cover category, with the null hypothesis that the ranks of PC scores are the same for each category. For PCs 1 and 2, the null hypothesis is rejected ($p < 0.001$) and the scores for each category were not of the same rank. For PC 3, the null hypothesis could not be rejected ($p = 0.37$). Pairwise Wilcoxon rank sum tests were run post-hoc and yielded the following results: for PC 1, all comparisons were unequal ($p < 0.001$) and the median scores decreased from tree → grass → shrub; for PC 2, all comparisons were unequal ($p < 0.001$) and median scores decreased from shrub → grass → tree. Notably, these broadly-defined land cover classes show a gradational transition from tree → grass → shrub cover classes from the fourth to second quadrants in Fig. 3.3A, parallel to the pH and base oxide loading vectors. This suggests that open, water-stressed habitats have

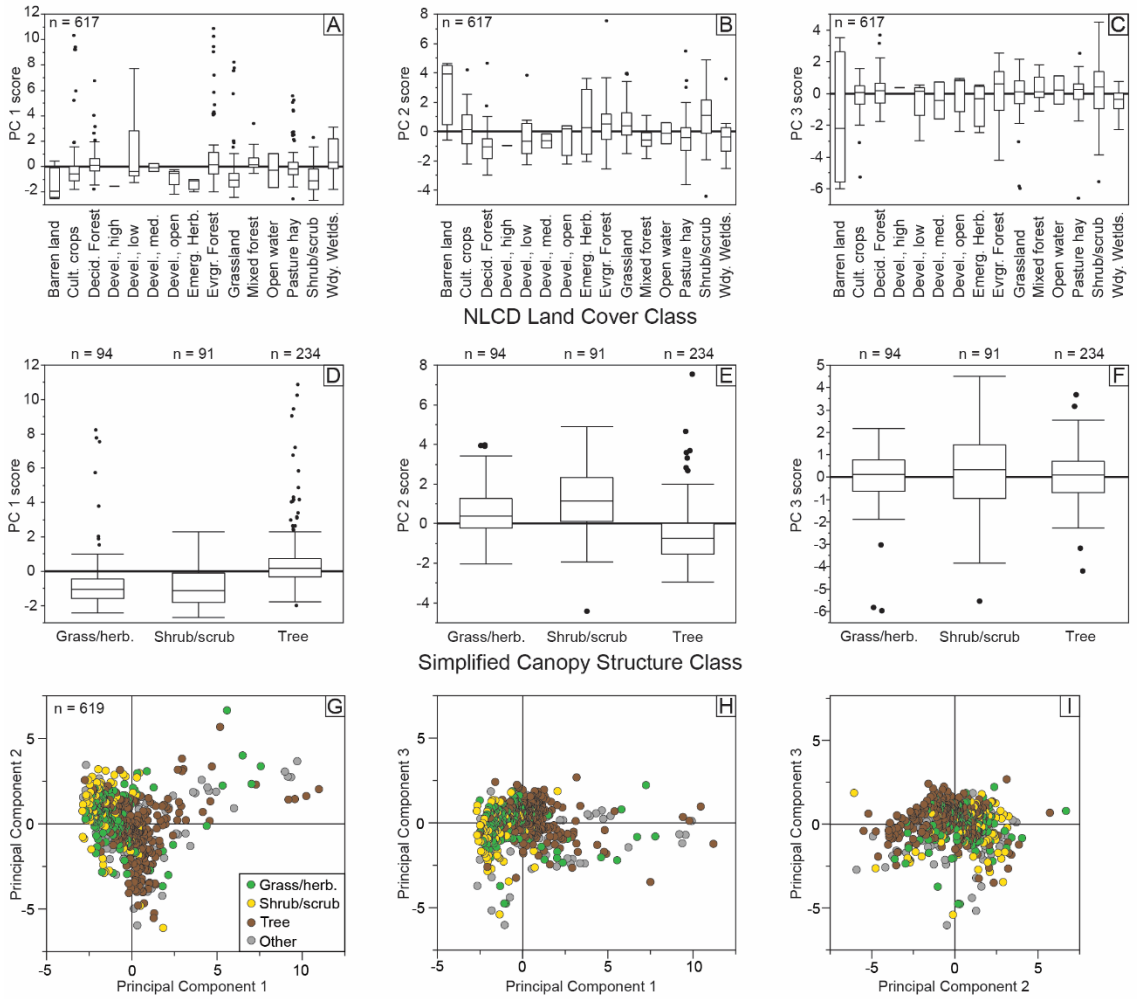

Figure 3.4. Landcover classes plotted against PC scores. A-C) All NLCD landcover classes plotted by PC score for PCs 1-3. Thick black line denotes a PC score of zero. D-F) Landcover classes binned by grassland/herbaceous, shrub/scrubland, and tree biomes. For PCs 1 and 2, ranks of the PC scores by landcover category are not the same (Kruskall-Wallis test, $p < 0.001$). For PC 3, ranks of PC scores are not dissimilar (Kruskall-Wallis test, $p = 0.37$). G-I) PC biplots with samples color coded for biome category. Note differentiation of tree, shrub/scrubland, and grassland/herbaceous bins follows the trajectory of increases in pH (see Fig. 3.3).

higher pH values, which are recorded in whole-soil geochemistry as increases in base oxide concentrations.

Relief. No significant correlations were found between PC scores and slope angle, slope aspect, elevation, latitude, or longitude.

Parent Material. Parent material categories show several notable trends with respect to PC scores (Fig. 3.5). Alluvium, eolian sand, glacial sediments, and loess generally plot in the second quadrant of PCs 1 and 2 (Fig. 3.5D), with some variability. Most samples from these categories have circumneutral to alkaline pH, although some acidic soils are present in each bin. Soils formed on lacustrine sediments almost exclusively plot in the second quadrant (Fig. 3.5D), with a median pH of 8.2 and all values above 6.7. Many of the soils formed on ash, colluvium and residuum plot at extreme positive PC 1 and 2 scores, and the upper quartile of each category is at or below pH of 7. Soils with marine parent materials plot at very negative PC 2 scores in the fourth quadrant (Fig. 3.5D). These soils all have pH values between 4.3-4.8 and sandy textures (sandy loam to sandy clay loam), and therefore have low pH associated with low acid neutralizing capacity rather than acid sulfate processes due to pyrite oxidation (Van Breemen, 1982). Finally, soils formed on till plot generally near the origin, with pH ranging from 3.6-8.1.

On PC 3, eolian and marine parented soils plot at negative values, while nearly all colluvium and loess parented soils plot at positive values. Soils formed on lacustrine sediments and residuum, as well as a few soils with alluvial parent materials, are associated with most of the extreme negative PC scores. All other parent materials vary about zero.

The influence of parent material type on B horizon geochemistry and pH is highly variable, with the noted exceptions of soils formed on ash and the limited number of samples associated with lacustrine mud and marine sand. High variability within parent material classes is driven by the combined effect of other soil-forming factors that act to

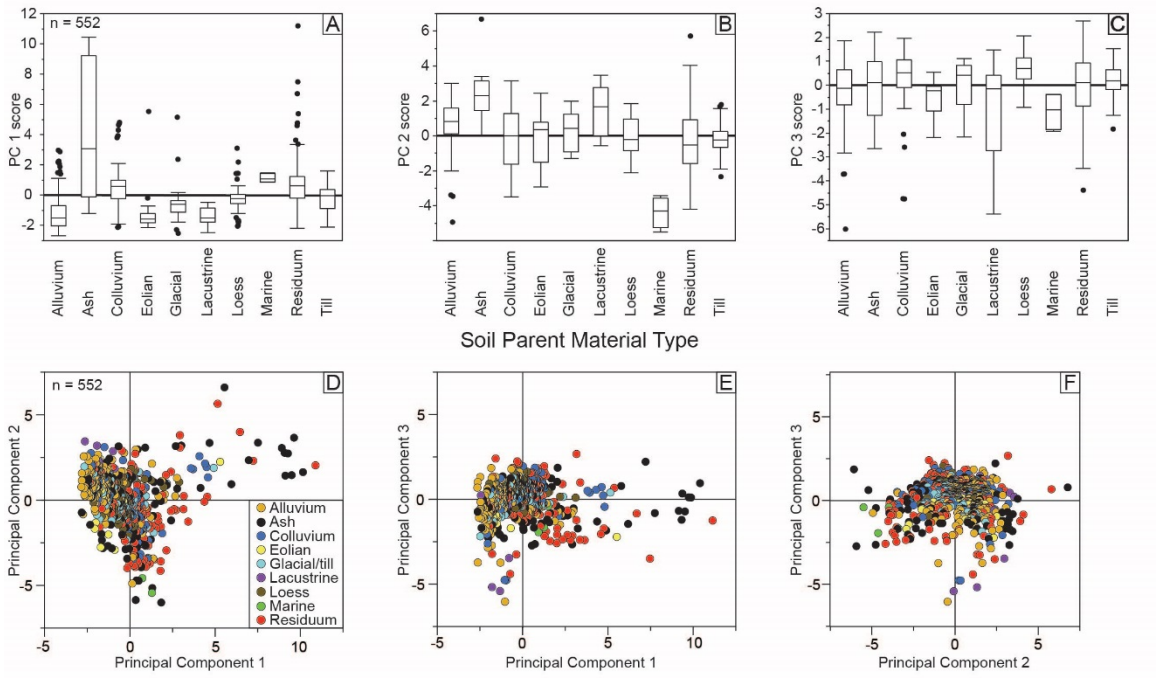

Figure 3.5. Parent material classes plotted against PC scores. Thick black line denotes a PC score of zero. A) Most extreme positive values are associated with soils formed on ash, residuum, and colluvium. B) Most parent material categories span the variance along PC 2. Extreme negative values are associated with soils formed on marine sediments. C) All samples plot about zero on PC 3. D-F) PC biplots with samples coded for each parent material class. Note that most first quadrant soils in D are soils formed on ash or residuum.

modify and redistribute primary geochemical constituents. This finding is promising, as it offers further evidence that soil geochemistry adjusts to local environmental factors, and that parent material is not the primary influence on pH for most soils.

Time and Taxonomy. As mentioned previously, time of pedogenesis is not well constrained for most soils in the data set. However, some soil taxonomic categories offer information on soil maturity and will be discussed in lieu of quantified pedogenic duration. The organization of NRCS-classified soil orders along PCs 1 and 2 clarifies some of the underlying processes organizing the data (Fig. 3.6). Soils with negative PC 1

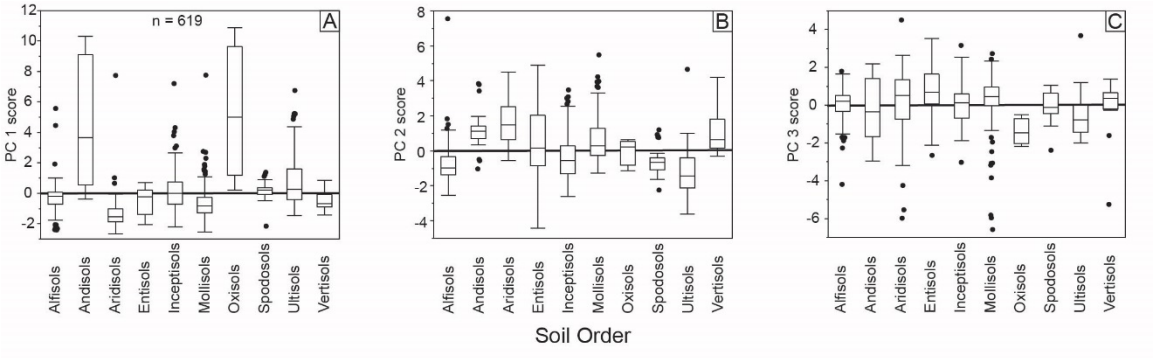

Figure 3.6. Soil taxonomic categories plotted against PC scores. A-C) Soil order plotted against PC scores. Note Andisols and Oxisols tend to have positive scores, whereas Aridisols, Mollisols, and Vertisols tend to have negative scores on PC 1.

and positive PC 2 scores (second quadrant, Fig. 3.3A) include the Aridisols, Vertisols, and Mollisols. These soils tend to be alkaline and rich in either 2:1 clays and/or carbonates (Soil Survey Staff, 2014). Soils with either positive PC 1 scores or negative PC 2 scores include the Andisols, Oxisols, and Ultisols, which have exclusively acidic pH. Whereas Ultisols and Oxisols are acidic due to protracted leaching in warm-wet climates, Andisols tend to be acidic due to the dominance of Al-organic complexes in cation exchange sites, which inhibits base retention (Soil Survey Staff, 2014). Furthermore, the strong correlation between PC 1 and P_2O_5 is likely driven by high phosphate retention in Andisols (e.g., Shoji, 1987).

Alfisols, Inceptisols, and Entisols are variable across each PC, and have pH values that span the range of the data set. This is likely due to the short to moderate time scales of pedogenesis and large variance in environmental settings associated with these soil orders. Accordingly, the relationship between geochemistry and pH stratified by these soil orders is confounded by other soil forming factors (e.g., climate, vegetation, or parent materials). Spodosols are roughly centered about zero on PCs 1 and 2, and all have acidic pH. All soil orders tend to be centered about zero along PC 3, with the exception

that Oxisols and Ultisols tend to have negative scores, and some Aridisol and Mollisols plot at extreme negative scores.

Soil Mineralogy. Soil mineral class is a taxonomic category that describes the dominant mineralogy observed in a soil profile (Soil Survey Staff, 1993). The distribution of PC scores by mineral class is presented in Fig. 3.7A-C. Soils with negative PC 1 and positive PC 2 scores include those with carbonatic (calcareous), gypsic, and magnesic mineral classes, and are neutral to alkaline. Iron-rich soils are binned as "ferruginous" but also include the ferritic classes. These soils are exclusively associated with positive PC 1 and 2 scores and are acidic (pH 5-5.2). Kaolinitic, paramicaceous, parasqesquic, and sesquic soils plot at generally positive PC 1 and negative PC 2 scores and are almost exclusively acidic. Siliceous soils are unique in that they have negative scores on both PCs 1 and 2, which likely explains the orientation of the SiO_2 loading vector (Fig. 3.3A). The short range order (SRO) bin contains all soils with andic properties, which includes the isotic, glassy, ferrihydritic, and amorphic mineral classes. These samples vary about zero for PCs 1 and 2, but also include extreme positive values on both PCs. The pH values for the SRO soils varies from extremely acidic to neutral. Soils with mixed and smectitic mineral classes have high variance, which is promising given that many paleosols likely fall into these categories.

Two measures of soil mineralogy common to alkaline soils include carbonate content (reported as wt. %) and the presence of soluble salts (Fig. 3.7D-J). A total of 134 soils in the data set have reported values for $CaCO_3$ content and salt presence. When plotted against PC scores, calcareous soils have almost exclusively negative scores on PC

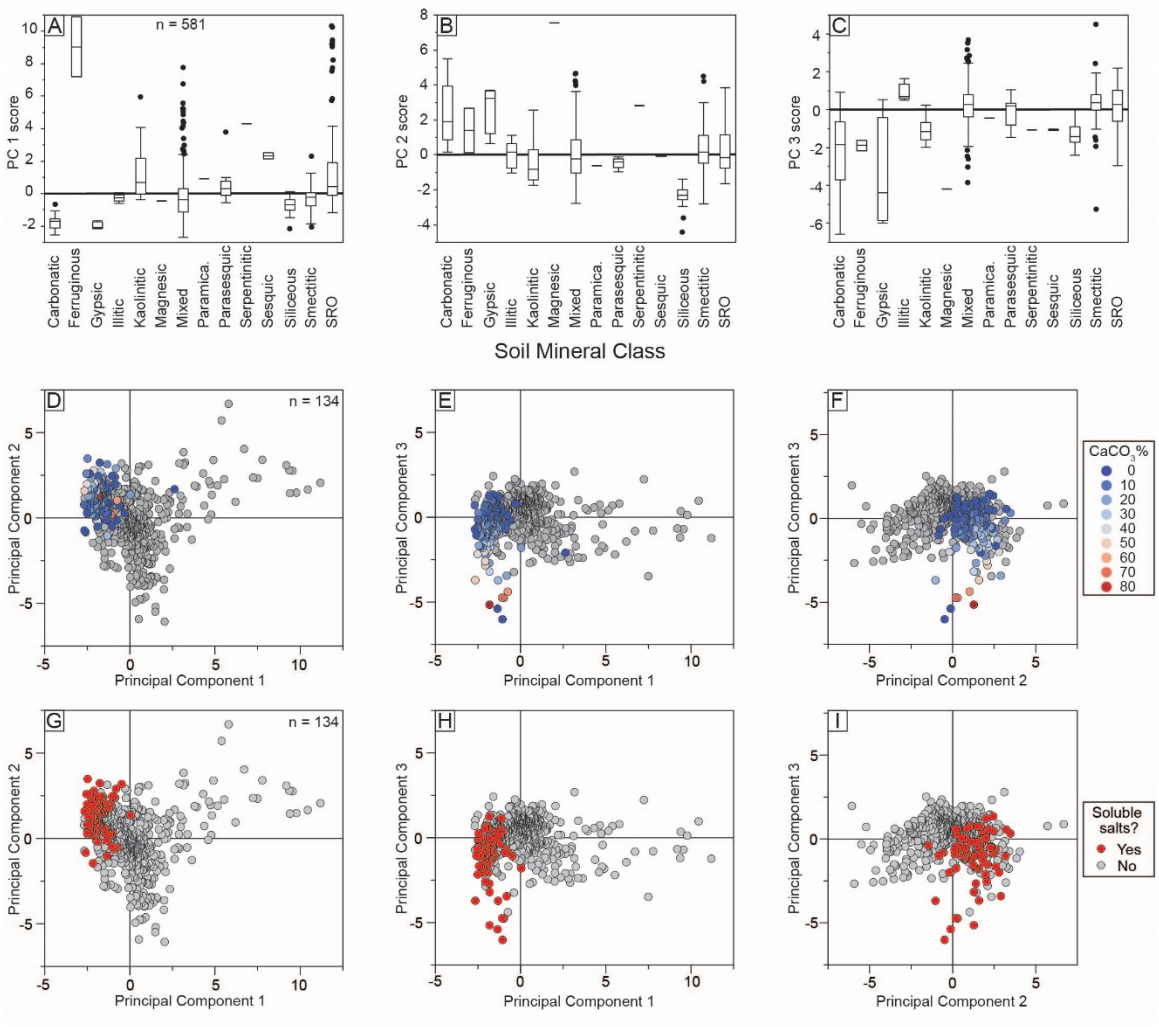

Figure 3.7. Mineralogy classes plotted against PC scores. A-B) Soils associated with intense weathering or have andic properties tend to have extreme positive values on PCs 1 and 2 (ferruginous, kaolinite, mixed, and short range order, or SRO). Soils associated with drylands or base-rich mineralogies tend to have negative PC 1 scores and positive PC 2 scores (carbonatic, gypsic, mixed, and smectitic). C) Most categories plot at negative values on PC 3, whereas some soils with mixed and smectitic mineralogies plot at extreme positive values. D-F) Soils with measured carbonate content are shown on PC biplots. Note that nearly all calcareous soils plot at negative PC 1, positive PC 2 and positive PC 3 scores, suggesting that alkalinity is one of the fundamental drivers of the geochemical variance in the data set. G-I) Soils with soluble salts observed are shown in red. Note the similarity with the occurrence of carbonate.

1, positive scores on PC 2, and tend to increase in carbonate content with decreasing PC 3

scores. These findings are consistent with the pH loading vector, which increases with

negative values on PCs 1 and 3, and increases with positive values on PC 2 (Fig. 3.3.). The distribution of soils that contain soluble salts mirrors that of the soils known to be calcareous. While the presence of salts alone is not indicative of alkaline pH (Brady and Weil, 2008), the co-occurrence of carbonate in most of the saline soils strongly suggests that the source of the salt is either from authigenic precipitation in arid environments and/or weathering of saline-alkaline parent materials. Some of the soils with negative PC 3 scores contain soluble salts, and when considered with the correlation between PC 3 scores and MAT, suggests that precipitation of Na- and K-bearing salts in soils forming under hot, arid climates may contribute to the correlation between the salinization ratio and MAT (Sheldon et al., 2002; Stinchcomb et al., 2016).

3.2. PCA Interpretations

We interpret PCs 1 and 2 to represent an integration of soil-forming processes, as revealed by analysis of soil forming factors and trends in both geochemistry and pH. Scores on PC 1 track leaching and residual enrichment (positive values), and base retention and carbonate precipitation (negative values). Scores on PC 2 are inverse, with positive values reflecting base retention and carbonate accumulation, whereas negative values reflect leaching and base loss. Both MAP and MAT contribute to sample ordering on PC 1, as revealed by their significant correlation coefficients (Table 3.1). MAP is also significantly correlated with PC 2, although MAT is not. Environmental factors that occur in conjunction with warm-wet climates include increased canopy density (tree cover) and enhanced weathering rates, which drive hydrolysis, oxidation, and desilication reactions. Soils that plot at negative PC 1 and positive PC 2 scores are dominated by carbonate and/or salt precipitation reactions in alkaline settings, which buffers base loss.

In most cases, this can be attributed to low moisture availability, for which MAP serves as a proxy, and therefore the vegetation occupying these landscapes tends to be open grasslands or shrub/scrublands. That MAP is more highly correlated than MAT with PCs 1 and 2 agrees with recent findings that water availability is a first-order control on setting soil pH values (Slessarev et al., 2016).

The larger variance on PC 1 is due in part to soils with andic properties, which are not constrained by any one type of vegetation cover and comprise some of the samples with MAP > 3000 mm. However, highly weathered Ultisols and Oxisols also contribute to the soils that plot at positive values of PCs 1 and 2 (Fig. 3.3A), and exclusion of Andisols from the data set does not alter the trends revealed by PCA. The elements associated with the Andisols, Ultisols, and Oxisols include P, Mn, Al, Fe, and Ti, and their loadings are orthogonal to the loadings of the pH vector and the base oxides. These trends match well to first-principles of soil weathering reactions (e.g., Chadwick and Chorover, 2001; Stinchcomb et al., 2016) and provide the underlying framework for predicting pH from paleosols based on bulk elemental analysis.

Scores on PC 3 are driven by the variance in *l*Na_2O and K_2O, which are highly correlated with PC 3 (Table 3.1). These correlations are necessarily independent of the processes driving scores on PCs 1 and 2. A weak but significant correlation exists between MAT and PC 3 (r = -0.26). This is evidence that some of the geochemical variance imparted by MAT is not expressed by PC 1, with which both MAT and MAP are more strongly correlated (Table 3.1). We interpret these results to signify that PC 3 is primarily tracking the correlation of *l*Na_2O and K_2O to MAT.

Comparison to Previous Analysis

The PCA results show some similarity to the partial least squares regression (PLSR) results found by Stinchcomb et al. (2016), from which the data for the current study has been extracted. Correlations between each of the axes found using PCA (PCs) and those found using PLSR ("Regressors") by Stinchcomb et al. (2016) can be found in Fig. A.1. PC 1 is very similar to Regressor 1 of Stinchcomb et al. (2016), primarily due to the fact that the first-order variance in soil geochemistry is due the broad spectrum of reactions that drive mineral weathering and result in either net base loss and residual enrichment, or base gain and calcification and/or salinization. PCs 2 and 3 capture some of the transformed weights of Regressors 2 and 3 from the PLSR analysis, but are not directly comparable due to differences in the algorithms used for each technique. PLSR differs from PCA in that both input and output matrices are transformed in PLSR to maximize predictive capacity for the output matrix and to model joint response variables. PCA does not optimize prediction of an output matrix. The inclusion of pH in the PCA of this study also differs from the approach of Stinchcomb et al. (2016), who used MAP and MAT values as dependent variables in their PLSR analysis and did not include pH as an independent variable.

Regression Analysis

Regression Analysis Results

The multivariate exploration of the data set revealed that base oxide concentrations are directly correlated with soil pH, and therefore should be useful predictors (X) in Eq. 1. Candidate residual elements (R) for Eq. 1 include the recalcitrant metals that were uncorrelated with pH (Fe_2O_3, TiO_2, and Al_2O_3). ZrO_2 was negatively

correlated with pH and was also selected as a candidate predictor. The loading vector for SiO_2 was also orthogonal to pH and was found to track soils with siliceous mineralogy. This suggests that SiO_2 may not be a useful recalcitrant element for most pedogenic settings (Chadwick et al., 1990; Oh and Richter, 2005). The loading vector for P_2O_5 was determined to be associated with andic soil properties, and like MnO, is relatively easily modified through diagenesis. These two oxides are therefore omitted from further analysis.

Regression analyses were performed by iteratively substituting base oxides and candidate recalcitrant oxides into Eq. 1. Significant results were selected based on functions that exhibited the highest r^2, lowest RMSE, and had residuals that were normally and randomly distributed. Three geochemical indices were found to show the best predictive capacity for soil pH, in which X = CaO and R = Fe_2O_3, TiO_2, and Al_2O_3, abbreviated as FeCa, TiCa, and AlCa, respectively. Formulas for the indices are presented in Table 3.2, regression statistics are presented in Table 3.3, and regression plots are shown in Fig. 3.8. FeCa and TiCa predict pH using oxide weight percent, whereas the correlation between AlCa and pH is improved using oxide moles (Retallack, 2001). Addition of other predictors in weathering indices, such as Na_2O or MgO (namely, CIA-K or CALMAG), resulted in significant regression statistics; however, r^2 was lower and RMSE was higher compared to the regressions using FeCa, TiCa, and AlCa.

Cross-Validation.

A cross-validation was performed on the FeCa, TiCa, and AlCa regression models using the hat matrix method of the leave-one-out technique (Seber and Lee, 2003); see Appendix for methods). The prediction r^2, root mean square prediction error (RMSPE)

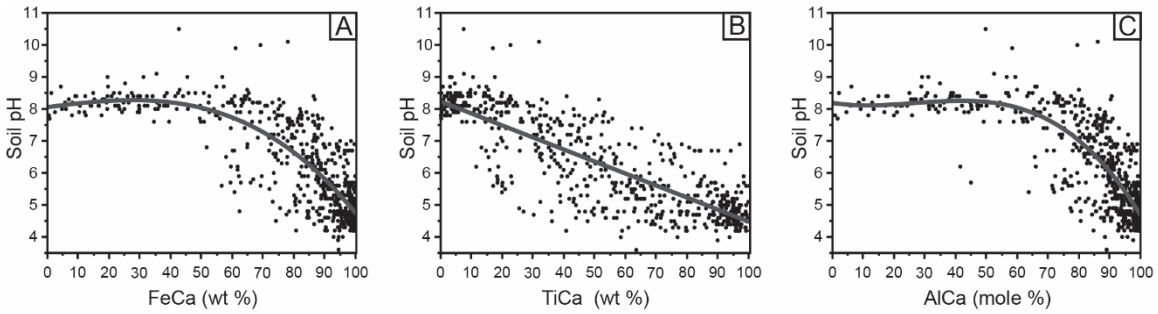

Figure 3.8. Relationships between soil pH and three weathering indices—FeCa, TiCa and AlCa. See Table 3.2 for index formulae and regression equations. See Table 3.3 for model fitness.

Table 3.2. Pedotransfer function equations.

Name	Index Formula	Pedotransfer Function
FeCa	$Fe_2O_3 / (Fe_2O_3 + CaO) \times 100$	$pH = 12.170835 - 6.92662 \times 10^{-2} \times FeCa - 9.826 \times 10^{-4} \times (FeCa-77.8066)^2 - 3.8936 \times 10^{-6} \times (FeCa-77.8066)^3$
TiCa	$TiO_2 / (TiO_2 + CaO) \times 100$	$pH = 8.2383387 - 0.037713 \times TiCa$
AlCa	$Al_2O_3 / (Al_2O_3 + CaO) \times 100$	$pH = 13.831949 - 0.0851153 \times AlCa - 1.6752 \times 10^{-3} \times (AlCa-81.6439)^2 - 1.0146 \times 10^{-5} \times (AlCa-81.6439)^3$

Note. Oxide concentrations are input as weight percent in the FeCa and TiCa functions; molar percent are input in the AlCa function. Coefficients in each function should not be rounded to prevent deviations from modelled curves.

and predicted residual error sum of squares (PRESS) statistic (Table 3.3) were used for weighing the relative fitness of each model. For each function, the r^2 and RMSPE were similar to those reported by regression results, indicating that the regression models are valid. The PRESS statistic is lowest for FeCa and highest for TiCa. Thus, pH predictions may prove more reliable from the FeCa and AlCa models than for TiCa, though all three functions should provide similar pH predictions.

Caveats for Pedotransfer Function Applications

The pedotransfer functions for pH are applicable for the uppermost B horizon of paleosols falling within the bounds of the data set (Fig. 3.2, see data repository).

Table 3.3. Pedotransfer function model fitness.

Model	Regression r^2	RMSE	Prediction r^2	RMSPE	PRESS
FeCa	0.68	0.82	0.68	0.82	422.41
TiCa	0.68	0.83	0.66	0.86	455.08
AlCa	0.67	0.84	0.67	0.84	442.81

Note. RMSE = root mean square error; RMSPE = root mean square prediction error; PRESS = predicted residual error sum of squares.

Transformation of oxide concentrations into geochemical indices (Eq. 1) should compensate for extreme concentrations of predictor oxides (i.e., CaO) by trending toward 0 or 100. However, paleosols with parent materials containing excessive Fe, Ti, or Al may skew results to lower pH by diluting the contribution of CaO, thereby underestimating pH. FeCa, TiCa, or AlCa results therefore should be cross-referenced in applications. All decimal places for each factor in the regression models should be included when calculating pH to prevent erroneous prediction (Table 3.2), which can occur particularly at low AlCa values. Paleosols bearing evidence of diagenetic alteration that possibly affected the concentrations of Ca, Al, Fe, or Ti should be omitted from proxy application. Such processes include diagenetic precipitation or dissolution of carbonates, diagenetic remobilization of Fe-oxides, or significant transmission of groundwater through coarse-grained paleosols. These functions should not be applied to Gelisols, organic soils (Histosols), or soils formed on sediments with free acids, such as pyritic marine muds, because sulfide dissolution lowers pH to ~2-3 (Thomas, 1996), below the lower limit of the data set. Likewise, soils with evidence of extreme sodicity (e.g., columnar peds) may have had pH above the upper prediction limit of the proxies.

Differentiating Soil pH and Climate

Soil pH is a measure of solution chemistry, and therefore should be influenced by the presence, amount, or timing of moisture and temperature fluxes through soil profiles. Indeed, a recent global survey of soil pH values found a significant relationship between the pH of soils and moisture balance, expressed as potential evapotranspiration (Slesserev et al., 2016). To explore the relationship between climate parameters (MAP and MAT), soil pH, and a number of geochemical weathering indices, we again applied PCA using the same methodology as above (Fig. 3.9). A strong, negative correlation exists between soil pH and CIA-K, CALMAG, FeCa, TiCa, and AlCa. These five weathering indices all increase in value with progressive base loss, which translates to less acid neutralizing capacity and lower pH (Chadwick and Chorover, 2001). The paleosol weathering index (PWI) was developed as a MAT proxy for forested Inceptisols, Alfisols, and Ultisols (Gallagher and Sheldon, 2013):

$$PWI = 100 \times [(4.20 \times Na_2O) + (1.66 \times MgO) + (5.54 \times K_2O) + (2.05 \times CaO)], \quad (2)$$

where the coefficients are calculated as relative molar abundances normalized to the sum of relative bond strengths and percent ionic character for each cation bonded with oxygen. Note that the PWI equation yields decreasing values for progressive base loss, which is the opposite trend of the other weathering indices. In this study, PWI is essentially uncorrelated with MAT and MAP, but is positively correlated with pH. The NaK index, also referred to as the salinization ratio (Sheldon et al., 2002), was developed as a MAT proxy, where:

$$NaK = \frac{Na_2O + K_2O}{Al_2O_3} \quad (3)$$

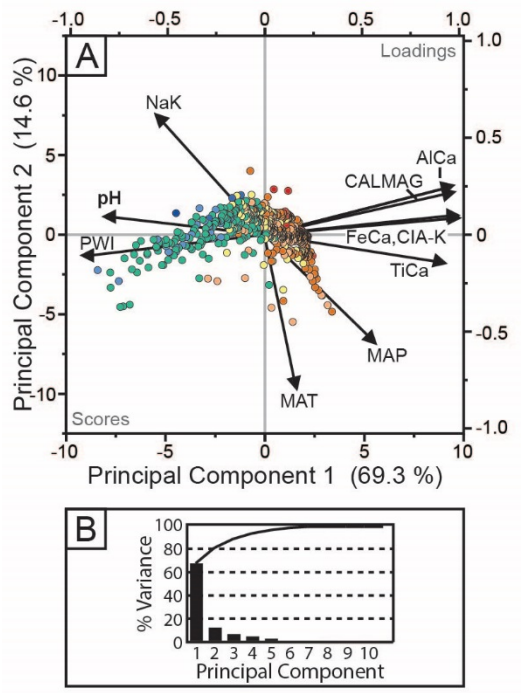

Figure 3.9. Principal components analysis on pH, geochemical indices, and the climate variables MAP and MAT. A) Color coding indicates pH value, as in Fig. 3.3. Increases in pH are strongly and inversely correlated with most weathering indices, with the exception of PWI, which increases with progressive base loss (opposite other indices), and NaK, which is positively correlated with pH but with less significance. The value of weathering indices for each sample tracks soil pH more closely than MAP, and only NaK closely tracks MAT. B) Proportion of the variance in the data set explained by each PC. Nearly all the variance is explained by PC 1, with minimal variance explained by PCs 3-10.

In this data set, NaK shows a strong negative correlation with MAP and MAT, and a significant but less strong correlation with soil pH. With the exception of NaK, all weathering indices show more robust correlations with soil pH than climate parameters. Soil pH shows a moderate, negative correlation with MAP and a weak, negative correlation with MAT.

Cross-plots of pH vs. MAP demonstrate that the relationship is functionally controlled by samples in climates that receive less than ca. 1500 mm MAP (Fig. 3.10). This cutoff has been shown elsewhere to be the approximate upper limit of MAP prediction using weathering indices that fundamentally rely on Ca to Al ratios (Sheldon

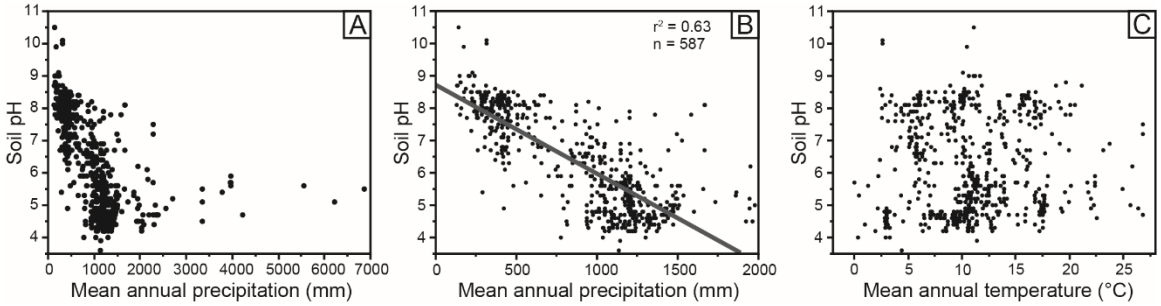

Figure 3.10. Relationship between soil pH and climate variables. A) Most data points have MAP values less than 2000 mm, above which no trend with respect to pH is evident. B) A significant negative correlation exists between pH and MAP below 2000 mm, with the majority of the relationship driven by samples below 1500 mm MAP. C) No significant relationship exists between pH and MAT.

et al., 2002; Nordt and Driese, 2010b). This finding also indicates that prediction of higher MAP values using soil bulk chemistry must use other methods, such as larger arrays of oxides in multivariate space (Stinchcomb et al., 2016) or mineralogical transformations (Hyland et al., 2015). There is no statistically significant relationship between pH and MAT using simple regression (Fig. 3.10). Collectively, we take these results to signify two important findings: 1) with the exception of NaK, the underlying variable that weathering indices track is soil pH, and 2) soil pH is influenced by climate, particularly MAP.

We can, however, examine the correlation between the weathering indices and pH independent of MAP or MAT using partial correlation analysis. Partial correlation calculates Pearson's correlation coefficient between two variables (x and y) while controlling for a third variable (z) (e.g., Rahbek and Graves, 2001; Peters, 2005). This is accomplished by first calculating the residuals of the relationship between x and z, and y and z. Because the residuals are uncorrelated with z in both cases, the calculated correlation between the residuals of the two functions are used as a measure of correlation of x and y, independent of the controlled variable (z). Partial correlation

analyses were performed in *R* statistical software (R Core Team, 2016) using the *pcor* function of the *ppcor* package (Kim, 2015).

Standard and partial correlation coefficients between pH and weathering indices and climate variables are presented in Table 3.4. For each partial correlation test, the input variable (x) was tested against pH (y) by controlling for either MAP or MAT (z) separately. Controlling for MAP resulted in a slight reduction of correlation between each weathering index and pH. The relationship between pH and MAT becomes significant at the 95% confidence level when MAP is constrained. Controlling for MAT resulted in essentially no effect on any of the correlations. It is important to note that the correlation coefficients are not regression coefficients, which depend on the type of regression model used. Most of the relationships between pH and weathering indices are nonlinear, therefore the ranking of correlation coefficients in Table 3.4 should not be confounded with predictive capacity using regression analysis (see Table 3.3 for regression models). For example, the CIA-K index shows a higher correlation coefficient with pH than AlCa. However, the AlCa regression model against pH has a higher r^2 and lower RMSE than the CIA-K regression model.

It is not surprising that each of the geochemical indices has a significant correlation with pH, as each incorporates the relative stability of Ca in some form (except NaK). These results demonstrate the relationship between soil pH and geochemistry is largely independent of MAT and influenced to some degree by MAP. However, much of the variation in soil geochemistry can be explained by pH alone, which suggests that the geochemical indices commonly used to predict climate are primarily recorders of soil pH.

Table 3.4. Correlations and partial correlations with pH.

Variable tested against pH	Correlation with pH (Pearson's r)		Partial correlation with pH (Pearson's r)		Partial correlation with pH (Pearson's r)	
			MAP-controlled		MAT-controlled	
	r	*p-value*	*r*	*p-value*	*r*	*p-value*
FeCa	-0.76	<0.001	-0.67	<0.001	-0.76	<0.001
TiCa	-0.82	<0.001	-0.75	<0.001	-0.84	<0.001
AlCa	-0.66	<0.001	-0.57	<0.001	-0.66	<0.001
CIA-K	-0.69	<0.001	-0.60	<0.001	-0.70	<0.001
CALMAG	-0.68	<0.001	-0.61	<0.001	-0.68	<0.001
PWI	0.64	<0.001	0.56	<0.001	0.64	<0.001
NaK	0.48	<0.001	0.30	<0.001	0.51	<0.001
MAP	-0.57	<0.001	NA	NA	-0.59	<0.001
MAT	-0.01	0.87[a]	0.22	<0.001	NA	NA

Note. All correlations were calculated at the 95% confidence level. Correlation coefficients differ from regression coefficients, which depend on the type of regression model used. See Table 3.2 and text for definitions or formulas for each variable. [a] Not a significant correlation ($p > 0.05$).

Discussion

The three pH proxies empirically derived in this study conform to theoretical principles of soil chemistry. We hypothesized that a geochemical index containing a ratio of Ca to Al should predict pH in regression analysis, and indeed, the AlCa index confirmed our assumptions. The reasons CaO responds to pH change are twofold: 1) Ca-carbonates are the dominant authigenic mineral phase in alkaline soils, and 2) Ca^{2+} is the most abundant exchangeable base in most non-calcareous soils (Brady and Weil, 2008). Other bases are less useful pH predictors likely due to variability in parent material mineralogy and relatively lower concentrations in the exchangeable fraction. CaO concentrations were found to be directly correlated with pH, the presence of $CaCO_3$ and soluble salts, and open canopy landscapes. Al_2O_3 was correlated with mineral classes consistent with volcanic parent materials and residually-enriched, mature soils (Ultisols

and Oxisols) that have low pH. The pH interval captured by the data in this study is bounded between 3.5 and 10.5. As noted in the introduction, the Al-buffer stabilizes pH between 3-4 due to the precipitation of 1:1 clays and Al-oxyhydroxides. Further, exchangeable Al^{3+} has been shown to rapidly increase as a relative proportion of total cation exchange capacity below pH 5.5, and dominates the exchange complex below pH ca. 4.5 (Thomas and Hargrove, 1984). Thus, both mineral and exchangeable phases favor Al species of Ca at successively lower pH, and the relative abundance of Al to Ca increases accordingly.

The relationship between FeCa and pH is significant in light of recent paleoclimate proxy developments. Using largely the same data set as the current study, (Stinchcomb et al., 2016) found the concentration of Fe_2O_3 to be an important predictor of MAP. They concluded that Fe_2O_3 was one reason the paleosol-paleoclimate model can predict MAP above the ca. 1500 mm limit of the CALMAG (Nordt and Driese, 2010b) and CIA-K functions (Sheldon et al., 2002). Hyland et al. (2015) found ratios of pedogenic goethite to hematite (G/H) to be directly correlated to MAP, though the G/H index has yet to be tested in settings above ca. 1200 mm. Taken together, both the concentration and the mineral phase of Fe in soils is related to rainfall. The relative stability of goethite versus hematite is determined by both Eh and pH (Essington, 2015), which precludes interpretation of soil mineralogy using FeCa index values without constraining soil O_2 and CO_2 concentrations. However, partial correlation analysis (Table 3.4) and the second PCA (Fig. 3.9) revealed that FeCa is more strongly correlated to pH than MAP. These findings suggest that the behavior of Ca is the primary driver in the

correlation between FeCa and pH, and that Fe mineralogy is not captured by the FeCa index.

Where soil pH is above ca. 5.5 and Al is generally immobile, bulk assays of Al_2O_3 and TiO_2 have been used as recalcitrant elements in mass balance analysis of soils (Chadwick et al., 1990). In such settings, the AlCa and TiCa indices should therefore behave similarly. In fact, the TiCa index is linear with respect to pH, in contrast to the polynomial relationship between pH and the AlCa and FeCa indices (Fig. 3.8). The linearity of the TiCa pedotransfer function suggests that Ca to Ti ratios are more sensitive to change at higher pH than Ca to Al or Ca to Fe ratios. This may be due to the fact that TiO_2 is generally less abundant than Fe_2O_3 and Al_2O_3, which would allow for the detection of small changes in CaO that are otherwise drowned out by the relatively larger concentrations of Fe_2O_3 and Al_2O_3.

Application

As a proof of concept, we reconstructed the pH of a succession of middle and late Triassic paleosols from the upper Moenkopi and Chinle Formations (Prochnow et al., 2006). All of the paleosols are fine-grained and formed on alluvial plains draining the Uncompahgre Highlands of western Pangea. Paleosol descriptions and analyses are published in Prochnow et al. (2006), the primary interpretations of which are presented in Table 3.5. These include paleosol taxonomy, reconstructed climate, and vegetation cover interpreted by a combination of root trace morphology, paleobotanical remains, or through inference using inferred MAP and MAT estimations. The addition of soil pH is a step toward more nuanced interpretation of early Mesozoic Critical Zone evolution.

Although the Chinle Formation in the study area was buried by at least 2.1 km (Jackson et al., 1998; Pederson et al., 2002), limited diagenetic alteration of the paleosols is evidenced by: 1) preserved down-profile trends in elemental oxides similar to modern soil analogues; 2) the occurrence of carbonates in sampled horizons as nodular and rhizomorphous masses, similar to modern soils, and not as fracture-fills or diagenetic cements; and 3) calculated MAT values from paleosol bulk geochemistry using the NaK index (Eq. 3) closely matches MAT values calculated using the $\delta^{18}O$ of pedogenic carbonates using a pedotransfer function by (Dworkin et al., 2005), which suggests that the oxygen isotopes in carbonates were not exchanged with diagenetic fluids. Additionally, no evidence of diagenetic precipitation of Fe minerals was reported by Prochnow et al. (2006).

The paleosols include Inceptisols, Aridisols, Alfisols, and Vertisols. The Castle Valley calcic Aridisol and Moab calcic Inceptisol were interpreted to have formed under dry desert scrub (Prochnow et al., 2006) and have an average predicted B horizon pH of 8.2 using all three pedotransfer functions, consistent with the presence of nodular calcic (Bk) horizons. Similarly, the pH values for the 48 Bk horizons in the modern soil training data set range from 7.8-9.1, with a mean of 8.2.

The Ute and La Sal Vertisols have estimated pH of 7.3-8.0, similar to values predicted by the Vertisol-specific pH function of (Nordt and Driese, 2010a). The Ute and La Sal paleosols were interpreted to have formed under a subhumid climate with dry woodland to open forest vegetation (Prochnow et al., 2006). The B horizons of 15 modern subhumid Vertisols in the training data set have similar pH values (7.5-8.2).

Finally, B horizon pH of the Kokopelli dystric Inceptisol and Slickrock argillic Alfisol are estimated to be 4.9-5.5. The presence of Bg and Bt horizons and CIA-K > 80 are congruent with a humid climate and forest vegetation. The training data set contains 87 soils with Bg or Bt horizons and CIA-K values > 80, which have pH values between 4.2-8.0 with a median of 5.3. Notably, the modern soils are dominated by forested landcover.

A shift from acidic Kokopeli and Slickrock pedotypes to alkaline Moab and Castle Valley pedotypes occurred from the lower to upper Chinle Formation (Prochnow et al., 2006), which tracks a regional aridification event attributed to the collapse of the Triassic megamonsoon (Nordt et al., 2015). The correspondence between reconstructed pH and inferred vegetation suggests a linkage existed between climate, weathering state, and plant community for these selected paleosols, such that intervals with high MAP corresponded with lower pH and higher nutrient availability in soils covered by forest vegetation. As climate dried in response to warming associated with rising CO_2 in the late Triassic, landscapes transitioned to alkaline, nutrient-poor soils mantled with desert scrub vegetation. These results are in line with observations of modern soil data using PCA and demonstrate that floral biomes may, in a broad sense, be estimated using a combination of inferred pH and paleoclimate conditions.

Table 3.5. Paleosol descriptions and reconstructed pH for middle and late Triassic paleosols.

Pedotype	Taxonomy	MAP[a] (mm)	MAT[b]	Vegetation[c]	pH values[d]				Edaphic Zone
					FeCa ±0.82	TiCa ±0.86	AlCa ±0.84	CaMg[e] ±0.6	
Castle Valley	Calcic Aridisol	Semiarid	Mesic-Hyperthermic	Desert shrub/dry woodland	8.2	8.2	8.2	N.A.	Alkaline
Moab	Calcic Inceptisol	Subhumid	Thermic-Hyperthermic	Dry woodland	8.2	8.2	8.2	N.A.	Alkaline
Ute	Cambic Vertisol	Subhumid	Thermic	Transitional dry woodland/open forest	7.3	7.7	8.0	8.2	Neutral-Alkaline
La Sal	Calcic Vertisol	Subhumid	Thermic	Transitional dry woodland/open forest	7.3	7.5	7.7	8.0	Neutral-Alkaline
Kokopelli	Dystric Inceptisol	Humid	N.A.[f]	Open forest	4.9	5.2	4.9	N.A.	Acidic
Slickrock	Argillic Alfisol	Humid	N.A.	Open forest	5.1	5.5	5.2	N.A.	Acidic

Note. Paleosol descriptions, interpretations and reconstructions of climate and vegetation are reported in Prochnow et al. (2006).
a MAP = mean annual precipitation, calculated from depth to nodular carbonate (Bk) horizon (Retallack, 2005) for the Castle Valley, Moab, and La Sal pedotypes; calculated from the chemical index of alteration munus potassium (CIA-K) proxy of Sheldon et al. (2002) for all other pedotypes.
[b] MAT = mean annual temperature, calculated using the stable oxygen isotope transfer function of Dworkin et al. (2005).
[c] Vegetation type inferred using combinations of climate reconstruction, fossil root traces and comparison to fossil floras.
[d] Reported values are averages of B horizon samples. Error given as RMSPE for FeCa, TiCa and AlCa.
[e] CaMg pH is calculated from Nordt and Driese (2010a). Error is reported as RMSE.
[f] N.A. = not applicable.

Conclusions

Soil pH is a powerful variable for understanding geochemical and biological processes in Critical Zones. Until now, pH proxies applicable on paleosols were based on limited data and restricted to the Vertisol soil order. The pedotransfer functions empirically derived in this study will allow for more robust paleosol pH reconstruction in a wider variety of settings, and adds to the growing number of proxies for deep-time Critical Zone components. Future development of pH proxies for more narrow ranges of soil forming conditions may yield reduced error estimates; however, researchers seeking to stratify data to improve regression models should carefully select soils based on properties readily recognizable in paleosols. The linkage between soil geochemistry and pH is influenced by combined actions of lithosphere composition and climate conditions, and is correlated to above-ground floral communities. The correspondence between pH, paleoclimate, and inferred floral biome in a deep-time paleosol case study suggests that future climatic and environmental proxies may benefit by incorporating soil pH in model development.

Acknowledgments

We thank S. Prochnow for providing previously unpublished geochemical data. We are also grateful to D.J. Peppe, S.I. Dworkin and J.D. White, whose comments improved an earlier draft of this manuscript. This research was supported by the Baylor University Geosciences Department and College of Arts & Sciences.

APPENDIX

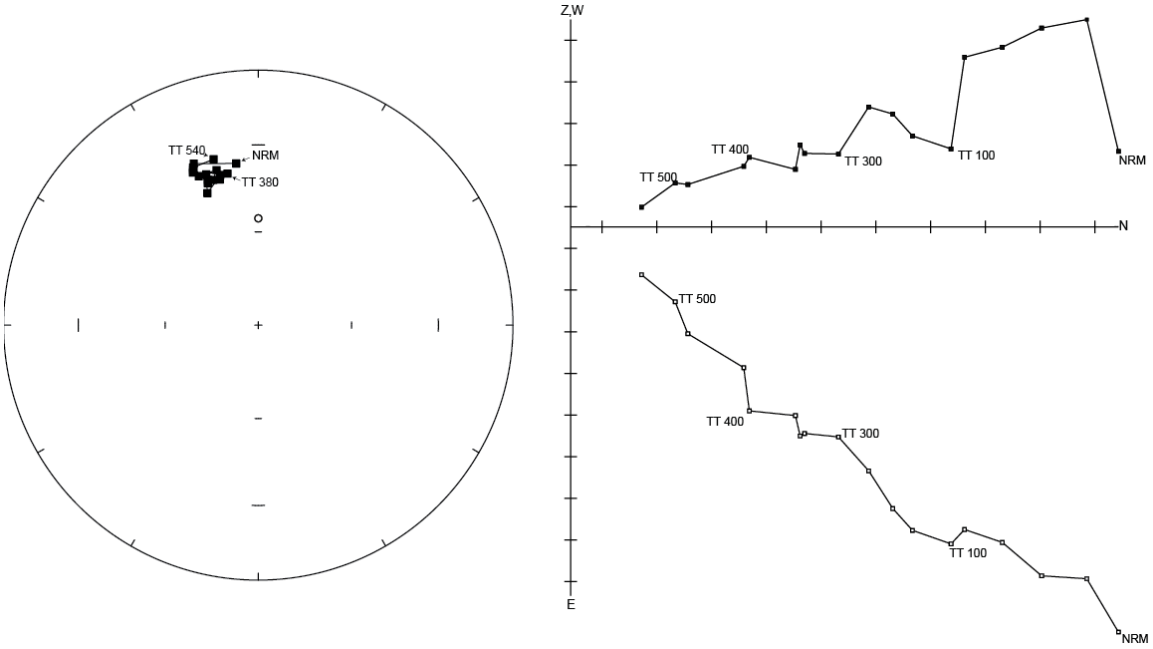

Figure A1. Equal area and vector endpoint diagram of demagnetization trajectory of a representative sample from Coffee Ranch and Mendota Ranch sections.

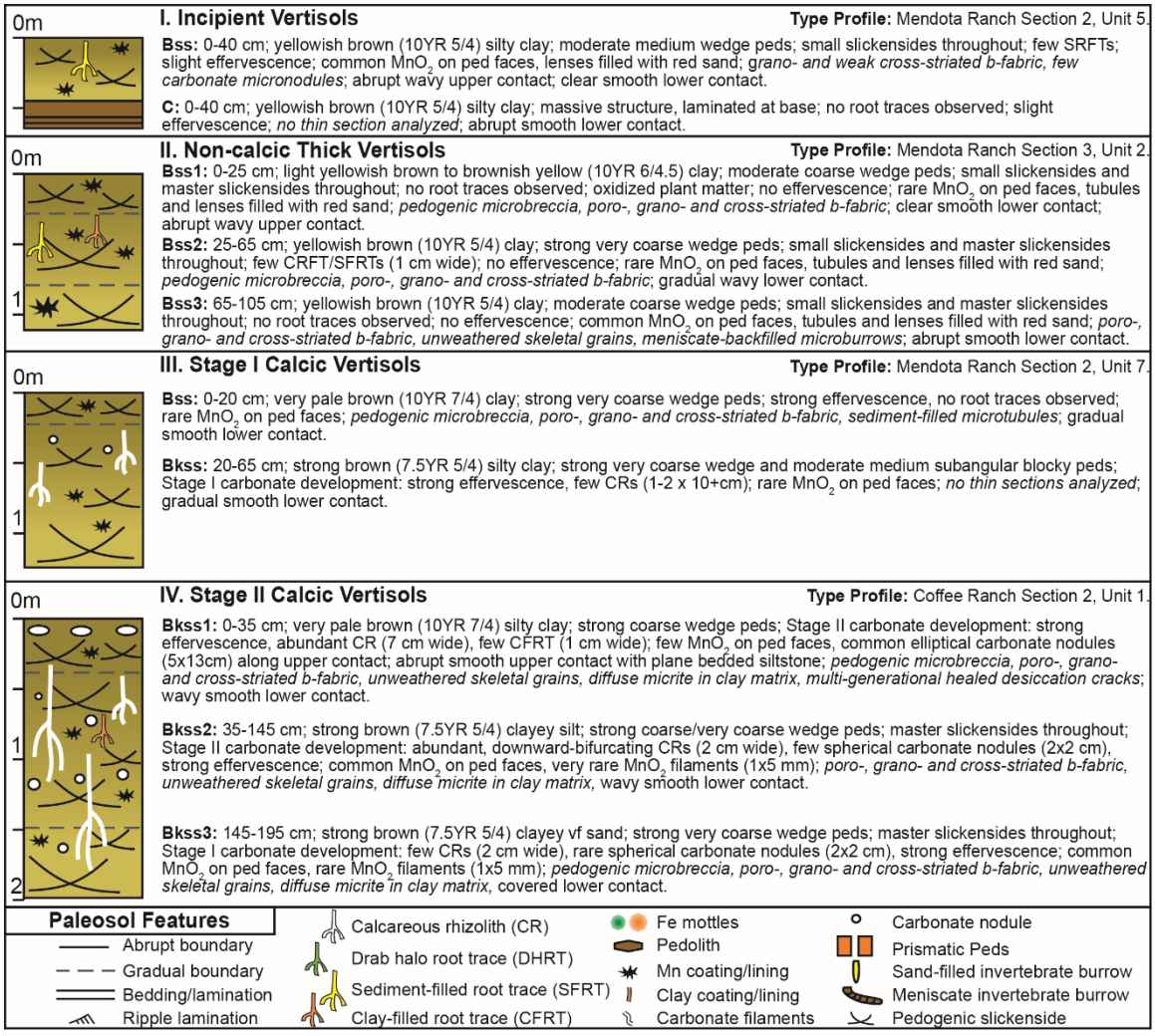

Figure A2. Clayey pedofacies described at Coffee and Mendota Ranch, Texas Panhandle.

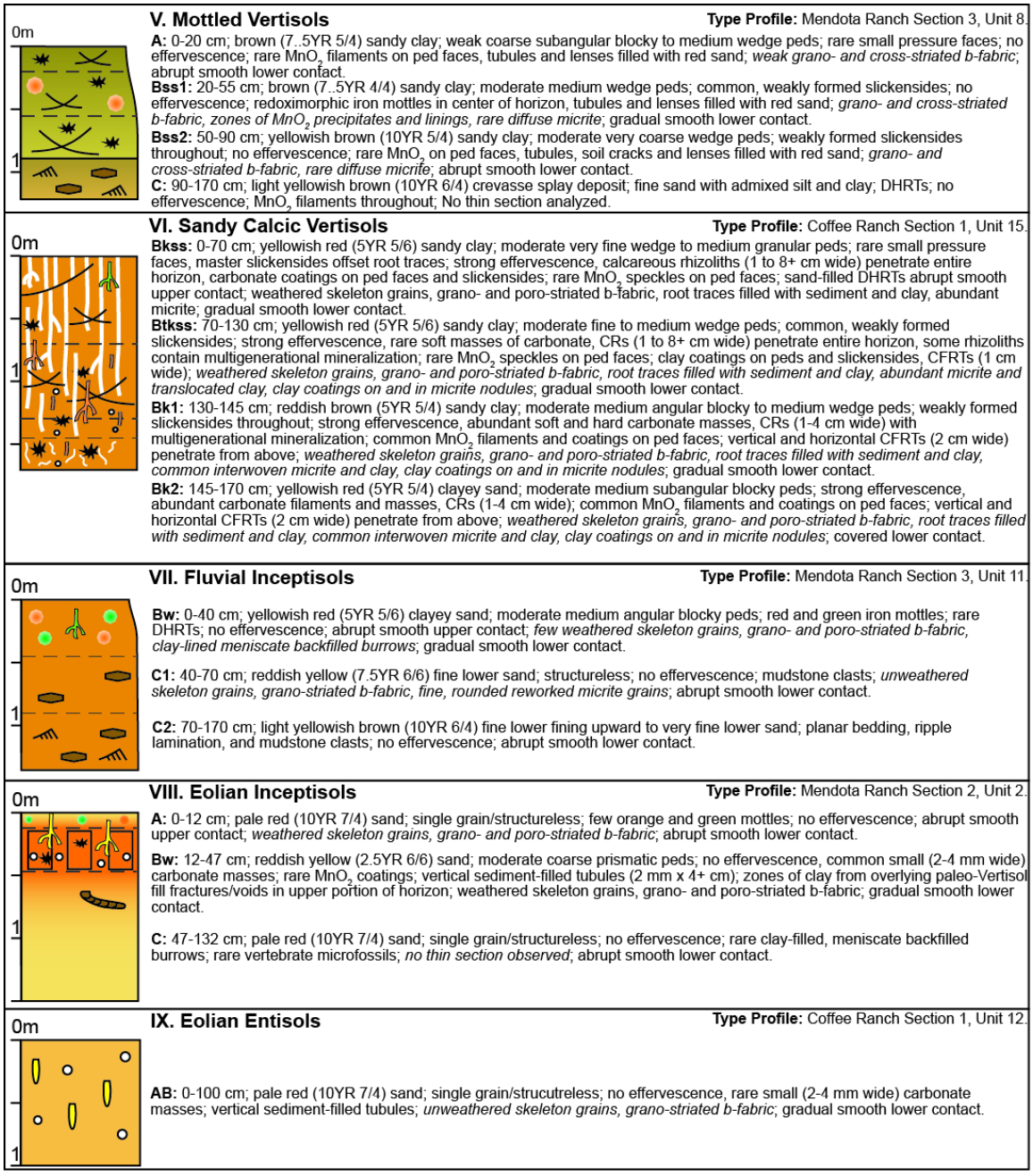

Figure A3. Sandy pedofacies described at Coffee and Mendota Ranch, Texas Panhandle.

Table A.1. Elemental geochemistry for Coffee and Mendota Ranch samples.

Profile	Horizon	Depth in horizon (cm)	Bd	Al2O3	CaO	Fe2O3	K2O	MgO	MnO	Na2O	P2O5	TiO2	ZrO2
MRS02U07	Bss	0-10	2.05	16.21	1.80	5.03	2.41	2.45	0.02	0.55	0.12	0.65	0.01
MRS02U07	Bss	10-20	2.05	16.72	1.75	5.33	2.48	2.40	0.02	0.46	0.12	0.69	0.01
MRS02U07	Bkss	0-10	2.05	16.67	1.97	5.23	2.39	2.40	0.02	0.40	0.12	0.66	0.01
MRS02U07	Bkss	10-20	2.05	17.48	1.89	5.55	2.47	2.45	0.02	0.44	0.12	0.71	0.01
MRS02U07	Bkss	20-30	2.05	16.82	1.69	5.40	2.41	2.42	0.06	0.42	0.12	0.68	0.01
MRS02U07	Bkss	30-45	2.05	17.44	1.65	5.52	2.42	2.54	0.05	0.39	0.12	0.68	0.01
CRS02U01	Bkss1	0-10	2.09	13.79	2.29	4.36	2.25	3.13	0.03	0.85	0.11	0.61	0.01
CRS02U01	Bkss1	10-20	2.09	14.15	1.22	4.37	2.35	2.39	0.02	0.86	0.10	0.59	0.01
CRS02U01	Bkss1	20-35	2.09	14.44	1.12	4.45	2.41	2.37	0.02	0.89	0.10	0.61	0.01
CRS02U01	Bkss2	0-20	2.2	14.42	1.54	4.49	2.29	2.42	0.02	0.84	0.11	0.61	0.01
CRS02U01	Bkss2	20-40	2.2	13.40	0.81	4.06	2.53	1.97	0.02	0.93	0.08	0.55	0.01
CRS02U01	Bkss2	40-60	2.2	13.62	1.69	4.03	2.45	2.16	0.03	0.90	0.09	0.55	0.01
CRS02U01	Bkss2	60-80	2.2	12.56	1.82	3.69	2.31	1.97	0.02	0.86	0.08	0.50	0.01
CRS02U01	Bkss2	80-110	2.2	12.75	1.90	3.73	2.31	2.01	0.02	0.89	0.08	0.51	0.01
CRS02U01	Bkss3	0-10	2.11	12.87	1.85	3.79	2.28	2.06	0.03	0.84	0.08	0.52	0.01
CRS02U01	Bkss3	10-25	2.11	12.94	2.00	3.83	2.29	2.06	0.04	0.85	0.08	0.52	0.01
CRS02U01	Bkss3	25-40	2.11	13.11	2.07	3.95	2.34	2.09	0.04	0.82	0.09	0.53	0.01
CRS02U01	Bkss3	40-50	2.11	13.57	1.75	4.00	2.39	2.19	0.03	0.82	0.09	0.54	0.01
MRS03U02	Bss1	0-10	2.02	17.97	0.85	5.63	2.54	2.57	0.02	0.28	0.12	0.69	0.01
MRS03U02	Bss1	10-20	2.02	18.38	0.90	5.85	2.64	2.59	0.02	0.27	0.13	0.71	0.01
MRS03U02	Bss2	0-10	2.05	18.27	0.92	5.82	2.61	2.60	0.05	0.31	0.13	0.70	0.01
MRS03U02	Bss2	10-20	2.05	17.87	0.85	5.63	2.53	2.55	0.02	0.27	0.12	0.68	0.01

Table A.1. Elemental geochemistry for Coffee and Mendota Ranch samples.

Profile	Horizon	Depth in horizon (cm)	Bd	Al2O3	CaO	Fe2O3	K2O	MgO	MnO	Na2O	P2O5	TiO2	ZrO2
MRS03U02	Bss2	20-30	2.05	16.87	0.85	5.70	2.48	2.49	0.05	0.28	0.11	0.72	0.01
MRS03U02	Bss2	30-40	2.05	17.46	0.85	5.45	2.52	2.55	0.01	0.28	0.12	0.66	0.01
MRS03U02	Bss3	0-10	2.3	17.87	0.87	5.56	2.54	2.60	0.03	0.31	0.12	0.69	0.01
MRS03U02	Bss3	10-20	2.3	17.19	0.78	5.16	2.54	2.44	0.02	0.38	0.12	0.63	0.01
MRS03U02	Bss3	20-30	2.3	17.27	0.73	5.23	2.60	2.45	0.03	0.40	0.11	0.63	0.01
MRS03U02	Bss3	30-40	2.3	18.08	0.88	5.72	2.60	2.62	0.01	0.30	0.13	0.70	0.01
MRS02U01	Bss1	0-10	2.02	14.64	0.67	4.35	2.42	2.37	0.03	0.65	0.09	0.55	0.01
MRS02U01	Bss1	10-20	2.02	15.36	0.70	4.50	2.47	2.47	0.03	0.65	0.09	0.58	0.01
MRS02U01	Bss1	20-30	2.02	15.91	0.73	4.75	2.49	2.59	0.03	0.59	0.09	0.60	0.01
MRS02U01	Bss1	30-40	2.02	15.78	0.74	4.72	2.53	2.52	0.03	0.65	0.09	0.60	0.01
MRS02U01	Bss1	40-50	2.02	16.02	0.76	4.83	2.48	2.59	0.03	0.57	0.10	0.61	0.01
MRS02U01	Bss1	50-60	2.02	16.02	0.76	4.86	2.51	2.60	0.04	0.58	0.10	0.61	0.01
MRS02U01	Bss1	60-70	2.02	16.42	0.77	5.15	2.49	2.77	0.03	0.50	0.11	0.65	0.01
MRS02U01	Bss1	70-80	2.02	17.44	0.85	5.45	2.52	2.89	0.02	0.44	0.11	0.69	0.01
MRS02U01	Bss2	0-10	2.23	17.36	0.80	5.43	2.42	2.92	0.02	0.39	0.11	0.67	0.01
MRS02U01	Bss2	10-20	2.23	15.51	0.73	4.80	2.34	2.52	0.03	0.46	0.09	0.64	0.01
MRS02U01	Bss2	20-30	2.23	15.55	0.73	4.98	2.30	2.59	0.05	0.42	0.09	0.65	0.01
MRS02U01	Bss2	30-40	2.23	16.82	0.71	5.32	2.43	2.77	0.03	0.39	0.10	0.71	0.01
MRS02U01	Bss2	40-55	2.23	16.31	0.62	5.20	2.40	2.65	0.03	0.39	0.10	0.69	0.01
CRS01U15	Bkss	0-10	2.23	9.69	2.88	3.27	2.17	1.91	0.02	0.74	0.03	0.35	0.01
CRS01U15	Bkss	10-20	2.23	9.35	1.85	3.16	2.14	1.67	0.02	0.74	0.03	0.34	0.01
CRS01U15	Bkss	30-40	2.23	8.97	3.04	2.86	2.07	1.59	0.03	0.80	0.03	0.33	0.01

Table A.1. Elemental geochemistry for Coffee and Mendota Ranch samples.

Profile	Horizon	Depth in horizon (cm)	Bd	Al2O3	CaO	Fe2O3	K2O	MgO	MnO	Na2O	P2O5	TiO2	ZrO2
CRS01U15	Bkss	50-60	2.23	8.96	4.84	2.85	2.04	1.66	0.04	0.78	0.04	0.33	0.01
CRS01U15	Bkss	60-70	2.23	8.96	8.98	2.80	1.95	1.77	0.03	0.75	0.05	0.34	0.01
CRS01U15	Btkss	0-10	2.28	9.03	7.25	2.79	2.01	1.72	0.03	0.81	0.05	0.35	0.01
CRS01U15	Btkss	20-30	2.28	9.52	4.18	3.03	2.14	1.77	0.04	0.81	0.04	0.36	0.01
CRS01U15	Btkss	30-40	2.28	8.80	14.06	2.66	1.78	1.81	0.04	0.71	0.06	0.33	0.01
CRS01U15	Btkss	40-50	2.28	9.35	10.20	2.92	1.95	1.89	0.05	0.75	0.06	0.36	0.01
CRS01U15	Btkss	50-60	2.28	9.77	13.29	3.09	1.90	2.07	0.04	0.73	0.08	0.39	0.01
CRS01U15	Btkss	60-70	2.28	10.18	8.37	3.20	2.06	2.04	0.04	0.78	0.06	0.40	0.01
CRS01U15	Bk1	0-10	2.47	10.56	9.32	3.29	2.04	2.14	0.04	0.82	0.08	0.42	0.01
CRS01U15	Bk1	10-15	2.47	11.34	8.81	3.56	2.08	2.37	0.04	0.73	0.08	0.44	0.01
CRS01U15	Bk2	0-10	1.82	10.69	7.44	3.40	2.07	1.94	0.04	1.11	0.10	0.45	0.01
CRS01U15	Bk2	10-25	1.82	9.28	1.90	2.80	2.06	1.41	0.02	1.12	0.03	0.34	0.01
MRS03U10	Mud		2.02	15.68	1.50	4.96	2.28	2.59	0.02	0.63	0.11	0.64	0.01
MRS01U13	U13A		2.02	15.66	1.25	5.16	2.60	2.57	0.02	0.61	0.12	0.64	0.01
MR S03 U3-5	Mud		2.02	15.93	2.43	5.09	2.42	2.24	0.02	0.44	0.14	0.70	0.01

Note: Elemental values are in weight percent

Table A.2. Oxygen isotopic compositions of carbonates from Coffee Ranch (CR) and Mendota Ranch (MR).

Locality	Profile	Horizon	Depth in profile (cm)	Texture	Association	Phase	Notes	$\delta^{18}O$ (‰VPDB)
MR	MRS2U7	Bkss	20-30	SlC	Rhizolith	Micrite	Core of rhizolith	-5.05
MR	MRS2U7	Bkss	20-30	SlC	Rhizolith	Micrite	Core of rhizolith	-5.08
MR	MRS2U7	Bkss	20-30	SlC	Rhizolith	Micrite	Core of rhizolith	-5.11
MR	MRS2U7	Bkss	20-30	SlC	Rhizolith	Micrite	Overgrowth	-5.08
MR	MRS2U7	Bkss	20-30	SlC	Rhizolith	Micrite	Overgrowth	-5.27
MR	MRS2U7	Bkss	20-30	SlC	Rhizolith	Micrite	Overgrowth	-5.40
MR	MRS2U7	Bkss	30	SlC	Rhizolith	Micrite	Core of rhizolith	-5.17
MR	MRS2U7	Bkss	30	SlC	Rhizolith	Micrite	Core of rhizolith	-5.12
MR	MRS2U7	Bkss	30	SlC	Rhizolith	Micrite	Core of rhizolith	-5.20
MR	MRS2U7	Bkss	30	SlC	Rhizolith	Micrite	Core of rhizolith	-5.26
MR	MRS2U7	Bkss	30	SlC	Rhizolith	Micrite	Core of rhizolith	-5.34
MR	MRS2U7	Bkss	30	SlC	Rhizolith	Micrite	Core of rhizolith	-5.24
CR	CRS2U1	Bkss1	0-10	SlC	Nodule	Micrite	Large nodules along upper contact	-5.11
CR	CRS2U1	Bkss1	0-10	SlC	Nodule	Micrite	Large nodules along upper contact	-5.12
CR	CRS2U1	Bkss1	0-10	SlC	Nodule	Micrite	Large nodules along upper contact	-5.16
CR	CRS2U1	Bkss1	0-35	SlC	Nodule	Micrite	NA	-4.64
CR	CRS2U1	Bkss1	0-35	SlC	Nodule	Micrite	NA	-5.00
CR	CRS2U1	Bkss1	0-35	SlC	Nodule	Micrite	NA	-5.03
CR	CRS2U1	Bkss1	0-35	SlC	Rhizolith	Micrite	NA	-4.97
CR	CRS2U1	Bkss1	0-35	SlC	Rhizolith	Micrite	NA	-4.93
CR	CRS2U1	Bkss1	0-35	SlC	Rhizolith	Micrite	NA	-4.90

Table A.2. Oxygen isotopic compositions of carbonates from Coffee Ranch (CR) and Mendota Ranch (MR).

Locality	Profile	Horizon	Depth in profile (cm)	Texture	Association	Phase	Notes	$\delta^{18}O$ (‰VPDB)
CR	CRS2U1	Bkss2	35-145	CSl	Rhizolith	Micrite	NA	-4.86
CR	CRS2U1	Bkss2	35-145	CSl	Rhizolith	Micrite	NA	-4.86
CR	CRS2U1	Bkss3	145-195	CS	Nodule	Micrite	NA	-4.77
CR	CRS2U1	Bkss3	145-195	CS	Nodule	Micrite	NA	-4.86
CR	CRS2U1	Bkss3	145-195	CS	Nodule	Micrite	NA	-4.84
CR	CRS2U1	Bkss3	145-195	CS	Rhizolith	Micrite	Massive rhizolith with admixed matrix	-4.81
CR	CRS2U1	Bkss3	145-195	CS	Rhizolith	Micrite	Massive rhizolith with admixed matrix	-4.91
CR	CRS2U1	Bkss3	145-195	CS	Rhizolith	Micrite	Massive rhizolith with admixed matrix	-4.90
CR	CRS2U1	Bkss3	145-195	CS	Rhizolith2	Micrite	Massive rhizolith with admixed matrix	-4.83
CR	CRS2U1	Bkss3	145-195	CS	Rhizolith2	Micrite	Massive rhizolith with admixed matrix	-4.93
CR	CRS2U1	Bkss3	145-195	CS	Rhizolith2	Micrite	Massive rhizolith with admixed matrix	-5.05
CR	CRS1U15	Bkss	0-70	SC	Rhizolith	Micrite	NA	-5.27
CR	CRS1U15	Bkss	0-70	SC	Rhizolith	Micrite	NA	-5.10
CR	CRS1U15	Bkss	0-70	SC	Rhizolith	Micrite	NA	-5.21
CR	CRS1U15	Btkss	70-130	SC	Rhizolith	Micrite	NA	-4.89
CR	CRS1U15	Btkss	70-130	SC	Rhizolith	Micrite	NA	-4.96
CR	CRS1U15	Btkss	70-130	SC	Rhizolith	Micrite	NA	-4.84
CR	CRS1U15	Bk1	130-145	SC	Rhizolith	Micrite	NA	-4.61
CR	CRS1U15	Bk1	130-145	SC	Rhizolith	Micrite	NA	-4.65

Table A.2. Oxygen isotopic compositions of carbonates from Coffee Ranch (CR) and Mendota Ranch (MR).

Locality	Profile	Horizon	Depth in profile (cm)	Texture	Association	Phase	Notes	$\delta^{18}O$ (‰VPDB)
CR	CRS1U15	Bk2	145-170	CS	Rhizolith	Micrite	NA	-4.74
CR	CRS1U15	Bk2	145-170	CS	Rhizolith	Micrite	NA	-4.46
CR	CRS1Tufa	NA	NA	Massive	Matrix	Micrite	No internal structure	-4.89
CR	CRS1Tufa	NA	NA	Massive	Matrix	Micrite	No internal structure	-4.96
CR	CRS1Tufa	NA	NA	Massive	Matrix	Micrite	No internal structure	-4.79
CR	Carb2	NA	NA	Massive	Secondary overgrowth	Translucent microspar	Translucent coatings	-5.41
CR	Carb2	NA	NA	Massive	Secondary overgrowth	Translucent microspar	Translucent coatings	-5.41
CR	Carb2	NA	NA	Massive	Secondary overgrowth	Translucent microspar	Translucent coatings	-5.46
CR	Carb2	NA	NA	Massive	Matrix	Micrite	No internal structure	-5.12
CR	Carb2	NA	NA	Massive	Matrix	Micrite	No internal structure	-5.10
CR	Carb2	NA	NA	Massive	Matrix	Micrite	No internal structure	-5.17
MR	MRS1Tufa	NA	NA	Massive	Fragments	Micrite	Reworked fragments of matrix	-5.05
MR	MRS1Tufa	NA	NA	Massive	Fragments	Micrite	Reworked fragments of matrix	-5.09
MR	MRS1Tufa	NA	NA	Massive	Fragments	Micrite	Reworked fragments of matrix	-5.04
MR	MRS1Tufa	NA	NA	Massive	Matrix	Micrite	No internal structure	-5.01
MR	MRS1Tufa	NA	NA	Massive	Matrix	Micrite	No internal structure	-5.04
MR	MRS1Tufa	NA	NA	Massive	Matrix	Micrite	No internal structure	-5.00
CR	CRS1.5	NA	NA	Massive	Secondary overgrowth	Translucent microspar	Translucent coatings	-4.73

Table A.2. Oxygen isotopic compositions of carbonates from Coffee Ranch (CR) and Mendota Ranch (MR).

Locality	Profile	Horizon	Depth in profile (cm)	Texture	Association	Phase	Notes	$\delta^{18}O$ (‰VPDB)
CR	CRS1.5	NA	NA	Massive	Secondary overgrowth	Translucent microspar	Translucent coatings	-4.70
CR	CRS1.5	NA	NA	Massive	Secondary overgrowth	Translucent microspar	Translucent coatings	-4.87
CR	CRS1.5	NA	NA	Massive	Fracture-fill	Micrite	No internal structure	-4.63
CR	CRS1.5	NA	NA	Massive	Fracture-fill	Micrite	No internal structure	-4.64
CR	CRS1.5	NA	NA	Massive	Fracture-fill	Micrite	No internal structure	-4.66
CR	CRS1.5	NA	NA	Massive	Fracture-fill	Micrite	No internal structure	-4.70
CR	CRS1.5	NA	NA	Massive	Fracture-fill	Micrite	No internal structure	-4.74
CR	CRS1.5	NA	NA	Massive	Fracture-fill	Micrite	No internal structure	-4.69

Table A.3. Paleomagnetic data for each sample used in polarity determination.

Sample	Stratigraphic section	Stratigraphic position	D (°)	I (°)	MAD (°)	Pole (°N)	Pole (°E)
CRS01-3A	CRS01	9.25	344.4	38.5	3.2	70.4	328.7
CRS04-1A	CRS04	1.75	14.4	70.2	13.8	69	124.5
CRS04-2A	CRS04	2.25	8.9	20.1	12.2	63.3	260.7
CRS04-3A	CRS04	2.75	6.7	49.2	11.8	82	234.1
CRS04-4A	CRS04	3.25	353.6	66.7	9.5	75.8	83.3
CRS04-5A	CRS04	3.75	320.3	33.7	8.1	51	354.8
MRS01-2A	MRS01	14	22.6	12.3	5.3	53.9	240.1
MRS02-1A	MRS02	0.75	352	26.5	15.3	67	300.8
MRS02-2A	MRS02	2.25	332.8	36	15.8	61.4	344.2
MRS02-3A	MRS02	2.75	339.5	58.2	5.1	73.4	27.4
MRS03-01A	MRS03	-1	327.4	48.4	10.3	61.9	6.7
MRS03-02A	MRS03	-0.5	12.5	48.9	3	77.9	216.6
MRS03-03A	MRS03	0	326.1	22.6	11.1	51.1	340.9
MRS03-05A	MRS03	0.5	357.8	32.3	10.5	71.6	287.2
MRS03-06A	MRS03	1	26.3	60.7	12.4	68.8	166.4
MRS03-07A	MRS03	1.5	21.4	78.5	3	55.7	114.6
MRS03-08A	MRS03	3.25	359.4	38.8	6.2	76.1	282.8
MRS03-09A	MRS03	4	339.9	39.9	3.1	68.2	339
MRS03-10A	MRS03	4	323.5	40	5.5	55.8	358.2
MRS03-11A	MRS03	4.75	349.3	47	8.6	78.2	333.5
MRS03-12A	MRS03	5	355.3	49.6	4.2	83.3	318.1
MRS03-13A	MRS03	6	29.3	66.4	14.4	64.9	150

Note: D = geographic declination; I = geographic inclination; MAD = mean angular deviation; Pole N and E = virtual geomagnetic pole calculated for each sample

Table A.4. Mean paleomagnetic directional data from Coffee and Mendota Ranch sections.

Subset	*n*	D (°)	I (°)	k	α95	Pole (°N)	Pole (°E)	K	A95
CRS01	1	344.4	38.5	n/a	n/a	70.4	127.8	n/a	n/a
CRS04	5	354.8	50	9.73	25.8	86.2	145.8	9.4	26.3
MRS01	1	22.6	12.3	n/a	n/a	53.9	39.1	n/a	n/a
MRS02	3	342.1	40.5	20.3	28.1	70.6	139	26.2	24.6
MRS03	12	350.7	49.6	15.3	11.4	83.2	145.1	11.3	13.5
All Coffee Ranch sites	6	352.6	48	11.5	20.6	83.4	136.4	10.9	21.2
All Mendota Ranch sites	16	351.7	46	13.2	10.6	81.4	127.4	11.4	11.4
All Sites	22	351.9	46.5	13.3	8.8	81.9	129.4	11.8	9.4

Note: Abbreviations are as follows: n—number of lines or sites included in the mean; D—declination; I—inclination; k—Fisher's (1953) precision parameter; a95—radius of 95% confidence cone around mean (Fisher, 1953); pole N and E—mean of virtual geomagnetic poles calculated for site; K and A95—Fisher statistics of paleomagnetic pole.

Table A.5. Ngira unit 15 profile B (NG15B) description.

Horizon	Depth Interval (cm)	Grain size	Structure	Color	Root traces	HCl rxn	Nodules	Lower boundary	Notes
Sand-stone	0 - +18	vcs FU to fs	txb; horizontal bedding	Gley 1 7/5 GY	NA	slight	reworked cc nodules	aw	gravel lag at base; truncates underlying horizon in places
1Btk	0 - 4	clayey fs	2mabk	10 YR 5/3 (brown)	CFRTs (1 mm); CRs (1-3 mm); DHRTs	slight	cc nodules (1-2 mm)	as	thin carbonate filaments; Fe hypocoatings on detrital grains
1C	4 - 6	ms	1vcpl	7.5 YR 6/4 (lt. brown)	rare DHRTs; few CFRTs	strong	few cc nodules (1 mm)	as	cc filaments along bedding
2Btk	6 - 34	vfs - slc	2cpr/ 2mabk	7.5 YR 5/3 (brown)	few DHRTs; abudant CFRTs (1-3 mm)	slight	common cc nodules (1-5 mm)	ab	clay skins on ped faces; Mn-coated grains
2C	34 - 36	ml-fu sand	laminated	7.5 YR 5/4 (brown)	few DHRTs; abudant CFRTs (1-3 mm)	slight	few cc nodules (1-2 mm)	as	horizontal bedding; horizon pinches out laterally
3Btk	36 - 48	vfs - slc	1-2mpr/ 2mabk	7.5 YR 5/4 (brown)	few DHRTs; abudant CFRTs (1-3 mm)	strong	abundant cc nodules (1-5 mm)	gs	clay skins on ped faces; Fe-coated grains and voids; Mn coatings on peds

Table A.5. Ngira unit 15 profile B (NG15B) description.

Horizon	Depth Interval (cm)	Grain size	Structure	Color	Root traces	HCl rxn	Nodules	Lower boundary	Notes
4Bk	71 - 85	slc	2fsbk	7.5 YR 5/4 (brown)	few DHRTs; common CFRTs (1-3 mm)	strong	common cc nodules (1-5 mm)	as	NA
4C	85 - 87	fl sand	weak bedding to massive	7.5 YR 6/4 (lt. brown)	few DHRTs; common CFRTs and Fe-lined RTs (1-3 mm)	strong	NA	as, inclined	bed is inclined 9° and becomes horizontal laterally
5Bw	87 - 93	clayey vfs	1-2 vfabk	7.5 YR 5/4 (brown)	few DHRTs	none	rare, isolated cc masses (<4 mm)	as, inclined	NA
5C	93 - 94	fl sand	weak bedding to massive	7.5 YR 6/4 (lt. brown)	few DHRTs; common CFRTs and Fe-lined RTs (1-3 mm)	strong	NA	as, inclined	bed is inclined 9° and becomes horizontal laterally
6Bw	94 - 112	clayey fs	2vfabk	7.5 YR 5/4 (brown)	few DHRTs, some with 2 mm wide cc core	slight	NA	as, inclined	NA
6C	112 - 116	fl sand	weak bedding to massive	7.5 YR 6/4 (lt. brown)	few DHRTs; common CFRTs and Fe-lined RTs (1-3 mm)	strong	NA	covered	NA

Note*:* Abbreviations are as follows. txb = trough cross-bedding. Structure: pedality = 1 (poor), 2 (moderate), 3 (strong); size = vf (very fine), f (fine), m (medium), c (coarse), vc (very coarse); ped type = abk (angular blocky), sbk (subangular blocky), pl (platy), pr (prismatic), w (wedge). Root traces: CRFT (clay-filled root trace), DHRT (drab halo root trace). Nodules: cc = calcium carbonate. Lower boundary: a (abrupt), g (gradual) w (wavy), s (smooth), b (broken).

Table A.6. Ngira unit 15 profile B (NG15B) bulk carbon analyses.

Horizon	Depth	Total C	Organic C	Inoranic C
1Btk	0	2.22	0.06	2.16
1BC	-5	5.49	0.06	5.43
2Btk	-10	2.28	0.03	2.25
2Btk	-20	2.00	0.04	1.96
2Btk w/sand lenses	-35	3.81	0.03	3.78
3Btk	-40	6.41	0.03	6.38
2BC	-60	6.37	0.08	6.29
3Bw	-75	2.71	0.03	2.68
3C	-86	5.90	0.04	5.86
4Bw	-90	2.69	0.04	2.65
4Bw	-100	1.96	0.03	1.93

Note: Reported values are in weight percent. Depth is in cm.

Table A.7. Ngira unit 15 profile B (NG15B) elemental geochemistry for untreated samples.

Horizon	Depth	Na2O	MgO	Al2O3	SiO2	K2O	CaO	TiO2	Fe2O3	P2O5	ZrO2	MnO	LOI
1Btk	0	1.23	2.96	10.20	40.20	4.14	9.03	2.34	11.55	0.55	0.04	0.35	15.50
1BC	-5	0.94	1.72	6.40	25.70	2.61	26.70	1.61	7.24	0.42	0.03	0.42	25.00
2Btk	-10	1.08	3.37	10.20	41.20	4.66	8.18	2.32	11.85	0.56	0.05	0.18	14.95
2Btk	-20	1.14	3.13	10.15	40.70	4.69	8.66	2.32	11.75	0.56	0.05	0.16	15.40
2Btk w/sand lenses	-35	0.94	2.59	9.00	35.60	4.12	15.15	2.04	10.30	0.57	0.05	0.19	18.90
3Btk	-40	0.80	3.00	7.78	30.70	3.47	18.90	1.77	8.85	0.56	0.04	0.31	22.20
2BC	-60	0.84	2.33	5.70	22.90	2.46	28.00	1.31	6.70	0.43	0.03	0.37	28.90
3Bw	-75	1.17	3.00	9.19	37.40	3.84	12.20	2.18	10.45	0.77	0.05	0.23	28.30
3C	-86	0.78	1.75	5.48	22.40	2.30	30.50	1.30	6.24	0.47	0.03	0.27	28.40
4Bw	-90	1.24	2.76	9.92	39.90	4.21	10.35	2.35	11.20	0.78	0.05	0.23	16.45
4Bw	-100	1.35	2.59	10.20	42.90	4.02	8.84	2.37	11.10	0.89	0.05	0.17	14.45

Note: All elemental values are in weight percent. Depth is in cm.

Table A.8. Ngira unit 15 profile B (NG15B) elemental geochemistry for decarbonated (treated) samples.

Horizon	Depth	Na2O	MgO	Al2O3	SiO2	K2O	CaO	TiO2	Fe2O3	P2O5	ZrO2	MnO
1Btk	0	1.07	2.38	11.54	51.05	4.81	1.03	3.03	13.13	0.17	0.05	0.11
1BC	-5	1.45	2.40	12.20	53.15	5.14	0.95	3.34	13.36	0.17	0.05	0.25
2Btk	-10	1.01	2.44	12.21	53.42	5.73	0.44	3.05	13.60	0.15	0.06	0.08
2Btk	-20	0.90	2.47	12.15	52.52	5.75	0.52	2.94	13.50	0.15	0.05	0.09
2Btk w/sand lenses	-35	1.06	2.54	12.28	52.48	5.76	0.74	3.03	13.69	0.18	0.06	0.09
3Btk	-40	0.92	2.57	12.33	52.48	5.77	0.55	3.10	13.91	0.16	0.06	0.10
2BC	-60	1.26	1.81	12.32	61.13	4.83	0.40	3.28	10.08	0.12	0.05	0.05
3Bw	-75	1.03	2.43	12.03	53.23	5.43	0.63	3.02	13.54	0.17	0.05	0.08
3C	-86	1.18	1.91	12.70	60.14	5.53	0.34	3.32	10.39	0.13	0.06	0.05
4Bw	-90	1.07	2.27	11.90	53.15	5.07	0.76	3.09	13.31	0.17	0.05	0.21
4Bw	-100	1.27	2.09	11.85	54.88	4.90	0.66	3.07	13.09	0.16	0.05	0.08

Note: All elemental values are in weight percent. Depth is in cm.

Table A.9. Elemental concentration of parent material values used for mass-balance calculations for Ngira unit 15 profile B (NG15B).

		Untreated			Decarbonated		
Horizon	Depth	Al2O3	TiO2	Zr	Al2O3	TiO2	Zr
Parent material average	NA	5.86	1.41	0.0227	12.40	3.31	0.05

Note: All elemental values are in weight percent.

Table A.10. Correlations with CaO for Ngira unit 15 profile B (NG15B).

Input	Untreated		Decarbonated	
	r	p	r	p
Na2O	-0.83	< 0.001	0.25	0.46
MgO	-0.84	0.001	0.42	0.2
K2O	-0.97	< 0.001	-0.42	0.19
Fe2O3	-0.99	< 0.001	0.5	0.12
SiO2	-0.99	< 0.001	-0.66	0.03
P2O5	-0.67	0.03	0.78	0.005
MnO	0.66	0.03	0.68	0.02
Al2O3	-0.99	< 0.001	-0.71	0.01
TiO2	-0.99	< 0.001	-0.12	0.72

Note: Decarbonate samples also referred to as “treated” in the text.

Table A.11. Stable isotope values for the NG15B profile.

Depth (cm)	Horizon	Phase	n	$\delta^{13}C$ (‰VPDB)		$\delta^{18}O$ (‰VPDB)	
				mean	sd	mean	sd
0	Bw	Nodules	3	-5.22	0.68	-5.98	0.42
5	BC	Nodules	3	-5.62	0.59	-4.62	0.28
35	2Btk (sand lens)	Dark grey hard nodules	3	-7.28	0.14	-5.02	0.09
40	2Btk (matrix)	Nodules	3	-5.31	0.10	-5.11	0.05
75	3Bw	Nodules and rhizos	3	-5.66	0.62	-7.03	0.29
90	4Bw	Fine rhizos (< 3mm)	3	-2.58	0.28	-8.05	0.17
90	4Bw	Hard nodules	3	-3.80	0.32	-6.74	0.22
90	4Bw	Hard nodules	3	-5.70	0.27	-7.66	0.01
90	4Bw	Fine rhizos (< 3mm)	3	-1.90	0.16	-7.49	0.13
100	5Bw	Rhizoliths	3	-3.23	0.18	-5.35	0.68
100	5Bw	Nodules	3	-4.93	2.90	-7.40	0.38

BIBLIOGRAPHY

Aciego Pietri, J.C., and Brookes, P.C., 2008, Relationships between soil pH and microbial properties in a UK arable soil: Soil Biology and Biochemistry, v. 40, no. 7, p. 1856–1861, doi: 10.1016/j.soilbio.2008.03.020.

Andrews, C. W. (1911). On a new species of Dinotherium (Dinotherium hobleyi) from British East Africa, in Proceedings of the Zoological Society of London (Wiley Online Library), 943–945.

Andrews, P. (1974). Report on the Karungu 1973 Expedition. Kenya National Museum, Nairobi.

Andrews, P. (1978). *A revision of the Miocene Hominoidea of East Africa*. British Museum (Natural History).

Andrews, P., Lord, J. M., and Nesbitt Evans, E. A. (1979). Patterns of ecological diversity in fossil and modern mammalian faunas. *Biol. J. Linn. Soc.* 11, 177–205.

Andrews, P., and Van Couvering, J. A. (1975). "Palaeoenvironments in the East African Miocene," in *in Szalay: Approaches to primate paleobiology*, 62–103.

Begun, D. R. (2015). "Fossil record of Miocene hominoids," in *Handbook of paleoanthropology* (Springer Berlin Heidelberg), 1261–1332.

Bestland, E. A., and Krull, E. S. (1999). Palaeoenvironments of Early Miocene Kisingiri volcano Proconsul sites: evidence from carbon isotopes, palaeosols and hydromagmatic deposits. *J. Geol. Soc.* 156, 965–976.

Bestland, E. A., Thackray, G. D., and Retallack, G. J. (1995). Cycles of doming and eruption of the Miocene Kisingiri Volcano, Southwest Kenya. *J. Geol.* 103, 598–607.

Beverly, E.J., Driese, S.G., Peppe, D.J., Johnson, C.R., Michel, L.A., Faith, J.T., Tryon, C.A., and Sharp, W.D., 2015, Recurrent spring-fed rivers in a Middle to Late Pleistocene semi-arid grassland: Implications for environments of early humans in the Lake Victoria Basin, Kenya: Sedimentology, v. 62, p. 1611–1635.

Beyrouty, C.A., Keino, J.K., Gbur, E.E., and Hanson, M.G., 2000, Phytotoxic concentrations of subsoil aluminum as influenced by soils and landscape position: Soil science, v. 165, no. 2, p. 135–143.

Birkeland, P.W., 1999, Soils and Geomorphology: Oxford University Press, 430 p.

Boellstorff, J., 1976, The succession of late Cenozoic volcanic ashes in the Great Plains: a progress report: Kansas Geological Survey Guidebook, v. 1, p. 37–71.

Bond, W. J., and Keeley, J. E. (2005). Fire as a global "herbivore": the ecology and evolution of flammable ecosystems. *Trends Ecol. Evol.* 20, 387–394.

Bonnefille, R., 2010, Cenozoic vegetation, climate changes and hominid evolution in tropical Africa: Global and Planetary Change, v. 72, p. 390–411, doi: 10.1016/j.gloplacha.2010.01.015.

Borůvka, L., Mládková, L., Penížek, V., Drábek, O., and Vašát, R., 2007, Forest soil acidification assessment using principal component analysis and geostatistics: Geoderma, v. 140, no. 4, p. 374–382, doi: 10.1016/j.geoderma.2007.04.018.

Borůvka, L., Vacek, O., and Jehlička, J., 2005, Principal component analysis as a tool to indicate the origin of potentially toxic elements in soils: Geoderma, v. 128, no. 3–4, p. 289–300, doi: 10.1016/j.geoderma.2005.04.010.

Bowen, G.J., and Revenaugh, J., 2003, Interpolating the isotopic composition of modern meteoric precipitation: Water Resources Research, v. 39.

Bowen, G.J., Wassenaar, L.I., and Hobson, K.A., 2005, Global application of stable hydrogen and oxygen isotopes to wildlife forensics: Oecologia, v. 143, p. 337–348.

Bown, T.M., and Kraus, M.J., 1987, Integration of channel and floodplain suites, I. Developmental sequence and lateral relations of alluvial paleosols: Journal of Sedimentary Petrology, v. 57, no. 4, p. 587-601.

Bradshaw, C.D., Lunt, D.J., Flecker, R., and Davies-Barnard, T., 2015, Disentangling the roles of late Miocene palaeogeography and vegetation – Implications for climate sensitivity: Palaeogeography, Palaeoclimatology, Palaeoecology, v. 417, p. 17–34.

Bradshaw, C.D., Lunt, D.J., Flecker, R., Salzmann, U., Pound, M.J., Haywood, A.M., and Eronen, J.T., 2012, The relative roles of CO2 and palaeogeography in determining late Miocene climate: results from a terrestrial model-data comparison: Climate of the Past; Katlenburg-Lindau, v. 8, p. 1257.

Brady, N. C., and Weil, R. C. (2008). *The Nature and Properties of Soils*. 14th ed. Pearson Education, Inc.

Brantley, S. L., Goldhaber, M. B., and Ragnarsdottir, K. V. (2007). Crossing disciplines and scales to understand the critical zone. *Elements* 3, 307–314.

Breecker, D.O., Sharp, Z.D., and McFadden, L.D., 2009, Seasonal bias in the formation and stable isotopic composition of pedogenic carbonate in modern soils from central New Mexico, USA: Geological Society of America Bulletin, v. 121, p. 630–640.

Brewer, R., 1964, Fabric and Mineral Analysis of Soils: Wiley, 470 p.

Bridge, J.S., 2003, Rivers and Floodplains, 491 pp: Blackwell Publishing, Malden, Mass, 491 p.

Brimhall, G.H., and Dietrich, W.E., 1987, Constitutive mass balance relations between chemical composition, volume, density, porosity, and strain in metasomatic hydrochemical systems: results on weathering and pedogenesis: Geochimica et Cosmochimica Acta, v. 51, p. 567–587.

Brimhall, G.H., Ford, C., Bratt, J., Taylor, G., Warin, O., and others, 1991, Quantitative geochemical approach to pedogenesis: importance of parent material reduction, volumetric expansion, and eolian influx in lateritization: Geoderma, v. 51, p. 51–91.

Bullock, P., Fedoroff, N., Jungerius, A., Stoops, G., and Tursina, T., 1985, Handbook of Soil Thin Section Description: Albrighton, UK, Waine Research Publications.

Burt, R., Wilson, M.A., Mays, M.D., and Lee, C.W., 2003, Major and trace elements of selected pedons in the USA: Journal of Environmental Quality, v. 32, no. 6, p. 2109–2121.

Butynski, T. (2013a). “Family Pedetidae,” in *Mammals of Africa* (London: Bloomsbury Publishing), 618.

Butynski, T. (2013b). “Species profile: Pedetes capensis,” in *Mammals of Africa* (London: Bloomsbury Publishing), 619–624.

Cerling, T.E., 1991, Carbon dioxide in the atmosphere: evidence from Cenozoic and Mesozoic paleosls: American Journal of Science, v. 291, p. 377–400.

Cerling, T. E. (1992). Development of grasslands and savannas in East Africa during the Neogene. *Palaeogeogr. Palaeoclimatol. Palaeoecol.* 97, 241–247.

Cerling, T.E., Ehleringer, J.R., and Harris, J.M., 1998, Carbon dioxide starvation, the development of C4 ecosystems, and mammalian evolution: Philosophical Transactions of the Royal Society of London. Series B: Biological Sciences, v. 353, p. 159–171.

Cerling, T. E., Harris, J. M., MacFadden, B. J., Leakey, M. G., Quade, J., Eisenmann, V., et al. (1997). Global vegetation change through the Miocene/Pliocene boundary. *Nature* 389, 153–158.

Cerling, T. E., Wynn, J. G., Andanje, S. A., Bird, M. I., Korir, D. K., Levin, N. E., et al. (2011). Woody cover and hominin environments in the past 6 million years. *Nature* 476, 51–56.

Cerling, T. E., Quade, J., Wang, Y., and Bowman, J. R. (1989). Carbon isotopes in soils and palaeosols as ecology and palaeoecology indicators. *Nature* 341, 138–139.

Cerling, T.E., and Quade, J., 1993, Stable carbon and oxygen isotopes in soil carbonates, *in* P.K. Swart, K.C. Lohmann, J. McKenzie, S. Savin (Eds.), Climate change in continental isotopic records, American Geophysical Union, v. 78, p. 217–231.

Cerling, T.E., Wang, Y., Quade, J., and others, 1993, Expansion of C4 ecosystems as an indicator of global ecological change in the late Miocene: Nature, v. 361, p. 344–345.

Chadwick, O.A., Brimhall, G.H., and Hendricks, D.M., 1990, From a black to a gray box—a mass balance interpretation of pedogenesis: Geomorphology, v. 3, p. 369–390.

Chadwick, O.A., and Chorover, J., 2001, The chemistry of pedogenic thresholds: Geoderma, v. 100, no. 3–4, p. 321–353, doi: 10.1016/S0016-7061(01)00027-1.

Chen, S.T., Smith, S.Y., Sheldon, N.D., and Strömberg, C.A.E., 2015, Regional-scale variability in the spread of grasslands in the late Miocene: Palaeogeography, Palaeoclimatology, Palaeoecology, v. 437, p. 42–52.

Chorover, J., Kretzschmar, R., Garcia-Pichel, F., and Sparks, D.L., 2007, Soil biogeochemical processes within the critical zone: Elements, v. 3, no. 5, p. 321–326.

Clark, W. E. L. G., and Leakey, L. S. B. (1951). *The Miocene Hominoidea of East Africa*. order of the Trustees of the British Museum.

Collinson, M. E., Andrews, P., and Bamford, M. K. (2009). Taphonomy of the early Miocene flora, Hiwegi Formation, Rusinga Island, Kenya. *J. Hum. Evol.* 57, 149–162.

Conrad, J. L., Jenkins, K., Lehmann, T., Manthi, F. K., Peppe, D. J., Nightingale, S., et al. (2013). New specimens of “Crocodylus” pigotti (Crocodylidae) from Rusinga Island, Kenya, and generic reallocation of the species. *J. Vertebr. Paleontol.* 33, 629–646.

Cook, R.D., and Weisberg, S., 1982, Residuals and Influence in Regression: Chapman & Hall, 248 p.

Cotton, J.M., Cerling, T.E., Hoppe, K.A., Mosier, T.M., and Still, C.J., 2016, Climate, CO_2, and the history of North American grasses since the Last Glacial Maximum: Science advances, v. 2, p. e1501346.

Cotton, J.M., Sheldon, N.D., and Strömberg, C.A.E., 2012, High-resolution isotopic record of C_4 photosynthesis in a Miocene grassland: Palaeogeography, Palaeoclimatology, Palaeoecology, v. 337–338, p. 88–98.

Counts, J.W., and Hasiotis, S.T., 2009, Neoichnological experiments with masked chafer beetles (Coleoptera: Scarabaeidae): Implications for backfilled continental trace fossils: Palaios, v. 24, p. 74–91.

Dalquest, W.W., 1983, Mammals of the Coffee Ranch Local Fauna, Hemphillian of Texas: Texas Memorial Museum, the University of Texas at Austin The Pearce-Sellards Series 38, 44 p.

Dalquest, W.W., 1969, Pliocene carbivores of the Coffee Ranch: University of Texas at Austin Bulletin 15, 49 p.

Dalquest, W.W., and Patrick, D.B., 1989, Small Mammals from the Early and Medial Hemphillian of Texas, with Descriptions of a New Bat and Gopher: Journal of Vertebrate Paleontology, v. 9, p. 78–88.

Davis, J.C., 1986, Statistics and data analysis in geology: John Wiley & Sons.

Delhaize, E., and Ryan, P.R., 1995, Aluminum Toxicity and Tolerance in Plants: Plant Physiology, v. 107, no. 2, p. 315–321.

Dere, A.L., White, T.S., April, R.H., Reynolds, B., Miller, T.E., Knapp, E.P., McKay, L.D., and Brantley, S.L., 2013, Climate dependence of feldspar weathering in shale soils along a latitudinal gradient: Geochimica et Cosmochimica Acta, v. 122, p. 101–126.

Devau, N., Cadre, E.L., Hinsinger, P., Jaillard, B., and Gérard, F., 2009, Soil pH controls the environmental availability of phosphorus: Experimental and mechanistic modelling approaches: Applied Geochemistry, v. 24, no. 11, p. 2163–2174, doi: 10.1016/j.apgeochem.2009.09.020.

Drake, R. E., Van Couvering, J. A., Pickford, M. H., Curtis, G. H., and Harris, J. A. (1988). New chronology for the Early Miocene mammalian faunas of Kisingiri, Western Kenya. *J. Geol. Soc.* 145, 479–491.

Driese, S.G., 2004, Pedogenic Translocation of Fe in Modern and Ancient Vertisols and Implications for Interpretations of the Hekpoort Paleosol (2.25 Ga): The Journal of Geology, v. 112, p. 543–560.

Driese, S.G., and Ashley, G.M., 2016, Paleoenvironmental reconstruction of a paleosol catena, the Zinj archeological level, Olduvai Gorge, Tanzania: Quaternary Research, v. 85, no. 1, p. 133–146.

Driese, S. G., Mora, C. I., Stiles, C. A., Joeckel, R. M., and Nordt, L. C. (2000). Mass-balance reconstruction of a modern Vertisol: implications for interpreting the geochemistry and burial alteration of paleo-Vertisols. *Geoderma* 95, 179–204.

Driese, S.G., Peppe, D.J., Beverly, E.J., DiPietro, L.M., Arellano, L.N., and Lehmann, T., 2016, Paleosols and paleoenvironments of the early Miocene deposits near Karungu, Lake Victoria, Kenya: Palaeogeography, Palaeoclimatology, Palaeoecology, v. 443, p. 167–182.

Dworkin, S.I., Nordt, L., and Atchley, S., 2005, Determining terrestrial paleotemperatures using the oxygen isotopic composition of pedogenic carbonate: Earth and Planetary Science Letters, v. 237, p. 56–68.

Easterling, D.R., Evans, J.L., Groisman, P.Y., Karl, T.R., Kunkel, K.E., and Ambenje, P., 2000, Observed variability and trends in extreme climate events: a brief review: Bulletin of the American Meteorological Society, v. 81, p. 417–425.

Edwards, E. J., Osborne, C. P., Strömberg, C. A., Smith, S. A., Consortium, C. G., and others (2010). The origins of C4 grasslands: integrating evolutionary and ecosystem science. *Science* 328, 587–591.

Ehleringer, J. R., and Cooper, T. A. (1988). Correlations between Carbon Isotope Ratio and Microhabitat in Desert Plants. *Oecologia* 76, 562–566.

Ehleringer, J.R., Cerling, T.E., and Helliker, B.R., 1997, C4 photosynthesis, atmospheric CO2, and climate: Oecologia, v. 112, p. 285–299.

Essington, M.E., 2015, Soil and water chemistry: an integrative approach: CRC press.

Farnham, I.., Johannesson, K.., Singh, A.., Hodge, V.., and Stetzenbach, K.., 2003, Factor analytical approaches for evaluating groundwater trace element chemistry data: Analytica Chimica Acta, v. 490, no. 1–2, p. 123–138, doi: 10.1016/S0003-2670(03)00350-7.

Fisher, R., 1953, Dispersion on a sphere, *in* Proceedings of the Royal Society of London A: Mathematical, Physical and Engineering Sciences, The Royal Society, v. 217, p. 295–305.

Forbes, M. S., Bestland, E. A., Krull, E. S., and Dicker, D. G. (2004). Palaeoenvironmental mosaic of Proconsul habitats: geochemical and sedimentalogical interpretation of Kisingiri fossil sites, Western Kenya. *J. Afr. Earth Sci.* 39, 63–79.

Forman, S.L., Oglesby, R., and Webb, R.S., 2001, Temporal and spatial patterns of Holocene dune activity on the Great Plains of North America: megadroughts and climate links: Global and Planetary Change, v. 29, p. 1–29.

Fox, D.L., and Fisher, D.C., 2004, Dietary reconstruction of Miocene Gomphotherium (Mammalia, Proboscidea) from the Great Plains region, USA, based on the carbon isotope composition of tusk and molar enamel: Palaeogeography, Palaeoclimatology, Palaeoecology, v. 206, p. 311–335.

Fox, D.L., Honey, J.G., Martin, R.A., and Peláez-Campomanes, P., 2012, Pedogenic carbonate stable isotope record of environmental change during the Neogene in the southern Great Plains, southwest Kansas, USA: carbon isotopes and the evolution of C4-dominated grasslands: Geological Society of America Bulletin, v. 124, p. 444–462.

Fox, D.L., and Koch, P.L., 2003, Tertiary history of C_4 biomass in the Great Plains, USA: Geology, v. 31, p. 809–812.

Fox, D.L., and Koch, P.L., 2004, Carbon and oxygen isotopic variability in Neogene paleosol carbonates: constraints on the evolution of the C_4-grasslands of the Great Plains, USA: Palaeogeography, Palaeoclimatology, Palaeoecology, v. 207, p. 305–329.

Fraser, D., and Theodor, J.M., 2013, Ungulate diets reveal patterns of grassland evolution in North America: Palaeogeography, Palaeoclimatology, Palaeoecology, v. 369, p. 409–421.

Fricke, H.C., and O'Neil, J.R., 1999, The correlation between $^{18}O/^{16}O$ ratios of meteoric water and surface temperature: its use in investigating terrestrial climate change over geologic time: Earth and Planetary Science Letters, v. 170, p. 181–196.

Friedman, I., and O'Neil, J.R., 1977, Data of geochemistry: Compilation of stable isotope fractionation factors of geochemical interest: US Government Printing Office, v. 440, 12 p.

Gallagher, T. M., and Sheldon, N. D. (2013). A new paleothermometer for forest paleosols and its implications for Cenozoic climate. *Geology* 41, 647–650. doi:10.1130/G34074.1.

Gat, J.R., 1996, Oxygen and hydrogen isotopes in the hydrologic cycle: Annual Review of Earth and Planetary Sciences, v. 24, p. 225–262.

Ge, D., Wen, Z., Xia, L., Zhang, Z., Erbajeva, M., Huang, C., et al. (2013). Evolutionary history of lagomorphs in response to global environmental change. *PLoS One* 8, e59668.

Gebo, D. L., MacLatchy, L., Kityo, R., Deino, A., Kingston, J., and Pilbeam, D. (1997). A hominoid genus from the early Miocene of Uganda. *Science* 276, 401–404.

Geraads, D., Lehmann, T., Peppe, D. J., and McNulty, K. P. (2016). New Rhinocerotidae from the Kisingiri localities (lower Miocene of western Kenya). *J. Vertebr. Paleontol.* 36, e1103247.

Gile, L.H., Peterson, F.F., and Grossman, R.B., 1966, Morphological and genetic sequences of carbonate accumulation in desert soils: Soil Science, v. 101, p. 347–360.

Groisman, P.Y., Karl, T.R., Easterling, D.R., Knight, R.W., Jamason, P.F., Hennessy, K.J., Suppiah, R., Page, C.M., Wibig, J., Fortuniak, K., and others, 1999, Changes in the probability of heavy precipitation: important indicators of climatic change, *in* Weather and Climate Extremes, Springer, p. 243–283.

Gurdak, J.J., and Roe, C.D., 2009, Recharge rates and chemistry beneath playas of the High Plains aquifer-A literature review and synthesis: US Geological Survey Circular 1333, 1333, 39 p.

Gustavson, T.C., 1986, Geomorphic development of the Canadian River Valley, Texas Panhandle: an example of regional salt dissolution and subsidence: Geological Society of America Bulletin, v. 97, p. 459–472.

Gustavson, T.C., 1996, Fluvial and eolian depositional systems, paleosols, and paleoclimate of the upper Cenozoic Ogallala and Blackwater Draw formations, southern High Plains, Texas and New Mexico: Bureau of Economic Geology, The University of Texas at Austin, v. 239, 62 p.

Gustavson, T.C., Holliday, V.T., and Hovorka, S.D., 1995, Origin and development of playa basins, sources of recharge to the Ogallala aquifer, Southern High Plains, Texas and New Mexico: Bureau of Economic Geology Report of Investigations 229, 44 p.

Gustavson, T.C., and Winkler, D.A., 1988, Depositional facies of the Miocene-Pliocene Ogallala Formation, northwestern Texas and eastern New Mexico: Geology, v. 16, p. 203–206.

Happold, D. C. D. (2013a). “Family Thryonomyidae,” in *Mammals of Africa* (London: Bloomsbury Publishing), 685–690.

Happold, D. C. D. (2013b). “Order Lagomorpha,” in *Mammals of Africa* (London: Bloomsbury Publishing), 693–717.

Harrison, T. (2010). Dendropithecoidea, proconsuloidea, and hominoidea. *Cenozoic Mamm. Afr. Univ. Calif. Press Berkeley*, 429–469.

Hasenmueller, E.A., Jin, L., Stinchcomb, G.E., Lin, H., Brantley, S.L., and Kaye, J.P., 2015, Topographic controls on the depth distribution of soil CO 2 in a small temperate watershed: Applied Geochemistry, v. 63, p. 58–69.

Haug, G.H., and Tiedemann, R., 1998, Effect of the formation of the Isthmus of Panama on Atlantic Ocean thermohaline circulation: Nature, v. 393, p. 673–676.

Helena, B., Pardo, R., Vega, M., Barrado, E., Fernandez, J.M., and Fernandez, L., 2000, Temporal evolution of groundwater composition in an alluvial aquifer (Pisuerga River, Spain) by principal component analysis: Water research, v. 34, no. 3, p. 807–816.

Homer, C., Dewitz, J., Fry, J., Coan, M., Hossain, N., Larson, C., Herold, N., McKerrow, A., VanDriel, J.N., Wickham, J., and others, 2007, Completion of the 2001 national land cover database for the counterminous United States: Photogrammetric Engineering and Remote Sensing, v. 73, no. 4, p. 337.

Hopwood, A. T. (1933). XI.—Miocene Primates from British East Africa. *J. Nat. Hist.* 11, 96–98.

Hyland, E.G., and Sheldon, N.D., 2013, Coupled CO2-climate response during the Early Eocene Climatic Optimum: Palaeogeography, Palaeoclimatology, Palaeoecology, v. 369, p. 125–135.

Izett, G.A., 1975, Late Cenozoic sedimentation and deformation in northern Colorado and adjoining areas: Geological Society of America Memoirs, v. 144, p. 179–210.

Jackson, M.P.A., Schultz-Ela, D.D., Hudec, M.R., Watson, I.A., and Porter, M.L., 1998, Structure and evolution of Upheaval Dome: A pinched-off salt diapir: Geological Society of America Bulletin, v. 110, no. 12, p. 1547–1573.

Jacobs, B.F., Kingston, J.D., and Jacobs, L.L., 1999, The Origin of Grass-Dominated Ecosystems: Annals of the Missouri Botanical Garden, v. 86, p. 590.

Jacobs, B. F., Pan, A. D., and Scotese, C. R. (2010). A review of the Cenozoic vegetation history of Africa. *Cenozoic Mamm. Afr. Univ. Calif. Press Berkeley*, 57–72.

Janis, C.M., Damuth, J., and Theodor, J.M., 2002, The origins and evolution of the North American grassland biome: the story from the hoofed mammals: Palaeogeography, Palaeoclimatology, Palaeoecology, v. 177, p. 183–198.

Jenny, H., 1941, Factors of soil formation: A system of quantitative pedology, New York: McGraw-Hill, 281 p.

Jenny, H., 1994, Factors of soil formation: a system of quantitative pedology: Courier Corporation, 300 p.

JMP, 2016, SAS Institute Inc., Cary, NC.

Joeckel, R.M., Wooden, S.R., Korus, J.T., and Garbisch, J.O., 2014, Architecture, heterogeneity, and origin of late Miocene fluvial deposits hosting the most important aquifer in the Great Plains, USA: Sedimentary Geology, v. 311, p. 75–95.

Kahmann, J.A., and Driese, S.G., 2008, Paleopedology and geochemistry of Late Mississippian (Chesterian) Pennington Formation paleosols at Pound Gap, Kentucky, USA: implications for high-frequency climate variations: Palaeogeography, Palaeoclimatology, Palaeoecology, v. 259, no. 4, p. 357–381.

Kämpf, N., and Schwertmann, U., 1983, Goethite and hematite in a climosequence in southern Brazil and their application in classification of kaolinitic soils: Geoderma, v. 29, no. 1, p. 27–39, doi: 10.1016/0016-7061(83)90028-9.

Karl, T.R., and Knight, R.W., 1998, Secular trends of precipitation amount, frequency, and intensity in the United States: Bulletin of the American Meteorological society, v. 79, p. 231–241.

Kay, R. F., and Ungar, P. S. (1997). “Dental evidence for diet in some Miocene catarrhines with comments on the effects of phylogeny on the interpretation of adaptation,” in *Function, Phylogeny, and Fossils* (Springer), 131–151.

Keeley, J.E., and Rundel, P.W., 2005, Fire and the Miocene expansion of C_4 grasslands: Miocene C4 grassland expansion: Ecology Letters, v. 8, p. 683–690.

Kelley, J. (1986). Species recognition and sexual dimorphism in Proconsul and Rangwapithecus. *J. Hum. Evol.* 15, 461–495.

Kelley, J. (1993). “Taxonomic implications of sexual dimorphism in Lufengpithecus,” in *Species, Species Concepts and Primate Evolution* (Springer), 429–458.

Kelley, J. (1997). “Paleobiological and phylogenetic significance of life history in Miocene hominoids,” in *Function, Phylogeny, and Fossils* (Springer), 173–208.

Kelley, J. (2002). The hominoid radiation in Asia. *Primate Foss. Rec.*

Keigwin, L., 1982, Isotopic Paleoceanography of the Caribbean and East Pacific: Role of Panama Uplift in Late Neogene Time: Science, v. 217, p. 350–353.

Kim, S., 2015, ppcor: An R Package for a Fast Calculation to Semi-partial Correlation Coefficients: Communications for Statistical Applications and Methods, v. 22, no. 6, p. 665–674.

King, B. C., Le Bas, M. J., and Sutherland, D. S. (1972). The history of the alkaline volcanoes and intrusive complexes of eastern Uganda and western Kenya. *J. Geol. Soc.* 128, 173–205.

Kingston, J. D., Marino, B. D., Hill, A., and others (1994). Isotopic evidence for Neogene hominid paleoenvironments in the Kenya Rift Valley. *Science* 264, 955–958.

Kirschvink, J.L., 1980, The least-squares line and plane and the analysis of palaeomagnetic data: Geophysical Journal International, v. 62, p. 699–718.

Kohn, M. J. (2010). Carbon isotope compositions of terrestrial C3 plants as indicators of (paleo)ecology and (paleo)climate. *Proc. Natl. Acad. Sci.* 107, 19691–19695. doi:10.1073/pnas.1004933107.

Kraus, M.J., 1987, Integration of channel and floodplain suites, II. Vertical relations of alluvial paleosols: Journal of Sedimentary Petrology, v. 57, no. 4, p. 602-612.

Kraus, M.J., 1999, Paleosols in clastic sedimentary rocks: their geologic applications: Earth-Science Reviews, v. 47, p. 41–70.

Krzanowski, W.J., 1988, Principles of multivariate analysis: a user's perspective: Clarendon Press ; Oxford University Press, Oxford [Oxfordshire]: New York.

Lauber, C.L., Hamady, M., Knight, R., and Fierer, N., 2009, Pyrosequencing-Based Assessment of Soil pH as a Predictor of Soil Bacterial Community Structure at the Continental Scale: Applied and Environmental Microbiology, v. 75, no. 15, p. 5111–5120, doi: 10.1128/AEM.00335-09.

Li, Y.-L., Peacock, A.D., White, D.C., Geyer, R., and Zhang, C.L., 2007, Spatial patterns of bacterial signature biomarkers in marine sediments of the Gulf of Mexico: Chemical Geology, v. 238, no. 3–4, p. 168–179, doi: 10.1016/j.chemgeo.2006.11.007.

Leakey, L. S. B. (1943). A Miocene anthropoid mandible from Rusinga, Kenya. *Nature* 152, 319–320.

Leakey, M., and Walker, A. (1997). "Afropithecus," in *Function, Phylogeny, and Fossils* (Springer), 225–239.

Lehmann, T., Peppe, D. J., Driese, S. G., Jenkins, K., Sanders, W. J., and McNulty, K. P. (2014). New fieldwork at Karungu (early Miocene; Lake Victoria, Kenya): preliminary paleontological and geological results. *J. Vertebr. Paleontol. Program Abstr.* 2014, A168.

Lindsay, E., Johnson, N.M., and Opdyke, N.D., 1975, Preliminary correlation of North American Land Mammal Ages and geomagnetic chronology, *in* Studies in Cenozoic Paleontology and Stratigraphy, University of Michigan Museum of Paleontology, C.W. Hibbard Memorial, p. 111–119.

Lovejoy, C. O. (2009). Reexamining human origins in light of Ardipithecus ramidus. *Science* 326, 74–74e8.

Lovejoy, C. O., Simpson, S. W., White, T. D., Asfaw, B., and Suwa, G. (2009a). Careful climbing in the Miocene: the forelimbs of Ardipithecus ramidus and humans are primitive. *Science* 326, 70–70e8.

Lovejoy, C. O., Suwa, G., Simpson, S. W., Matternes, J. H., and White, T. D. (2009b). The great divides: Ardipithecus ramidus reveals the postcrania of our last common ancestors with African apes. *Science* 326, 73–106.

Lucas, S., and Schultz, G., 2007, Miocene vertebrate footprints from the Texas Panhandle: Cenozoic Vertebrate Tracks and Traces. New Mexico Museum of Natural History and Science Bulletin, v. 42, p. 177–183.

Lyman, R. L. (2008). *Quantitative paleozoology*. Cambridge University Press.

Ma, L., Chabaux, F., Pelt, E., Blaes, E., Jin, L., and Brantley, S., 2010, Regolith production rates calculated with uranium-series isotopes at Susquehanna/Shale Hills Critical Zone Observatory: Earth and Planetary Science Letters, v. 297, no. 1, p. 211–225.

MacLatchy, L., Gebo, D., Kityo, R., and Pilbeam, D. (2000). Postcranial functional morphology of Morotopithecus bishopi, with implications for the evolution of modern ape locomotion. *J. Hum. Evol.* 39, 159–183.

MacLatchy, L., Rossie, J., Smith, T. M., and Tafforeau, P. (2010). Evidence for dietary niche separation in the Miocene hominoids Morotopithecus and Afropithecus. in *American Journal of Physical Anthropology*, 160–160.

Mandal, U.K., Warrington, D.N., Bhardwaj, A.K., Bar-Tal, A., Kautsky, L., Minz, D., and Levy, G.J., 2008, Evaluating impact of irrigation water quality on a calcareous clay soil using principal component analysis: Geoderma, v. 144, no. 1–2, p. 189–197, doi: 10.1016/j.geoderma.2007.11.014.

Matthew, W.D., and Stirton, R.A., 1930, Equidae from the Pliocene of Texas: Berkeley, CA, University of California Press, University of California publications, Bulletin of the Department of Geological Sciences, v. 19, 349-369 p.

Maxbauer, D. P., Peppe, D. J., Bamford, M., McNulty, K. P., Harcourt-Smith, W. E., and Davis, L. E. (2013). A morphotype catalog and paleoenvironmental interpretations of early Miocene fossil leaves from the Hiwegi Formation, Rusinga Island, Lake Victoria, Kenya. *Palaeontol. Electron.* 16, 19.

Maynard, J.B., 1992, Chemistry of modern soils as a guide to interpreting Precambrian paleosols: The Journal of Geology, v. 100, no. 3, p. 279–289.

McCollum, M. S., Peppe, D. J., McNulty, K. P., Dunsworth, H. M., Harcourt-Smith, W. E. H., and Andrews, A. L. (2013). Magnetostratigraphy of the early Miocene Hiwegi Formation (Rusinga Island, Lake Victoria, Kenya). in *Geological Society of America Abstracts with Programs*, 12.

McNulty, K. P. (2003). Geometric morphometric analyses of extant and fossil hominoid craniofacial morphology, Unpublished PhD. Thesis, City University of New York.

McNulty, K. P., Harcourt-Smith, W. E. H., and Dunsworth, H. M. (2007). New primate fossils from Rusinga Island, Kenya. in *American Journal of Physical Anthropology* (Wiley), 170–170.

McNulty, K. P., Begun, D. R., Kelley, J., Manthi, F. K., and Mbua, E. N. (2015). A systematic revision of Proconsul with the description of a new genus of early Miocene hominoid. *J. Hum. Evol.* 84, 42–61.

Miall, A.D., 1978, Lithofacies types and vertical profile models in braided river deposits: a summary, *in* Fluvial Sedimentology, Canadian Society of Petrolium Geology Memoirs 5, p. 597–604.

Michel, L. A., Peppe, D. J., Lutz, J. A., Driese, S. G., Dunsworth, H. M., Harcourt-Smith, W. E. H., et al. (2014). Remnants of an ancient forest provide ecological context for Early Miocene fossil apes. *Nat. Commun.* 5. doi:10.1038/ncomms4236.

Miller, R.O., and Kissel, D.E., 2010, Comparison of Soil pH Methods on Soils of North America: Soil Science Society of America Journal, v. 74, no. 1, p. 310, doi: 10.2136/sssaj2008.0047.

Moore, D. M., and Reynolds, R. C. (1997). *X-ray Diffraction and the Identification and Analysis of Clay Minerals*. Oxford university press Oxford.

Morgan, M. E., Kingston, J. D., and Marino, B. D. (1994). Carbon isotopic evidence for the emergence of C4 plants in the Neogene from Pakistan and Kenya. *Nature* 367, 162–165.

Morgan, L.A., and McIntosh, W.C., 2005, Timing and development of the Heise volcanic field, Snake River Plain, Idaho, western USA: Geological Society of America Bulletin, v. 117, p. 288–306.

Morgan, L.A., Pierce, K.L., and McIntosh, W.C., 1999, 40Ar/39Ar ages of silicic volcanic rocks in the Snake River Plain: timing of volcanism and tectonism along the track of the Yellowstone hot spot: Geological Society of America Abstracts with Program, v. 31, p. A-49.

Morley, R. J., and Richards, K. (1993). Gramineae cuticle: a key indicator of Late Cenozoic climatic change in the Niger Delta. *Rev. Palaeobot. Palynol.* 77, 119–127.

Naeser, C.W., Izett, G.A., and Obradovich, J.D., 1980, Fission-track and K-Ar ages of natural glasses: US Govt. Printing Office

Neelin, J.D., Sahany, S., Stechmann, S.N., and Bernstein, D.N., 2017, Global warming precipitation accumulation increases above the current-climate cutoff scale: Proceedings of the National Academy of Sciences, vol. 114, no. 6, p. 1258-1263.

Nesbit Evans, E., Van Couvering, J. A., and Andrews, P. (1981). Palaeoecology of Miocene sites in western Kenya. *J. Hum. Evol.* 10, 99–116.

Nesbitt, H.W., and Young, G.M., 1982, Early Proterozoic climates and plate motions inferred from major element chemistry of lutites: Nature, v. 299, no. 5885, p. 715–717.

Nordt, L., Atchley, S., and Dworkin, S., 2003, Terrestrial evidence for two greenhouse events in the latest Cretaceous: GSA today, v. 13, p. 4–9.

Nordt, L., Atchley, S., and Dworkin, S., 2015, Collapse of the Late Triassic megamonsoon in western equatorial Pangea, present-day American Southwest: Geological Society of America Bulletin, p. 1798-1815.

Nordt, L.C., and Driese, S.G., 2010a, A modern soil characterization approach to reconstructing physical and chemical properties of paleo-Vertisols: American Journal of Science, v. 310, no. 1, p. 37–64.

Nordt, L.C., and Driese, S.G., 2010, New weathering index improves paleorainfall estimates from Vertisols: Geology, v. 38, p. 407–410.

Nordt, L. C., and Driese, S. G. (2013). Application of the Critical Zone Concept to the Deep-Time Sedimentary Record Lee C. *Sediment. Rec.* 11, 4–9. doi:10.2110/sedred.2013.3.

Nordt, L.C., Hallmark, C.T., Driese, S.G., and Dworkin, S.I., 2013, Multi-analytical pedosystem approach to characterizing and interpreting the fossil record of soils: New Frontiers in Paleopedology and Terrestrial Paleoclimatology, v. 104, p. 89–107.

Nordt, L.C., Hallmark, C.T., Driese, S.G., Dworkin, S.I., and Atchley, S.C., 2012, Biogeochemical characterization of a lithified paleosol: Implications for the interpretation of ancient Critical Zones: Geochimica et Cosmochimica Acta, v. 87, p. 267–282, doi: 10.1016/j.gca.2012.03.019.

Nordt, L.C., Wilding, L.P., Lynn, W.C., and Crawford, C.C., 2004, Vertisol genesis in a humid climate of the coastal plain of Texas, USA: Geoderma, v. 122, p. 83–102.

Ogg, J. G., 2012, Geomagnetic Polarity Time Scale, *in* Gradstein, F. M., Ogg, J. G., Schmitz, M. D., and Ogg, G. D., eds., The Geologic Time Scale: Oxford, UK, Elsevier, p. 85-114.

Oh, N.-H., and Richter, D.D., 2005, Elemental translocation and loss from three highly weathered soil–bedrock profiles in the southeastern United States: Geoderma, v. 126, no. 1–2, p. 5–25, doi: 10.1016/j.geoderma.2004.11.005.

O'Leary, M. H. (1988). Carbon isotopes in photosynthesis. *Bioscience* 38, 328–336.

Olszewski, T. (1999). Taking advantage of time-averaging. *Paleobiology* 25, 226–238.

Oswald, F. (1914). The Miocene Beds of the Victoria Nyanza and the geology of the country between the lake and the Kisii Highlands. *Q. J. Geol. Soc.* 70, 128–159.

Passey, B.H., Cerling, T.E., Perkins, M.E., Voorhies, M.R., Harris, J.M., and Tucker, S.T., 2002, Environmental Change in the Great Plains: An Isotopic Record from Fossil Horses: The Journal of Geology, v. 110, p. 123–140.

Patterson, B. (1965). *The fossil elephant shrews (Family Macroscelididae)*. Museum of Comparative Zoology.

Pederson, J.L., Mackley, R.D., and Eddleman, J.L., 2002, Colorado Plateau uplift and erosion evaluated using GIS: GSA TODAY, v. 12, no. 8, p. 4–10.

Peppe, D. J., Deino, A. L., Driese, S. G., Dunsworth, H. M., Fox, D. L., Harcourt-Smith, W. E. H., et al. (2017). Revised geochronology of the Early Miocene faunas from Rusinga Island and Mfangano Island (Lake Victoria, Kenya): Implications for Miocene hominoid evolution and faunal succession, American Association of Physical Anthropology annual meeting.

Perkins, M.E., Brown, F.H., Nash, W.P., McIntosh, W.C., and Williams, S.K., 1998, Sequence, age and source of silicic fallout tuffs in middle to late Miocene basins of the northern basin and range province: Geological Society of America Bulletin, v. 110, p. 344–360.

Perkins, M.E., Nash, W.P., Brown, F.H., and Fleck, R.J., 1995, Fallout tuffs of Trapper Creek, Idaho-a record of Miocene explosive volcanism in the Snake River Plain volcanic province: Geological Society of America Bulletin, v. 107, p. 1484–1506.

Peters, S.E., 2005, Geologic constraints on the macroevolutionary history of marine animals: Proceedings of the National academy of Sciences of the United States of America, v. 102, no. 35, p. 12326–12331.

Pickford, M. (1981). Preliminary Miocene mammalian biostratigraphy for western Kenya. *J. Hum. Evol.* 10, 73–97.

Pickford, M. (1986). Sedimentation and fossil preservation in the Nyanza Rift System, Kenya. *Geol. Soc. Lond. Spec. Publ.* 25, 345–362.

Pickford, M., and Mein, P. (2011). Nuevos Pedetidae (Rodentia: Mammalia) del Mio-Plioceno de Africa. *Estud. Geológicos* 67, 455–469.

Pierce, K.L., and Morgan, L.A., 1992, The track of the Yellowstone hot spot: Volcanism, faulting, and uplift: Geological Society of America Memoirs, v. 179, p. 1–54.

Poppe, L. J., Paskevich, V. F., Hathaway, J. C., and Blackwood, D. S. (2001). A laboratory manual for X-ray powder diffraction. *US Geol. Surv. Open-File Rep.* 1, 1–88.

Pound, M.J., Haywood, A.M., Salzmann, U., and Riding, J.B., 2012, Global vegetation dynamics and latitudinal temperature gradients during the Mid to Late Miocene (15.97–5.33 Ma): Earth-Science Reviews, v. 112, p. 1–22.

PRISM Climate Group, 2004, http://prism.oregonstate.edu.

Prochnow, S.J., Nordt, L.C., Atchley, S.C., and Hudec, M.R., 2006, Multi-proxy paleosol evidence for middle and late Triassic climate trends in eastern Utah: Palaeogeography, Palaeoclimatology, Palaeoecology, v. 232, no. 1, p. 53–72, doi: 10.1016/j.palaeo.2005.08.011.

Pye, K., and Tsoar, H., 1990, Aeolian sand and sand deposits: London: Unwin Hyman.

Qadir, M., and Schubert, S., 2002, Degradation processes and nutrient constraints in sodic soils: Land Degradation & Development, v. 13, no. 4, p. 275–294, doi: 10.1002/ldr.504.

Quade, J., Cerling, T.E., and Bowman, J.R., 1989, Systematic variations in the carbon and oxygen isotopic composition of pedogenic carbonate along elevation transects in the southern Great Basin, United States: Geological Society of America Bulletin, v. 101, p. 464–475.

R Core Team, 2016, R: A language and environment for statistical computing: Vienna, Austria, R Foundation for Statistical Computing, https://www.R-project.org/.

Rahbek, C., and Graves, G.R., 2001, Multiscale assessment of patterns of avian species richness: Proceedings of the National Academy of Sciences, v. 98, no. 8, p. 4534–4539.

Rascio, N., 2002, The Underwater Life of Secondarily Aquatic Plants: Some Problems and Solutions: Critical Reviews in Plant Sciences, v. 21, p. 401–427, doi: 10.1080/0735-260291044296.

Reed, L.C., and Longnecker, O.M., Jr., 1932, The Geology of Hemphill County, Texas: Bureau of Economic Geology The University of Texas Bulletin 3231, 99 p.

Retallack, G.J., 1997, Neogene Expansion of the North American Prairie: PALAIOS, v. 12, p. 380.

Retallack, G.J., 2001, Soils of the past: an introduction to paleopedology: John Wiley & Sons, 403 p.

Retallack, G. J. (2008). *Soils of the past: an introduction to paleopedology*. John Wiley & Sons.

Riebe, C.S., Hahm, W.J., and Brantley, S.L., 2017, Controls on deep critical zone architecture: a historical review and four testable hypotheses: Four Testable Hypotheses about the Deep Critical Zone: Earth Surface Processes and Landforms, v. 42, no. 1, p. 128–156, doi: 10.1002/esp.4052.

Rogers, R. R., Carrano, M. T., Rogers, K. A. C., Perez, M., and Regan, A. K. (2017). Isotaphonomy in concept and practice: an exploration of vertebrate microfossil bonebeds in the Upper Cretaceous (Campanian) Judith River Formation, north-central Montana. *Paleobiology* 43, 248–273.

Sage, R.F., 2004, The evolution of C_4 photosynthesis: New phytologist, v. 161, p. 341–370.

Salley, S.W., Sleezer, R.O., Bergstrom, R.M., Martin, P.H., and Kelly, E.F., 2016, A long-term analysis of the historical dry boundary for the Great Plains of North America: Implications of climatic variability and climatic change on temporal and spatial patterns in soil moisture: Geoderma, v. 274, p. 104–113.

Schoeneberger, P.J., Wysocki, E.C., Benham, E.C., and Soil Survey Staff, 2012, Field book for describing and sampling soils: Natural Resources Conservation Service, National Soil Survey Center, Lincoln, NE.

Seber, G., and Lee, A., 2003, Linear Regression Analysis: Wiley-Interscience, Hoboken, NJ.

Sharma, A., Weindorf, D.C., Man, T., Aldabaa, A.A.A., and Chakraborty, S., 2014, Characterizing soils via portable X-ray fluorescence spectrometer: 3. Soil reaction (pH): Geoderma, v. 232–234, p. 141–147, doi: 10.1016/j.geoderma.2014.05.005.

Schultz, G.E., 1990, Clarendonian and Hemphillian vertebrate faunas from the Ogallala Formation (late Miocene–early Pliocene) of the Texas Panhandle and adjacent Oklahoma: Geologic framework and regional hydrology: Upper Cenozoic Blackwater Draw and Ogallala Formations, Great Plains, p. 56–96.

Sharp, Z.D., and Cerling, T.E., 1998, Fossil isotope records of seasonal climate and ecology: straight from the horse's mouth: Geology, v. 26, p. 219–222.

Sheldon, N.D., Grimes, S.T., Hooker, J.J., Collinson, M.E., Bugler, M.J., Hren, M.T., Price, G.D., and Sutton, P.A., 2016, Coupling of marine and continental oxygen isotope records during the Eocene-Oligocene transition: Geological Society of America Bulletin, v. 128, no. 3–4, p. 502–510.

Sheldon, N.D., Retallack, G.J., and Tanaka, S., 2002, Geochemical Climofunctions from North American Soils and Application to Paleosols across the Eocene-Oligocene Boundary in Oregon: The Journal of Geology, v. 110, p. 687–696.

Sheldon, N.D., and Tabor, N.J., 2009, Quantitative paleoenvironmental and paleoclimatic reconstruction using paleosols: Earth-Science Reviews, v. 95, no. 1–2, p. 1–52, doi: 10.1016/j.earscirev.2009.03.004.

Shoji, S., Suzuki, Y., and Saigusa, M., 1987, Clay Mineralogical and Chemical Properties of Nonallophanic Andepts (Andisols) from Oregon, USA: Soil Science Society of America Journal, v. 51, no. 4, p. 986–990.

Slessarev, E.W., Lin, Y., Bingham, N.L., Johnson, J.E., Dai, Y., Schimel, J.P., and Chadwick, O.A., 2016, Water balance creates a threshold in soil pH at the global scale: Nature, v. 540, no. 7634, p. 567–569, doi: 10.1038/nature20139.

Smith, M., and Mosley, P. (1993). Crustal heterogeneity and basement influence on the development of the Kenya Rift, East Africa. *Tectonics* 12, 591–606.

Soil Survey Laboratory Staff, 1992, Soil survey laboratory methods manual: Soil Survey Investigations Report, v. 42.

Soil Survey Staff, 1993, Soil survey manual: Soil Conservation Service.

Soil Survey Staff, 1996, Soil Survey Laboratory Methods Manual: USDA-NRCS National Soil Survey Center Soil Survey Investigations Report No. 42, 716 p.

Soil Survey Staff, 2014, Keys to Soil Taxonomy: United States Department of Agriculture, Natural Resources Conservation Service, 12th edition, 362 p.

Stiles, C.A., Mora, C.I., Driese, S.G., and Robinson, A.C., 2003, Distinguishing climate and time in the soil record: Mass-balance trends in Vertisols from the Texas coastal prairie: Geology, v. 31, p. 331–334.

Stinchcomb, G.E., Nordt, L.C., Driese, S.G., Lukens, W.E., Williamson, F.C., and Tubbs, J.D., 2016, A data-driven spline model designed to predict paleoclimate using paleosol geochemistry: American Journal of Science, v. 316, p. 746–777.

Stone, M., 1974, Cross-Validatory Choice and Assessment of Statistical Predictions: Journal of the Royal Statistical Society. Series B (Methodological), v. 36, no. 2, p. 111–147.

Tedford, R.H., Albright, L.B., Barnosky, A.D., Ferrusquia-Villafranca, I., Hunt, R.M., Storer, J.E., Swisher, C.C., III, Voorhies, M.R., Webb, S.D., and Whistler, D.P., 2004, Mammalian biochronology of the Arikareean through Hemphillian interval (late Oligocene through early Pliocene Epochs), *in* Woodburne, M.O., ed., Late Cretaceous and Cenozoic Mammals of North America, New York, Columbia University Press, p. 169–231.

Tipple, B. J., Meyers, S. R., and Pagani, M. (2010). Carbon isotope ratio of Cenozoic CO2: A comparative evaluation of available geochemical proxies. *Paleoceanography* 25.

Thomas, G.W., 1996, Soil pH and soil acidity: Methods of soil analysis. Part 3-chemical methods., p. 475–490.

Thomas, G.W., and Hargrove, W.L., 1984, The chemistry of soil acidity, *in* Soil acidity and liming, Agronomy 12, Soil Science Society of America, Madison, WI, p. 3–56.

Torsvik, T.H., Müller, R.D., Van der Voo, R., Steinberger, B., and Gaina, C., 2008, Global plate motion frames: toward a unified model: Reviews of Geophysics, v. 46, p. 1-46.

Ufnar, D. F., Gröcke, D. R., and Beddows, P. A. (2008). Assessing pedogenic calcite stable-isotope values: Can positive linear covariant trends be used to quantify palaeo-evaporation rates? *Chem. Geol.* 256, 46–51.

Ungar, P. S., Scott, J. R., Curran, S. C., Dunsworth, H. M., Harcourt-Smith, W. E. H., Lehmann, T., et al. (2012). Early Neogene environments in East Africa: Evidence from dental microwear of tragulids. *Palaeogeogr. Palaeoclimatol. Palaeoecol.* 342, 84–96.

Uno, K. T., Polissar, P. J., Jackson, K. E., and others (2016). Neogene biomarker record of vegetation change in eastern Africa. *Proc. Natl. Acad. Sci.* 113, 6355–6363.

Van Breemen, N., 1982, Genesis, Morphology, and Classification of Acid Sulfate Soils in Coastal Plains: Acid Sulfate Weathering, v. sssaspecialpubl, no. acidsulfateweat, p. 95–108, doi: 10.2136/sssaspecpub10.c6.

Vepraskas, M. J. (2001). Morphological features of seasonally reduced soils. *Wetl. Soils Genes. Hydrol. Landsc. Classif.*, 163–82.

Walker, A., Teaford, M. F., Martin, L., and Andrews, P. (1993). A new species of Proconsul from the early Miocene of Rusinga/Mfangano Islands, Kenya. *J. Hum. Evol.* 25, 43–56.

Wang, Y., Cerling, T.E., and MacFadden, B.J., 1994, Fossil horses and carbon isotopes: new evidence for Cenozoic dietary, habitat, and ecosystem changes in North America: Palaeogeography, Palaeoclimatology, Palaeoecology, v. 107, p. 269–279.

Webb, S.D., 1965, The osteology of Camelops: Bulletin of the Los Angeles County Museum, v. 1, p. 1–54.

Whitworth, T. (1954). *The miocene hyracoids of East Africa: with some observations on the order hyracoidea*. British Museum.

Wilson, M.J., 1999, The origin and formation of clay minerals in soils: past, present and future perspectives: Clay Minerals, v. 34, p. 7–25.

Wood, H.E., Chaney, R.W., Clark, J., Colbert, E.H., Jepsen, G.L., Reeside, J.B., Stock, C., and others, 1941, Nomenclature and correlation of the North American continental Tertiary: Geological Society of America Bulletin, v. 52, p. 1–48.

Wynn, J.G., 2007, Carbon isotope fractionation during decomposition of organic matter in soils and paleosols: implications for paleoecological interpretations of paleosols: Palaeogeography, Palaeoclimatology, Palaeoecology, v. 251, p. 437–448.

Zachos, J., Pagani, M., Sloan, L., Thomas, E., and Billups, K., 2001, Trends, rhythms, and aberrations in global climate 65 Ma to present: Science, v. 292, p. 686–693.

Zamanian, K., Pustovoytov, K., and Kuzyakov, Y., 2016, Pedogenic carbonates: Forms and formation processes: Earth-Science Reviews, v. 157, p. 1–17.